UPC CTTC

Novel Dispersion Error and Grey Area Mitigation Approaches for Subsonic Jet Noise Spectra

Heat and Mass Transfer Technological Centre Departament de Màquines i Motors Tèrmics Universitat Politècnica de Catalunya

> Jesús Ruano Doctoral Thesis

Novel Dispersion Error and Grey Area Mitigation Approaches for Subsonic Jet Noise Spectra

Jesús Ruano

PHD THESIS

submitted to the

Departament de Màquines i Motors Tèrmics Escola Superior d'Enginyeries Industrial, Aeroespacial i Audiovisual de Terrassa Universitat Politècnica de Catalunya

in partial fulfillment of the requirements for the degree of

Doctor of Philosophy in Thermal Engineering

Terrassa (Barcelona), September 2025

Novel Dispersion Error and Grey Area Mitigation Approaches for Subsonic Jet Noise Spectra

Jesús Ruano

Thesis Supervisors

Prof. Francesc Xavier Trias Miquel Prof. Assensi Oliva Llena

Committee Board

Dr. Tatiana Kozubskaya Keldysh Institute of Applied Mathematics

> Dr. Gennaro Coppola Università di Napoli 'Federico II'

Dr. Jesús Castro Universitat Politècnica de Catalunya

Aquesta tesi està dedicada als meus pares, Jose i Maria del Carme, a les meves dues germanes, Judith i Noelia, i a qui fa que els dies valguin una mica més la pena, Cèlia

Acknowledgements

I want to express my most sincere gratitude to all the people who have contributed to this thesis both explicitly and implicitly. It has been a long journey, but it seems that, finally, has come to an end.

I think that, like most of the people in the lab, I would not be here if Prof. Assensi Oliva had not given me the chance. A part-time contract during the summer of 2013 to perform my Final Masters Thesis became the seed to fully introduce me into the world of CFD.

If there is a name in this thesis that should be specially thanked, this would be undoubtedly Prof. Xavi Trias. Always humble and never imposing your ideas over others, you always have time to discuss about everything and push forward all those around you. If I'm here, literally, is because of you.

I would also especially thank Aleix Baez. When I could only repeat that we needed to move forward high-order methods if we wanted to study acoustics, Aleix just asked for a reason that did not involve an argument based on conclusions extracted in meshes we will never be used... So we started working on dispersion error.

Alexey Duben and Andrey Gorobets have been an amazing duo to work with. The second part of this thesis would not have been possible without them, as their work has allowed for the final showdown between low and high-order schemes when applied to the transonic round jet.

Arnau, as you wrote some years ago: a tu et guardo un lloc apart. We started in this together and learned what CFD was together. At good times and bad times, you have been there! Ets un grande que arribarà on vulgui!

Another special guest that should appear here, and in all the thesis done in the lab, is Octavi. It doesn't matter which problem you have with your computer... because in the time moving from Octavi's desk to your own, he has already fixed it. Un altre grande!

Of course, I would also like to thank all the people from the CTTC with whom I shared part of this journey! There is a long list... but you know that, if we have interacted, you are inside it!

I would also thank all the people from the Keldysh Institue of Applied Mathematics in Moscow who welcomed me in February 2017... because if you go to Russia, at least go when it's cold. It was amazing and, even though was short, the fundamentals in aeroacoustics I learned there form the basis for the second half of this thesis.

Finally, I would like to especially thank all the support from my family. Both my parents and sisters have been a haven on which I could rely to recover when I needed to.

And Cèlia, without your support and your patience... I don't really know how this thesis would have been written... This thesis is for you.

Abstract

With increased noise restrictions applied to aviation, the Computational AeroAcoustics community is growing day by day.

In Computational AeroAcoustics, scientists deal with a numerical error not always considered in other disciplines: the dispersion error. This error generates that waves with different frequencies travel at different speeds, distorting the acoustic spectrum.

At the same time, they need to deal with problems related to turbulence modeling but requiring time-dependent solutions, thus avoiding RANS methods. At the same time, they need to solve problems involving high-speed regimes flows and/or geometries with increased complexity, therefore making it difficult to apply an LES model fulfilling its mesh requirements.

Dispersion error has classically been studied by means of projecting the derivative onto the Fourier space and then analyzing the difference between the numerical and analytical wavenumber.

However, such a method is only possible to be applied to evenly spaced domains with periodic boundary conditions and linear discretization schemes.

Here, we present a new methodology to numerically analyze and evaluate this error, without the main constraint of being limited to structured uniform meshes but also applicable to stretched ones. At the same time, the new method is able to handle non-linear schemes, such as blendings between upwinded and central schemes, usually used within the CAA community.

The extracted conclusions with this new method, when applied to stretched grids, do not show a clear difference between high and low-order numerical schemes, as the former quickly degrades its order of accuracy.

Detached-Eddy Simulation (DES) has gathered a lot of attention these last years as an interesting approach for covering the gap between RANS and LES turbulence models in terms of both computational resources and degree of modeling. DES is able to produce reliable unsteady results without having excessively stringent mesh requirements. To check the validity of the conclusions extracted in the first part of this work, together with the feasibility of DES, we simulate a subsonic round jet.

vi Abstract

We will be using two different numerical codes: NOISEtte, which uses high-accuracy schemes, and OpenFOAM, an open-source code that uses low-order schemes. This allows us to compare the effect that the order of the scheme has on the acoustic spectra of the subsonic round jet.

At the same time, we will analyze how the filtering length scale and the subgrid turbulence model are able to attenuate one of the main issues within DES: the unphysical slow transition from RANS to LES, known as the Gray Area problem. If the turbulence model is not able to minimize the effects of this transition, would result in unphysical noise generated that could not be distinguished from the correct one.

The conclusions extracted from this analysis show a similar performance between high and low-order schemes, at least if only aerodynamics are considered. The acoustic spectrum obtained by using low-accuracy methods differs slightly more than the one obtained by using high-accuracy methods. Nonetheless, these differences are bound to be inferior to 3 dB and at the most challenging observer angles.

Contents

A	bstrac	t		\mathbf{v}
1	Intr	oduction		1
	1.1	Noise: why?		. 1
			ts on the human body	
			dynamic noise	
	1.2	How turbule	ent noise is studied?	. 5
			outational AeroAcoustics: definition	
			t methods	
			id approaches	
	1.3	-	n CAA	
			ersion and diffusion	
		_	ılence modelling	
	1.4		the thesis	
	1.5		e thesis	
2		_	dispersion errors on Cartesian stretched meshes f	
	both		on-linear operators	31
	2.1			
	2.2	Theoretical b	packground	36
	2.3	Methodology	y	41
		2.3.1 Evalu	aating the gradient	43
		2.3.2 Select	tion of an orthonormal basis	43
		2.3.3 Effect	t of the phase	46
		2.3.4 Study	ring sinusoids or other functions	47
	2.4	Numerical te	ests	48
		2.4.1 Dispe	ersion error results: Eigenbase	53
		_	ersion error results: Sinusoids	
	2.5	*	time step	
			ected performance	
	2.6			

viii Contents

_				
3			of numerical scheme and turbulence model on subsoni	
	rou	nd jet s	pectra	79
	3.1	Introd	luction	80
	3.2	Case I	Formulation and Computational Meshes	83
	3.3		ematical Models and Numerical Methods	85
	3.4		ts and Discussion	88
		3.4.1	Influence of GAM Approaches on Jet Plume Aerody-	
			namics	88
		3.4.2		
		0.1.2	dynamics for a Set of Refining Meshes	91
		3.4.3	Influence of the Selected GAM Approaches on Jet Aeroa-	71
		0.1.0	coustics for a Set of Refining Meshes	95
		3.4.4	e e e e e e e e e e e e e e e e e e e	100
	٥.	0.1.1	Evaluation of Far-Field Results on <i>Grid 3</i>	
	3.5		usions	101
		Refere	ences	103
4	Com	ما ده ا	ns and further work	109
4				
	4.1	Concl	uding remarks	109
		4.1.1	Concluding remarks on the development of a new dis-	
			persion error methodology	109
		4.1.2	Concluding remarks on jet aerodynamics and aeroacous-	
			tics	110
	4.2	Furth	er work	112
		Refere	oncos	113

List of Figures

1.1	Most relevant noise sources on-board of conventional midrange transport aircraft. Credits to Henri Siller and Jan Delfs, DLR, 2019	4
1.2	Anechoic chamber in UCI Aeroacoustics Lab. Credits to Dimitri	_
	Papamoschou, UCI, 2022	6
1.3	Obtained profiles of the initial Gaussian impulse at times t=0 and t=500. From top to bottom: first-order upwind scheme,	
	second-order central scheme, sixth-order central scheme, and	
	DRP4 scheme	15
1.4	Turbulent kinetic energy wavenumber spectrum. Extracted	
	from [20]	17
2.1	Examples of discrete eigenvectors in two-dimensional meshes.	
	Left: low eigenvalue associated, right: high eigenvalue asso-	
	ciated. Top: uniform mesh; Middle: stretched mesh; Bottom:	
	unstructured mesh	45
2.2	Used meshes with increasing strteching factor from top (0%) to	
	bottom (5%) and equal minimum mesh size	49
2.3	Normalized polar plot of wave number anisotropy for wavenum-	
	bers $\frac{k\Delta}{\pi} = \frac{1}{10}, \frac{2}{10}, \dots \frac{9}{10}, \frac{10}{10}$. Left: second-order central difference	
	scheme; Right: fourth-order DRP scheme	51
2.4	Recovered numerical vs analytical eigenvalue made non-dimension	nal
	using the maximum mesh size	53
2.5	Difference between diagonal terms and the root mean square of	
	the row of matrix Γ after 5000 rotations made non-dimensional	
	using the maximum mesh size	54
2.6	Standard deviation of the recovered numerical eigenvalue made	
	non-dimensional using the maximum mesh size	55
2.7	Recovered numerical vs analytical eigenvalue made non-dimension	nal
	using the minimum mesh size	56
2.8	Recovered numerical vs analytical wavenumber made non-	
	dimensional using maximum mesh size	57
2.9	Recovered numerical vs analytical wavenumber made non-	
	dimensional using minimum mesh size	58

2.10	Standard deviation of recovered numerical wavenumber vs an- alytical wavenumber made non-dimensional using maximum	
	mesh size.	59
2.11	Computational cost vs relative error at wavenumber range 0 to	
	32π for different stretchings and linear convective schemes	66
2.12	<u> </u>	
	32π for different stretchings and non-linear convective schemes.	67
3.1	Distributions of maximum (Δ_{max}/D , solid lines) and minimum	
	(Δ_{\min}/D) , dashed lines) mesh sizes along the lip line for the	
	meshes considered	85
3.2	The instantaneous flow field in the jet plume region (the NOISEtte	
	simulation on the <i>Grid 3</i> mesh using the Δ_{SLA} +SMG approach).	
	The yellow lines mark the location of the FWH control surfaces	87
3.3	Instantaneous flow fields (vorticity magnitude, $ \Omega $) on the	
	Grid 2 mesh in the mid-span section: strongly delayed RANS-	
	to-LES transition in the shear layer using the SGS $\tilde{\Delta}_{\omega}$ (left),	
	delayed transition using Δ_{ω} (center) and rapid transition using	
	Δ_{SLA}	88
3.4	Centerline distributions of streamwise velocity (left) and its rms	
	(right) obtained using all the considered combinations	89
3.5	Lipline distributions of the rms of streamwise velocity obtained	
	using all the considered combinations	90
3.6	Lipline distributions v_t/v obtained using all the considered	
	combinations	91
3.7	Centerline distributions of the streamwise velocity obtained	
	using NOISEtte (left) and OpenFOAM (right) on a set of refining	
	meshes (top to bottom)	92
3.8	Centerline distributions the streamwise velocity pulsations rms	
	obtained using NOISEtte (left) and OpenFOAM (right) on a set	
	of refining meshes (top to bottom)	93
3.9	Lipline distributions of the streamwise velocity pulsations rms	
	obtained using NOISEtte (left) and OpenFOAM (right) on a set	
	of refining meshes (top to bottom)	94
3.10	Noise directivity obtained using NOISEtte (left) and Open-	0.
	FOAM (right) on a set of refining meshes (top to bottom)	96

LIST OF FIGURES xi

3.11	1/3rd-octave integrated spectrums at the observer angle $\theta =$	
	60° using NOISEtte (left) and OpenFOAM (right) on a set of	
	refining meshes (top to bottom)	97
3.12	1/3rd-octave integrated spectrums at the observer angle $\theta =$	
	150° using NOISEtte (left) and OpenFOAM (right) on a set of	
	refining meshes (top to bottom)	99
3.13	Deviation of OASPL from the experimental data in dB Δ_{dB} =	
	$OASPL_{comp} - OASPL_{exp}$ (top) and lipline distributions of v_t/v	
	(bottom) obtained on <i>Grid 3.</i>	100

List of Tables

2.1	List of the different used meshes and the symbol of the results	
	obtained when using them and the acronyms of the convective	
	schemes	52
2.2	Non-dimensional maximum eigenvalue normalized respect	
	maximum eigenvalue for second-order symmetry preserving	
	in uniform meshes, linear schemes	62
2.3	Non-dimensional maximum eigenvalue normalised respect	
	maximum eigenvalue for first-order upwind in uniform meshes,	
	non-linear schemes	63
2.4	Arithmetic Intensity for each differential scheme	64
2.5	Number of bytes (B) in double-precision for each differential	
	scheme	64
3.1	Meshes parameters	84
3.2	Computational cost of $100D/U_{iet}$ time units on <i>Grid</i> 3	88

Introduction

Abstract. In this introductory chapter, we explain why scientists became more interested in problems involving both the production and transport of sound, commonly noise. Then, the different approaches that investigators could use to study sound propagation will be described. During this description, the problems that emerge during these studies will naturally come up, so they will be detailed, as well as how the mitigation or, on the other hand, their presence affects the quality and validity of the obtained results. Finally, the main conclusions of this first chapter will be presented justifying the need for the present thesis and similar studies to understand better the different roles of several elements involved in noise simulation problems, and how these elements ultimately affect the obtained results.

1.1 Noise: why?

Humanity wants to be comfortable. This is not only because a comfortable situation is more desirable than an uncomfortable one but also because discomfort could eventually generate a health problem. This problem may not appear immediately, but its effects surging due to a very long exposition or appearing all of a sudden due to a very intense exposition. For this reason, every situation which involves some degree of discomfort should be studied to analyze how this discomfort has arisen and, if possible, how it can be mitigated or avoided.

Inside the most common sources of peoples' discomfort, we find noise. From a physical point of view, there is no difference between sound and noise as both are mechanical vibrations traveling through a continuum medium;

it is psychology that makes the difference between wanted and unwanted sound, i.e., noise. Therefore, noise is defined as an unwanted sound that is unpleasant and usually louder than its wanted counterpart.

1.1.1 Effects on the human body

As has been previously said, noise "loudness" is usually the primary source of discomfort and the one that can affect the health of the people exposed.

140 dB is defined as the pain threshold at which the sound becomes painful to hear. An example of such noise level is the jet engine at take-off for a close observer located at approximately 30 m. If the observer were just 1 meter from the engine, the level would rise to 150 dB instead. It is not necessary to achieve such noise levels to induce instantaneous hearing loss, as noise levels around 120 dB can provoke it. Examples of these levels are diverse and can be found in a pop/rock concert or produced by a two-stroke chainsaw. However, long exposures to smaller levels can still induce hearing loss.

For a typical workday, i.e., 8-hour average, the recommended exposure levels should be below 85 dB(A) [1]. If this exposure was continuous throughout the whole period, the noise levels should be lowered to 70 dB(A) instead.

Finally, hearing loss is not the only consequence on hearing that noise can cause. Noise can also cause tinnitus, a noise perceived as ringing, buzzing, or roaring when external noise production is not present. This may be caused by a single and strong exposure or by a continuous and more attenuated one.

Hearing risks are not the only concern regarding noise, as it has effects on other aspects of health and daily life. Noise is one of the main causes of stress. Non-hazardous noise levels can still be problematic if they cause the listener to be tense. For example, a non-understandable and continuous mumble during work hours. This noise is, of course, non-damaging as it is extremely low but can cause concentration problems and even the impossibility of executing a task correctly. Linked with this, there is a correlation between noise pollution and cardiovascular disease, as environmental noise can increase the risk of high blood pressure levels and the incidence of arterial hypertension, heart failure, and stroke due to increased stress levels [2].

Recent investigations are linking the apparition of dementia and Alzheimer's disease with hearing loss [3]. Sleep quality is highly affected by the presence of noise. It does not require an excessively high sound, but just enough to

become a nuisance. Furthermore, noise does not require waking you up or making it impossible to sleep in order to have detrimental effects. The brain still processes and registers sound while sleeping, leading to a worsening in sleep quality.

1.1.2 Aerodynamic noise

Noise is generated by very different mechanisms. Taking, for example, a car, it can be distinguished between the noise generated by the friction between the wheels and the road or the noise generated by the air flowing through the air conditioning systems [4]. Among all the noise generation mechanisms, aerodynamic noise is the one we want to put focus on during this thesis. Aerodynamic noise refers to the sound generated by an unsteady flow, generally turbulent. This generation is produced via two different mechanisms:

- The interaction of aerodynamic forces with solid surfaces. Examples
 of this kind of noise generation include propellers, rotorcraft, landing
 gears, airplane fuselage...
- The fluid turbulent motion itself. Examples of this kind of noise generation mechanism are free shear layer problems, such as immersed jets, or sudden expansions like backward-facing step configurations.

Intuitively, it is easy to understand that the aerodynamic noise is generated by a fluid in motion. The higher the motion, i.e., velocity, the higher the noise. Therefore, this kind of noise is usually associated with high-speed flows.

Previously, it has been shown as an example of two different noise mechanisms in a car. More precisely, of an exterior noise generation mechanism -tire noise- and an interior one -air conditioning system noise. Regarding exterior sound mechanisms, tire noise is the predominant noise generation mechanism at low speeds, i.e., cities. However, aerodynamic noise becomes the predominant sound mechanism on highways where the car achieves velocities around 100-120 km/h.

Cars are not the only transport where aerodynamic noise has become a problem; trains also face a very similar situation. While the friction between the rail and the wheels of the train is the predominant noise generator at low speeds, the pantograph becomes the predominant noise generator at higher

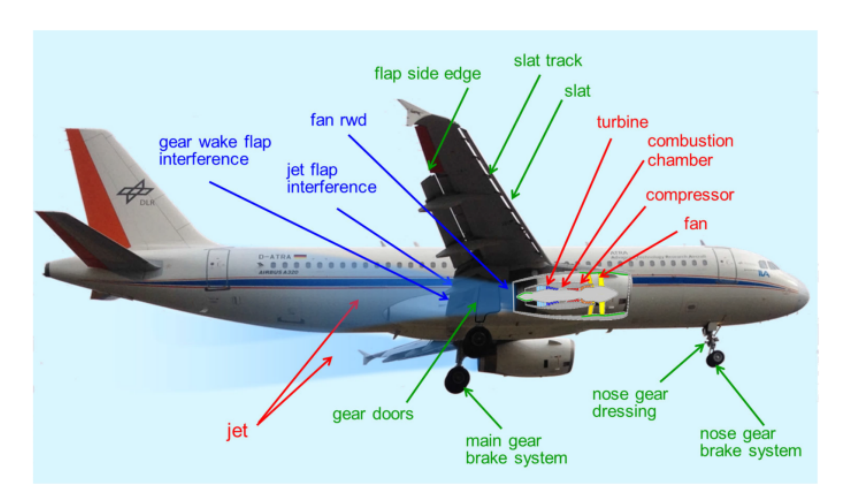


Figure 1.1: Most relevant noise sources on-board of conventional mid-range transport aircraft. Credits to Henri Siller and Jan Delfs, DLR, 2019

velocities [5,6]. Additionally, at very high-speed regimes achieved by bullet trains, the whole wagon becomes a noise generator [5,7].

Still with transport systems, commercial aviation has been dealing with noise comfort since its apparition at the end of WW2. Unlike than during the years prior, when airplane noise was not seen as a problem and more as an intimidating strategy, commercial aviation wants quite the opposite: the quietest the airplane, the better. In high altitudes, predominant noise generators are located on the whole fuselage and the engine, which can be annoying for passengers and crew members. People living near airports also suffer from noise emitted by airplanes, especially during taking-off and landing, when noise is mainly generated by the jet flow exiting the engine. In Figure 1.1, the most relevant noise sources in the typical configuration of a mid-range airplane are included.

Finally, also within transport systems but not related to vehicles in motion, climatization systems are known to be a noise source. Even though the sound power levels of these systems are usually low, their constant presence can be annoying.

1.2 How turbulent noise is studied?

As has been previously said, noise is an issue which can evolve into an eventual health problem. Therefore, it should be studied to establish how it is produced. At the same time, understanding the noise production mechanisms will lead to improved designs that reduce or minimize the radiated sound.

The first and most straightforward option to study noise is to measure it directly. In other words, use an experiment facility at which the noise production conditions are replicated in order to obtain a direct measure of the noise. However, such an option is not always the best approach for various reasons.

First, it requires the physical noise generator object which needs to be analyzed. In the prototyping stage, this approach is not cheap as if several geometries or designs are being considered, all these designs should be manufactured, with their corresponding manufacturing cost, and then studied.

Second, the facilities used to obtain noise measures have strict requirements to not influence the results [8]. Sound has a vast influence domain, i.e., noise decays slowly compared to turbulence, and, additionally, it bounces in the walls. This means that a returning sound wave could interact with an outgoing wave, distorting the results. Therefore, facilities with walls that are very far from the observation point of interest or alternatively, or even better, in conjunction with absorbing noise walls should be used. In other words, massive facilities or anechoic chambers, like the one in Figure 1.2, should be used.

The second option relies on simulation. Instead of reproducing the problem in the real world, the numerical simulation reproduces and studies it in a computer. This avoids the costs of manufacturing several options under study as their geometry, usually a CAD file or equivalent, is the required input. Moreover, there is no need to use huge facilities or anechoic chambers to avoid undesired wall effects such as sound wave bouncing. This problem is easily solved by imposing a specific boundary condition to avoid a reflection back to the domain. This approach is what is called Computational AeroAcoustics.

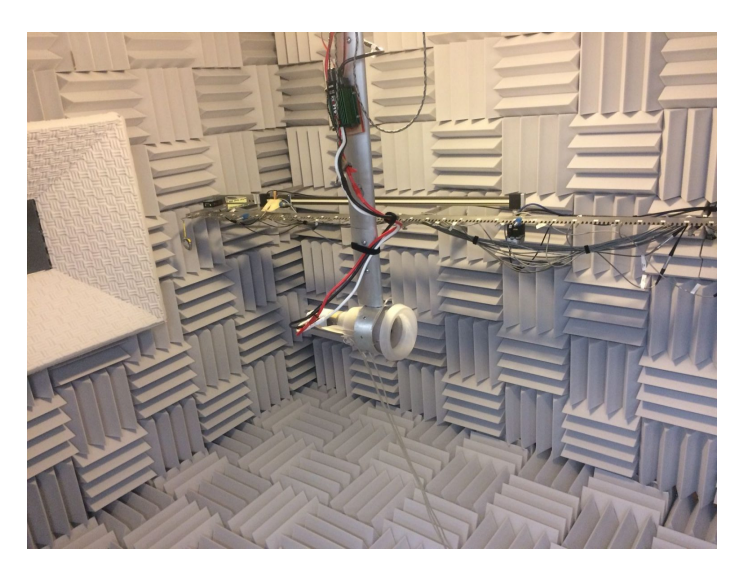


Figure 1.2: Anechoic chamber in UCI Aeroacoustics Lab. Credits to Dimitri Papamoschou, UCI, 2022

1.2.1 Computational AeroAcoustics: definition

Computational AeroAcoustics (CAA) is a subbranch of both acoustics and turbulence whose objective is to analyze the noise generated by a turbulent fluid via numerical methods. As the available computational resources have increased in recent years, this has allowed a simulation-based approach for aeroacoustics possible. As the possibility of studying real-life problems where noise plays a relevant role is becoming a reality, Computational Fluid Dynamics (CFD) researchers have put their focus on studying turbulent-induced noise.

As CAA is relatively a new-born area, there is still not a clear winner between all the different approaches that exist; each procedure has its cons and pros, making it more suited for a case but producing awful results in others. The first big division between CAA methods comes from how noise is computed.

1.2.2 Direct methods

The first and probably the most straightforward methodology to understand are the direct methods. These methods take the fully compressible set of Navier-Stokes (NS) equations and solve it *directly*, as noise generation and propagation are included implicitly in the set of equations [9].

So, by just simulating NS equations, it is possible to study noise-related problems without any modelization or approximation of how noise is produced and transported. Turbulence models, luckily, can be used in this kind of approach and are still considered direct methods. These kinds of simulations require domains as large as the distance between where the noise is produced and where the noise is wanted to be analyzed, i.e., an observer or several observer positions. Compared with CFD, direct methods can be seen as a kind of Direct Numerical Simulations (DNS) applied to acoustics, and as happens with DNS, not everything is positive.

The first issue is that direct methods require a considerable amount of computational resources, mainly due to two reasons: domain size and multiscale. As has been previously commented, direct methods require very large domains, which translates into discrete domains larger than those treated by CFD. Aeroacoustics is, additionally, a multiscale problem. This means that the scales of acoustics and hydrodynamics vary by several orders of magnitude. In other words, in the region where noise is produced, hydrodynamic forces are thousands of times stronger than acoustic waves, which can be easily hidden by the numerical errors of the former.

The second problem is that even though both CFD and CAA seem to have a lot in common, some of the best methodologies that work on CFD are not precise enough to work on CAA. For example, the second-order scheme is one of the most used schemes in CFD for the advective term. However, when dealing with acoustics, low-order schemes are usually insufficient to consistently simulate acoustic waves as these are dampened or distorted due to high amounts of diffusion and dispersion [10]. Nonetheless, there is a solution to circumvent this problem and still use the same schemes as the CFD community: reduce the mesh sizes so both numerical errors, which depend on the local mesh resolution, become negligible. However, it is easy to see how this solution will affect the first issue commented: mesh will increase its size dramatically.

1.2.3 Hybrid approaches

The other option consists of the so-called hybrid approaches. This kind of approach decouples the problem into noise generation and noise propagation. The CFD solver handles the first part as noise is generated due to the interaction between aerodynamic forces and turbulence. Noise propagation to the far-field, i.e., the region in space where only acoustics plays a relevant role as turbulence is negligible and the fluid has practically non-movement, is handled by the acoustic solver or post-processor. In summary, hybrid approaches decouple noise problems into two different problems: how noise is generated and how noise is transported.

Regarding how noise sources are computed, we can distinguish between two different methodologies to obtain acoustic sources:

- Resolved sources, which are constructed using hydrodynamic variables extracted directly from the fluid, mainly density, velocity, and pressure. This requires as input the transient information from the CFD solver, restricting the CFD simulation to a DNS, an LES, or a DES.
- Reconstructed sources, which are modeled semi-empirically after some turbulent information extracted from the CFD simulation. The accuracy and reliability of these kinds of methods depend on how those semiempirical sources had been constructed. Moreover, unlike with resolved ones, reconstructed sources do not require a transient input, making it possible to use RANS in the CFD simulation [11].

Again, there is no unique methodology for noise transport, but two different approaches can be distinguished:

Analytical transport methods, in which the wave equation is used in an integrated form, such as Lighthill's equation [12], Kirchhoff's surface integral, or Ffowcs-Williams Hawkings equation [13]. These methods compute acoustic sources along a region of the space, being it a volume or a surface, and then, through the sound speed, the noise generated by these sources is extrapolated to the observer location points. Finally, the full acoustic signal is obtained by summing the noise obtained from all the sources.

 Numerical transport methods, in which the partial differential equation under study is discretized and solved numerically. In this sense, these methods are very similar to a conventional CFD simulation, as both take the same approach: discretize and solve numerically a PDE or a system of PDEs. They differ from the acoustic direct approach in the sense that these methods do not simulate the same set of equations. For example, among the more common approaches, there are the Euler Equations or their linearized form (LEE), which are used to avoid instability issues arising from the lack of diffusivity. Alternatively, more accurate approaches, such as Linearized Acoustic Perturbation Equations (LPCE) [14] or Acoustic Perturbed Equations (APE) [15] systems, with different application areas for each one. Finally, as the system of equations to solve is different from the NS equations solved by the CFD solver, specifically tuned schemes with low dispersion and diffusion properties can be used. This allows using the best approach for each problem. Nonetheless, they share a common problem with direct methods as domains require to be larger enough to cover the distance between the generation region and the observation point under interest.

1.3 Open areas in CAA

Computational AeroAcoustics has not yet achieved a level of maturity that can be considered a fully closed discipline. As numerically simulating the fluid is required in order to study its noise spectra in CAA. Basically, all the open areas in CFD affect, to one degree or another, the quality and validity of the CAA results. Furthermore, to add more complication, CAA deals with a multiscale problem. This means that the amplitudes of hydrodynamic oscillations and acoustic waves have different orders of magnitude. In other words, it is easy for the acoustic wave to be entirelly swallowed by the hydrodynamic oscillation errors.

Acoustic waves are characterized by their amplitude, frequency, and the speed at which they travel. If several of these acoustic waves interact between them, they produce a resulting noise. As waves can be both destructive and constructive depending on the phase they have between them, it is possible for two waves to produce a more energetic wave or result in a null wave, i.e.,

a wave with zero amplitude. So, it is of paramount importance to achieve good numerical resolution of both amplitude and speed of acoustic waves as, otherwise, the interaction between them will not be correct. In other words:

- If the amplitude of one considered wave is smaller than it should be, the result of interacting with another wave, with or without the correct amplitude, will not be correct. More precisely, the amplitude of the resulting wave will not be correct.
- But if the velocity of the acoustic wave is not well computed, this has more implications. If two waves with incorrect phases between them, due to a mismatch between propagation velocities, interact, both the phase and the amplitude of the resulting wave will not be correct.

Independently of the procedure used to compute aerodynamic noise, except in the case of spectral methods, they all share the fact that a numerical approximation of the derivative is required. Therefore, numerical schemes have to be used. These schemes affect the accuracy of both the amplitude and the velocity of the resulting acoustic waves. And, as a rule of thumb, the higher the accuracy or order of the used scheme, the lower the error committed in both amplitude and velocity of propagation.

1.3.1 Dispersion and diffusion

Numerical approximation of the derivatives induces two kinds of errors, or three if a non-linear field, such as the product of two fields, is derived. These errors are:

- Diffusion error.
- Dispersion error.
- Aliasing error.

We want to put our focus on the two first, as even though Navier-Stokes equations present the derivative of a non-linear field, the usual approach in acoustics is analyzing diffusion and dispersion only. This happens due to, usually, acoustic problems being linear.

Diffusion error

The numerical diffusion error is the phenomenon observed in numerical simulations where the simulated medium exhibits a higher diffusivity than its real counterpart.

Its appearance can be both positive and negative. For example, if a high-fidelity simulation is performed, numerical diffusion can cause the obtained results to not be enough as they do not resemble what occurs in reality. However, on the other hand, numerical simulations also deal with stability. Adding some artificial viscosity can lead to converging simulations, whereas the lack of it could be the reason behind a diverging simulation. For example, if shock waves are considered, the numerical simulation has to be able to compute an extremely thin wave, i.e., a field gradient extremely high. Therefore, in order to stabilize the simulation, it is recommended to add some diffusion, as otherwise, it would blow up.

It is relatively easy to see how diffusion error is introduced. The derivative operator is known to be skew-symmetric. In other words, it makes the next relation true:

$$\langle \phi, C\psi \rangle = -\langle C\phi, \psi \rangle,$$
 (1.1)

where *C* is the derivative operator. Therefore, in order to mimic the previous property, skew-symmetric schemes should be used [16,17]. In the case that the numerical scheme has a symmetric component, such as the family of upwind schemes, among others, this will introduce some numerical diffusion to the simulation.

Dispersion error

The definition of numerical dispersion error is quite similar to numerical diffusion. The numerical dispersion error is the phenomenon observed in numerical simulations where the simulated medium exhibits a higher dispersivity than its real counterpart. However, its effects are not so clear.

Taking, for example, a linear first-order wave propagation equation in 1D:

$$\frac{\partial \phi}{\partial t} + c \frac{\partial \phi}{\partial x} = 0, \tag{1.2}$$

where *c* is a constant wave velocity propagation. The previous equation follows a linear dispersion relation between the angular frequency and the

wavenumber equal to:

$$\omega = ck. \tag{1.3}$$

The previous means that both phase velocity c_p and group velocity c_g are the same as

$$c_p = \omega/k = c, \tag{1.4}$$

and

$$c_g(k) = \frac{\partial \omega}{\partial k} = c. \tag{1.5}$$

However, the previous does not hold when a discrete differential scheme is used. In this case, the relation between the angular frequency and the wavenumber is equal to:

$$\omega = c\hat{k}(k),\tag{1.6}$$

where $\hat{k}(k)$ is the numerical wavenumber as a function of the analytical one. This means that the group velocity now is:

$$c_g(k) = \frac{\partial \omega}{\partial k} = \frac{\partial \omega}{\partial \hat{k}(k)} \cdot \frac{\partial \hat{k}(k)}{\partial k} = c \cdot \frac{\partial \hat{k}(k)}{\partial k}.$$
 (1.7)

What does the previous equation mean? Equation 1.5 shows that all the different wave components have the same speed. However, Equation 1.7 shows that, unless the numerical wavenumber is equal to the analytical one, the different components each have a different propagation speed, even though they must have the same one.

Spectral approach of diffusion and dispersion

The previous introductions to diffusion and dispersion error can be seen as a "physical" approach to understanding them. However, it is possible to take an entirely mathematical approach and still be able to explain how these errors appear [10,18].

First, let us assume a numerical discretization of the first derivative in a structured and uniform distribution of nodes:

$$\frac{\partial \phi}{\partial x} \simeq \frac{1}{\Delta x} \sum_{j=-N}^{N} a_j \phi(x + j \Delta x).$$
 (1.8)

Then, the Fourier Transform of each side of the equation is performed. Being the left-hand side equal to:

$$FT\left(\frac{\partial\phi}{\partial x}\right) = ik\hat{\phi}(k),\tag{1.9}$$

and the right-hand side is equal to:

$$FT\left(\frac{1}{\Delta x}\sum_{j=-N}^{N}a_{j}\phi_{j}\right) = \frac{1}{\Delta x}\left[\sum_{j=-N}^{N}a_{j}e^{ijk\Delta x}\right]\hat{\phi}(k). \tag{1.10}$$

Then, equating both terms again:

$$ik\hat{\phi}(k) \simeq \frac{1}{\Delta x} \left[\sum_{j=-N}^{N} a_j e^{ijk\Delta x} \right] \hat{\phi}(k).$$
 (1.11)

The right-hand side can be rewritten in a form such as becomes more similar to the left-hand side. For example:

$$\frac{1}{\Delta x} \left[\sum_{j=-N}^{N} a_j e^{ijk\Delta x} \right] \hat{\phi}(k) = i\bar{k}\hat{\phi}(k). \tag{1.12}$$

Therefore, there is a relation between the analytical wavenumber k and the numerical one \bar{k} :

$$\bar{k} = \frac{-i}{\Delta x} \left[\sum_{j=-N}^{N} a_j e^{ijk\Delta x} \right]. \tag{1.13}$$

As can be seen in Equation 1.13, the numerical wavenumber \bar{k} is a complex number. However, the analytical wavenumber is a real number. Or the same: a complex number with a null imaginary part. The only possibility for the numerical wavenumber to have a non-zero imaginary part is that the weights of the selected numerical scheme, i.e the a_j terms in the previous equations, are not purely skew-symmetric. In other words, using skew-symmetric schemes avoids having a numerical wavenumber with a complex component. However, using skew-symmetric schemes when approximating the derivative was also the reason to avoid introducing numerical diffusion. Therefore, if the numerical wavenumber has an imaginary component, this indicates the presence of numerical diffusion error.

Finally, it is also easy to link the numerical wavenumber with the dispersion error. Assuming a skew-symmetric scheme has been used, in order to simplify the discussion, the numerical wavenumber expression 1.13 can be further reduced to:

$$\bar{k} = \frac{2}{\Delta x} \left[\sum_{j=1}^{N} a_j \sin(jk\Delta x) \right]. \tag{1.14}$$

For example, for the well-known second-order symmetry-preserving scheme where $a_1 = -a_{-1} = \frac{1}{2}$, the Equation 1.14 reduces to:

$$\bar{k} = \frac{\sin(k\Delta x)}{\Delta x}.\tag{1.15}$$

So, what is dispersion error? It is a mismatch between the numerical wavenumber and the exact wavenumber. And, unlike the diffusion error, numerical dispersion error cannot be avoided by any means except when spectral methods are used. This is explained by Equation 1.14, as the relation between the numerical and the analytical wavenumber will always be expressed by means of a non-linear relation involving sinusoids, which will never be equal to unity.

Example

Let us reproduce Tam's [19] example and one of the easiest problems in acoustics, or linear wave propagation in general: a one-dimensional pulse propagation. Assuming a constant convection velocity of 1 and a finite difference approximation of the derivative, Equation 1.2 can be rewritten as:

$$\frac{\partial \phi}{\partial t} + \sum_{j=-N}^{N} a_j \phi_j = 0. \tag{1.16}$$

Where a_j are the weights of the selected numerical scheme, and N denotes the position of the nodes in this scheme. As an initial condition, a Gaussian profile will be used:

$$\phi(x,t=0) = 0.5exp\left[-ln2\left(\frac{x}{3}\right)^2\right]. \tag{1.17}$$

As Equation 1.2 does not consider any kind of dissipative behavior but only pure convection, the exact result of convecting the previous Gaussian profile should be a displacement of the initial pulse without changing its shape, i.e:

$$\phi(x,t) = 0.5exp \left[-ln2 \left(\frac{x - ct}{3} \right)^2 \right]. \tag{1.18}$$

However, let's see what happens when different numerical schemes are used and how the numerical solution approximates to the exact solution. For this example, we consider four different schemes: the first-order upwind scheme, the second-order central scheme, the sixth-order central scheme, and the DRP4 scheme.

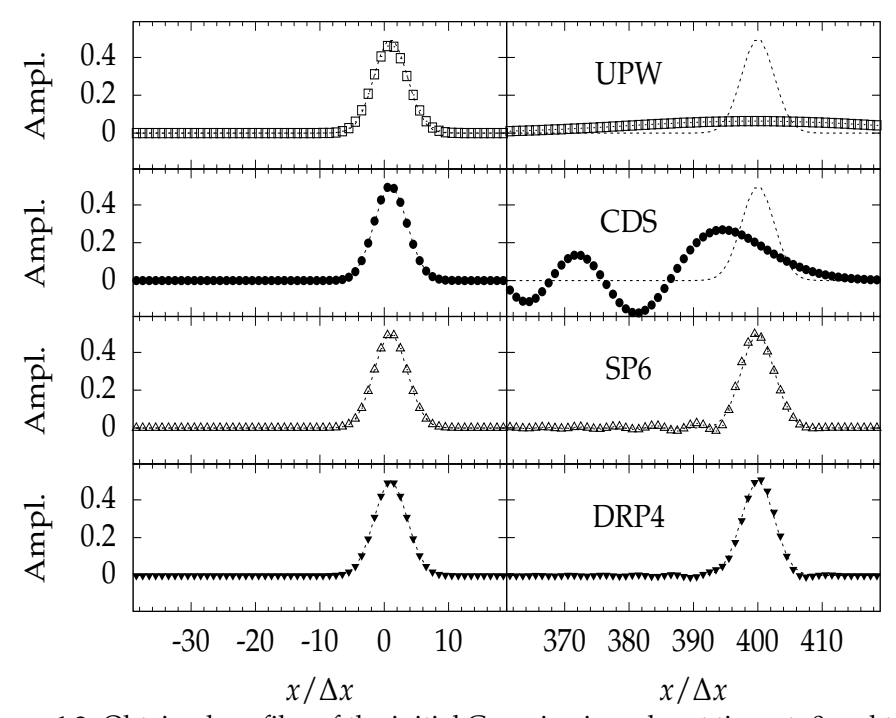


Figure 1.3: Obtained profiles of the initial Gaussian impulse at times t=0 and t=500. From top to bottom: first-order upwind scheme, second-order central scheme, sixth-order central scheme, and DRP4 scheme

As can be seen in Figure 1.3, using a dissipative scheme (Figure 1.3, top) leads to a highly diffused solution that differs significantly from the expected solution. However, even if non-dissipative schemes are used, the numerical solution can be very different from the expected analytical one as the shape is no longer attenuated but heavily distorted. This phenomenon is explained by the dispersion error introduced by the numerical scheme, which leads to a group of waves traveling at different wave speeds instead of a single one. As can be seen, raising the order of the numerical scheme leads to a reduction of the dispersion error, which, therefore, preserves the shape of the numerical solution.

1.3.2 Turbulence modelling

Due to its inherent high non-linearity, there are just a few analytical solutions for the Navier-Stokes equations. Problems that are, apparently, geometrically simple, such as a squared cavity with a fluid circulating or a simple squared cylinder immersed within a fluid in movement, can pose a challenging problem to be studied. This callenge becomes more apparent if we consider more complex geometries like the ones the industry has to deal with, such as flow around aerodynamic shapes like cars and planes. The way how the scientists and engineers have dealt with these kinds of problems has been relying on numerical simulations. Nonetheless, even with the astonishing growth in the available computational resources during the last decades, there are still problems at very high Reynolds number that cannot be afforded to be solved. This occurs due to the non-linearity of the convective term of the Navier-Stokes equations, which acts as a generator of modes or frequencies. This mechanism is explained by Kolmogorov on how the kinetic energy is transferred between scales:

- Energy-containing scales, where the energy is introduced to the system. This can be further divided into:
 - Large scales, or the scales defined by geometry.
 - Integral scales, or the scales that have more kinetic energy.
- Inertial subrange, a range of scales where the energy introduced to the system is transferred to smaller scales. This energy transfer mechanism

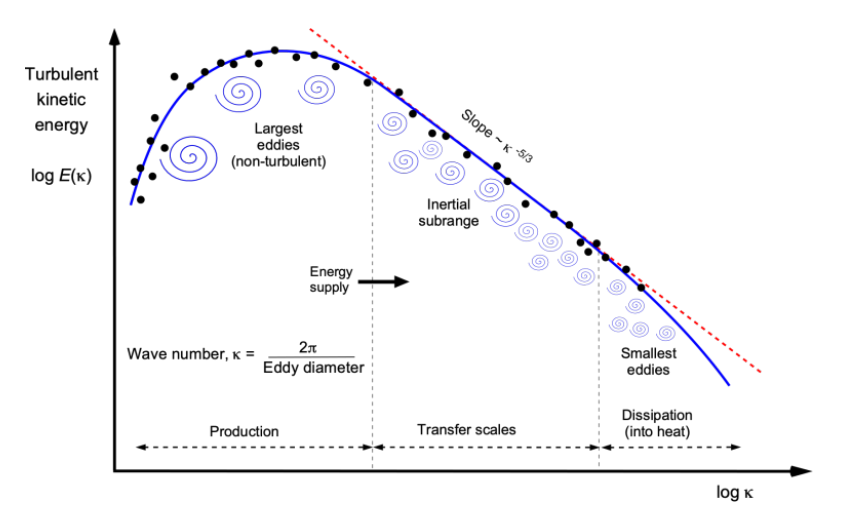


Figure 1.4: Turbulent kinetic energy wavenumber spectrum. Extracted from [20]

is replicated in a self-similar way, i.e., the kinetic energy is transferred again from small scales to smaller ones and then again and again...

• Dissipation scales or Kolmogorov scales, where the kinetic energy isconverted to thermal energy due to friction by means of viscous effects.

Figure 1.4 briefly summarises the whole energy cascade mechanism.

In summary, the problem of raising the Reynolds number can be seen as a problem where the Kolmogorov scales become smaller and smaller. And these scales should be correctly simulated when solving the Navier-Stokes equations numerically. In other words, the numerical simulation should precisely be able to reproduce the entire energy cascade mechanism. However, in order to avoid increasing the mesh to capture these scales of motion and how they interact with the bigger ones, there is an alternative. Instead of having such a fine mesh that can capture the smallest eddies, have a numerical model that reproduces the effect of these smallest scales and how they interact with the bigger scales of motion without having to simulate them. This is the key idea behind turbulence modeling.

Here, we will discuss only three different turbulence modeling techniques: Reynolds-Averaged Navier-Stokes (RANS), Large-Eddy Simulation (LES), and Detached-Eddy Simulation (DES).

Reynolds-Averaged Navier-Stokes (RANS)

RANS models are based on decoupling each field as a combination of a meanflow component and a temporal fluctuation, i.e., Reynolds decomposition. If we apply this decomposition to the i component of the velocity, we have:

$$u_i(x, y, z, t) = \overline{u}_i(x, y, z) + u'_i(x, y, z, t),$$
 (1.19)

where \overline{u}_i denotes the averaged velocity in time, and u'_i its time fluctuation. If this decomposition is repeated again:

$$\overline{u}_i = \overline{\overline{u}_i + u_i'} = \overline{\overline{u}_i} + \overline{\psi_i'} = \overline{u}_i, \tag{1.20}$$

so the equality is fulfilled.

If the Reynolds decomposition is applied to the incompressible continuity equation, this becomes:

$$\frac{\partial}{\partial x_i} (\overline{u}_i + u_i') = 0$$

$$\frac{\partial}{\partial x_i} \overline{u}_i + \frac{\partial}{\partial x_i} u_i' = 0$$

$$\frac{\partial}{\partial x_i} \overline{u}_i = 0,$$
(1.21)

which, apparently, reads identical to the non-filtered version. Nonetheless, the reader should be careful with this statement, as the filtered version in expression 1.21 only considers the mean component of the velocity, whereas the non-filtered version considers all the possible velocity fluctuations.

If this procedure is repeated again with the momentum equation:

$$\frac{\overline{\partial}}{\partial t}(\overline{u}_{i} + u'_{i}) + \overline{(\overline{u}_{j} + u'_{j})} \frac{\overline{\partial}}{\partial x_{j}}(\overline{u}_{i} + u'_{i}) = \frac{\overline{\partial}(\overline{p} + p')}{\overline{\partial}x_{i}} + \overline{v} \frac{\overline{\partial^{2}}}{\overline{\partial}x_{j}}(\overline{u}_{i} + u'_{i})$$

$$\frac{\overline{\partial}\overline{u}_{i}}{\overline{\partial t}} + \overline{u}_{j} \frac{\overline{\partial}\overline{u}_{i}}{\overline{\partial}x_{j}} + \overline{u'_{j}} \frac{\overline{\partial}u'_{i}}{\overline{\partial}x_{j}} = \frac{\overline{\partial}\overline{p}}{\overline{\partial}x_{i}} + \overline{v} \frac{\overline{\partial^{2}}\overline{u}_{i}}{\overline{\partial}x_{j}}$$

$$\frac{\overline{\partial}\overline{u}_{i}}{\overline{\partial t}} + \overline{u}_{j} \frac{\overline{\partial}\overline{u}_{i}}{\overline{\partial}x_{j}} + \overline{u'_{j}} \frac{\overline{\partial}u'_{i}}{\overline{\partial}x_{j}} = \frac{\overline{\partial}\overline{p}}{\overline{\partial}x_{i}} + v \frac{\overline{\partial^{2}}\overline{u}_{i}}{\overline{\partial}x_{j}},$$
(1.22)

where we have omitted the intermediate step, in which the zero terms are removed. If the expression 1.22 is rearranged such as follows the non-filtered version of the Navier-Stokes equations, it can be seen that an extra term has appeared:

$$\frac{\partial \overline{u}_i}{\partial t} + + \overline{u}_j \frac{\partial \overline{u}_i}{\partial x_j} = \frac{\partial \overline{p}}{\partial x_i} + \nu \frac{\partial^2 \overline{u}_i}{\partial x_j} + \frac{\partial}{\partial x_j} (\overline{u_j' u_i'}). \tag{1.23}$$

The last term in the equation, $\frac{\partial}{\partial x_j}(\overline{u_j'u_i'})$, is an extra term called the Reynolds stresses. This term appeared due to the non-linearity of the convective operator, representing the interaction between fluctuations. This means that we have more unknowns than equations; therefore, the system is not closed. A RANS model aims to offer a closure for the system of equations, i.e., compute the Reynolds stresses. In the literature we can find several options, being the most used the ones based on the Boussinesq approximation or linear eddy viscosity models. They are called "linear" as the Reynolds stresses are modeled using a linear relation with the mean flow:

$$\overline{u_j'u_i'} = 2\nu_t S_{ij} - \frac{2}{3}k\delta_{ij},\tag{1.24}$$

where

$$S_{ij} = \frac{1}{2} \left[\frac{\partial \overline{u}_j}{\partial x_i} + \frac{\partial \overline{u}_i}{\partial x_j} \right] - \frac{\partial \overline{u}_k}{\partial x_k} \delta_{ij}$$
 (1.25)

is the mean rate of strain tensor, and

$$k = \frac{1}{2}\overline{u_k'u_k'} \tag{1.26}$$

the mean turbulent kinetic energy, i.e., the trace of the Reynolds stress tensor. As can be seen, a new variable, v_t , appeared in expression 1.24. This is the so-called eddy viscosity, or turbulent eddy viscosity, due to the parallelism it has with the molecular viscosity.

However, there are still more unknowns than equations. Depending on how many variables are modeled, the RANS models can be classified as zero (or algebraic), one or two equations models.

Large-Eddy Simulation (LES)

One of the big issues regarding RANS models is their inability to capture transient phenomena. There are options within RANS, such as URANS, which stands for Unsteady RANS, that are able to work with unsteadiness. However, from a mathematical point of view, it is strange to apply a method that defines a mean flow variable, i.e., a variable that does not depend on time as in expression 1.19, but then allows this variable to vary on time.

Large Eddy Simulation takes a similar but different approach than RANS: LES is based on a spatial average instead of averaging variables on time. So, in a similar fashion to equation 1.19, the i component of the velocity can be decomposed into:

$$u_i = \tilde{u}_i + u_i^{\prime\prime},\tag{1.27}$$

where \tilde{u}_i is the spatially filtered velocity and u_i'' is the spatial subfiltered velocity. Looking at Figure 1.4, this filtering process means that the filtered velocity, \tilde{u}_i , is able to capture all the frequencies up to a certain frequency located within the inertial subrange. Therefore, all the frequencies above this cut-off frequency are included within u_i'' . In other words, u_i'' represents all the scales of motion that are too small to be resolved.

Following the same procedure as with RANS modeling, if LES filtering is applied, the momentum equation:

$$\frac{\partial \widetilde{u}}{\partial t} + \widetilde{u_{j}} \frac{\partial \widetilde{u_{i}}}{\partial x_{j}} = \frac{\partial \widetilde{p}}{\partial x_{i}} + \nu \frac{\partial^{2} u_{i}}{\partial x_{j}}$$

$$\frac{\partial \widetilde{u}_{i}}{\partial t} + \frac{\partial \widetilde{u_{i}} u_{j}}{\partial x_{j}} = \frac{\partial \widetilde{p}}{\partial x_{i}} + \nu \frac{\partial^{2} \widetilde{u}_{i}}{\partial x_{j}}$$

$$\frac{\partial \widetilde{u}_{i}}{\partial t} + \frac{\partial \widetilde{u_{i}} \widetilde{u_{j}}}{\partial x_{j}} - \frac{\partial \widetilde{u_{i}} \widetilde{u_{j}}}{\partial x_{j}} + \frac{\partial \widetilde{u_{i}} u_{j}}{\partial x_{j}} = \frac{\partial \widetilde{p}}{\partial x_{i}} + \nu \frac{\partial^{2} \widetilde{u}_{i}}{\partial x_{j}}$$

$$\frac{\partial \widetilde{u}_{i}}{\partial t} + \frac{\partial \widetilde{u_{i}} \widetilde{u_{j}}}{\partial x_{j}} = \frac{\partial \widetilde{p}}{\partial x_{i}} + \nu \frac{\partial^{2} \widetilde{u_{i}}}{\partial x_{j}} - \frac{\partial}{\partial x_{j}} (\widetilde{u_{i}} u_{j} - \widetilde{u_{i}} \widetilde{u_{j}}),$$
(1.28)

where $\widetilde{u_iu_j} - \widetilde{u_i}\widetilde{u_j}$ is equal to the residual stress tensor, or subgrid stress tensor τ_{ij} . This subgrid stress tensor can be further decomposed into three different components [21]:

$$\tau_{ij} = L_{ij} + C_{ij} + R_{ij}, \tag{1.29}$$

where

$$L_{ij} = \widetilde{u_i u_j} - \widetilde{u_i u_j}, \tag{1.30}$$

the Leonard tensor represents the interactions among the large scales,

$$C_{ij} = \widetilde{u_i u_j''} - \widetilde{u_i''} \widetilde{u_j}, \tag{1.31}$$

the Clark tensor, representing the interaction between resolved (large) and subgrid scales, and

$$R_{ij} = \widetilde{u_i'' u_j''}, \tag{1.32}$$

the Reynolds stress tensor, representing the interaction among subgrid scales. Nonetheless, even though having them separated and showing explicitly the different interactions among scales, the usual approach is to model them as a whole, i.e., model only τ_{ij} instead of L_{ij} , C_{ij} , and R_{ij} .

Among the different existing approaches to model τ_{ij} , functional or eddy viscosity models, the ones used in this work, are based on adding an artificial eddy viscosity. These eddy viscosity models treat the kinetic energy dissipation in the subgrid scales analogously to the molecular dissipation. Therefore, the filtered Navier-Stokes equations can finally be written as:

$$\frac{\partial \tilde{u}_i}{\partial t} + \frac{\partial \tilde{u}_i \tilde{u}_j}{\partial x_j} = \frac{\partial \tilde{p}}{\partial x_i} + \frac{\partial}{\partial x_j} ((\nu + \nu_{turb}) \frac{\partial \tilde{u}_i}{\partial x_j}), \tag{1.33}$$

where v_{turb} is the eddy viscosity and the one modeled by the subgrid-scale model.

Finally, the usual approach to model the eddy viscosity within functional models is to express it as a product between a characteristic length, a characteristic velocity, and a constant calibrated such that the amount of added diffusion is correct. In other words:

$$\nu_{turb} = (C_{LES}\Delta_{SGS})^2 D_{LES}. \tag{1.34}$$

Formally, what is known as the *turbulence model* is only referred to the calculus of D_{LES} . In the literature can be found a large variety of turbulence

models, ranging from the simplest one, i.e., Smagorinsky, to models that take into account the flow topology, such as WALE [22] or σ [23].

Whereas a lot of effort has been dedicated to producing more reliable turbulence models, making them sensitive to two-dimensional patterns, Δ_{SGS} has been, for a long time, the one forgotten; usually, this subgrid scale length has been computed as the cubic root of the volume, i.e., $\Delta_{vol} = Vol^{1/3}$, as it is simple and cheap to compute. Nonetheless, in recent years, the CFD community has started to become more interested in developing *advanced* subgrid scales that, as with the turbulence model, are able to take into account the different flow topologies when they are computed. Within these new ones, we can find $\tilde{\Delta}_{\omega}$ [24], Δ_{SLA} [25], or Δ_{lsq} [26], each one having produced more accurate results and being less mesh sensitive than Δ_{vol} .

Detached Eddy Simulation

LES tries to overcome RANS issues, such as its inability to capture transient phenomena or the lack of accuracy of specific RANS models when applied to flows exhibiting separation. Nonetheless, this comes with an increase in the computational effort needed to run a simulation, as LES meshes are required to be finer than their RANS counterpart. Therefore, even though LES is able to cover the main issues with RANS models, the problem is still not solved; there is not a clear winner, so some applications will still be using RANS while others will be incorporating LES as soon as the available computational power allows it.

Nonetheless, despite the considerable increase in computational resources in these last decades, pure LES simulations for general industrial applications are still many years to go. In these transition years, from RANS to LES, hybrid methods significantly boost the quality of the numerical results, when compared to RANS, without requiring the computational effort of a pure LES simulation.

Detached Eddy Simulation (DES) [27] is one of the available hybrid RANS-LES methods available. DES offers a single turbulence model that behaves as an LES where the grid is fine enough, whereas, in regions where the grid is too coarse to act as a subgrid-scale model, the model functions as a RANS model instead. In other words, near walls or shear-layers DES will behave like RANS, whereas the model will behave as an LES in those regions where the

flow *detaches*. DES is considered a non-zonal hybrid method, in the sense that a single turbulence model is used instead of explicitly using a RANS model in a region of the simulated domain and a separate LES model in the rest of the mesh. From a formal aspect, the only difference between a RANS model and its DES counterpart is the definition of L_{RANS} , a length scale present within the RANS model. DES modify this L_{RANS} to:

$$L_{DES} = min(L_{RANS}, C_{DES}\Delta), \tag{1.35}$$

where C_{DES} is the DES model constant, similar to the C_{LES} in equation 1.34, and Δ follows the same definition as in an LES model, i.e., a measure from the local grid size or local characteristic length.

However, at least in its first iteration, DES was not exempt from issues. Among others:

- If the interface between RANS and LES is located within the boundary layer, i.e., the mesh is too fine for DES to work as expected but too coarse to fully resolve turbulent structures, this causes the DES model to behave like LES prematurely. In other words, LES is entering the boundary layer whilst it should not. This triggers a sooner transition to fully resolved turbulence than expected. For this reason, this problem is also known as Grid-Induced Separation: a too-refined mesh generates a turbulence triggering sooner than it should have appeared.
- When the model transitions from RANS to LES, it changes from modeling turbulence to resolving it; the region where this occurs is known as the *Gray Area*. During this transition, the model behaves as a mixture between RANS and LES, but at the same time, it is none of them: it does not have enough modeled turbulence to be considered RANS nor enough resolved turbulence to be considered LES. So, the transition from RANS to LES behaves like a kind of laminar to turbulent transition. The main issue is that this laminar-turbulent happens in a region of the space where the fluid should be totally turbulent. So, there is a delay in the development of fully resolved turbulence within the domain.

As can be seen, the first problem is that turbulence is triggered sooner than expected, whereas the second problem is a delay in triggering thurbulence.

Regarding Grid-Induced Separation, later DES revisions have fixed this issue or reduced its effects. The most used approach is the so-called Delayed DES (DDES) [28], as this approach *delays* the mode switch between RANS and LES until it is located outside the boundary layer. This approach included the so-called shielding function, f_d , which modified equation 1.35 to:

$$L_{DDES} = L_{RANS} - f_d max(L_{RANS} - \Psi C_{DDES} \Delta, 0). \tag{1.36}$$

The new variable Ψ is a correction function published in the same paper where the shielding is presented. The inclusion of Ψ avoids erroneous or unwanted RANS model dampings near walls in LES mode.

However, the Gray Area problem is still an open issue which is addressed by Gray Area Mitigation (GAM) techniques. As the formal definition for the turbulent viscosity is the one used in 1.34, it can be seen that turbulence can be triggered by decreasing ν_t , accelerating the RANS to LES transition. This can be achieved by two different paths: reducing Δ or reducing D_{LES} . As commented previously in the LES section, new Δ definitions, such as $\tilde{\Delta}_{\omega}$, Δ_{SLA} , or Δ_{lsq} are able to contribute to the GAM by producing reduced values of Δ . At the same time, advanced turbulence models like the ones previously mentioned (σ , WALE, S3PQR,...) can also reduce ν_t values.

1.4 Objective of the thesis

Traditionally, Computational AeroAcoustics has relied on using high-order methods to obtain reliable results. The classical approach of Tam, presented in this introduction, shows a clear dependence of the numerical wavenumber on the order of the numerical scheme. High numerical methods have a broader range of wavenumbers where the difference between the numerical and analytical wavenumbers is small enough not to affect the outcome of the simulation. Nonetheless, low-order methods are a more straightforward, direct, and easy approach to ensure the symmetries of the discretized operators are kept in a general framework. This implies, for example, considering different kinds of discrete domains and not only structured uniform meshing approaches.

This presents a dilemma: what is more important? Do we need to use high-order methods so that the numerical dispersion error is kept at a minimum? Or use low-order methods, such that the symmetries of the discretized operators are ensured instead? However, there are still other questions apart from the previous ones: Is it correct to use the conclusions extracted from a method applied to evenly distributed domains when using non-uniform meshes as an argument that favours high-order schemes? Do low-order schemes behave so poorly compared to high-order schemes when using non-uniform meshing strategies?

Nonetheless, in real-world scenarios, where the Reynolds number is too high to consider a DNS, the effect of the turbulence modelling on the acoustic results should also be taken into account. As previously stated, DES presents an alternative methodology to standard LES models that can be used during the transition period until a fully LES simulation can be performed on a daily basis. Nonetheless, DES is not exempt from problems: the unphysical delay from the RANS mode to the LES mode generates numerical oscillations which cannot be distinguished from the acoustic waves. Are the standard DES approaches based on Δ_{Vol} , *Smagorinsky*, and *Spalart-Allmaras* good enough to provide accurate acoustic results? Or is it necessary to use more advanced features, such as dynamically adapting subgrid length-scales, to suppress the generation of unphysical oscillations entirely? Is the order of the numerical scheme so important when turbulence modelling is added to the equation?

This work aims to answer the previous questions at all the possible levels. First, by analyzing the differences between high and low-order methods using an extended mathematical analysis, parting from Tam's one. And second, by comparing the acoustic and hydrodynamic results of the subsonic turbulent round jet obtained from two different numerical algorithms: OpenFOAM, an open-source low-order software, and NOISEtte, an in-house high-order code. By considering a turbulent case, such as the one in this work, and forcing the usage of some turbulence modelling approach, we can analyze the effect that this selection has on the obtained hydrodynamic and acoustic results.

We believe that this thesis significantly contributes to explaining whether low-order schemes can be a viable option for the Computational AeroAcoustics community when non-uniform meshes, within a limited stretching factor range, are employed. It will also shed some light on the obtained versus expected behavior when a numerical scheme, whether low or high-order, is tested outside the usual discretization procedures, i.e., uniformly distributed nodes. Moreover, by comparing different turbulence modelling options amongst them, we can establish a general framework for the requirements they should have when used in an application within Computational AeroAcoustics.

1.5 Outline of the thesis

This thesis is divided into four chapters. The first chapter provides an introduction to Computational AeroAcoustics, making special emphasis on two of the main concerns within the community: how both the dispersion error and the turbulence closure modelling affect the validity of the results. The main contribution of the present research is presented in chapters 2 and 3, which are self-contained and could be read independently without requiring the full document. The content of those chapters has been published as original research articles in international peer-reviewed journals as well as presented at different conferences during the realization of the doctoral studies. Finally, the last chapter presents the concluding remarks of the present investigation, as well as possible investigation lines which could follow from the current work.

Chapter 2 presents an alternative methodology to compute the effects that the dispersion error has on a numerical simulation. This is done by developing an alternative measure of the dispersion error, mimicking Tam's approach based on the Fourier Transform but using eigenvectors and eigenvalues instead of the eigenfunctions of the continuous Laplacian operator. The comparison between high and low-order schemes is done by presenting the spectral properties of a representative set of different numerical schemes, considering both linear and non-linear ones with different order accuracy.

Chapter 3 presents the comparison between low and high-order schemes in a real-world scenario. The numerical results from the simulation of the turbulent subsonic round jet are discussed. This chapter also focuses on the second open area within CAA presented in this introduction: how the turbulence modelling affects the quality of the obtained results.

For this reason, the selected case is simulated in a set of refining meshes using two different numerical algorithms, to analyze the effect of the numerical scheme, and a combination between dynamic adaptinc subgrid length scales and new subgrid LES models, to analyze how the selected turbulence closure model impacts the quality of the results.

Finally, Chapter 4 summarizes and reviews the conclusions extracted in this thesis, as well as proposes future research lines that can follow the present work.

References

- [1] Centers for Disease Control, Prevention, et al. The national institute for occupational safety and health. noise and hearing loss prevention, 2017.
- [2] Thomas Münzel, Frank P Schmidt, Sebastian Steven, Johannes Herzog, Andreas Daiber, and Mette Sørensen. Environmental noise and the cardiovascular system. *Journal of the American College of Cardiology*, 71(6):688–697, 2018.
- [3] Jennifer A Deal, Nicholas S Reed, Alexander D Kravetz, Heather Weinreich, Charlotte Yeh, Frank R Lin, and Aylin Altan. Incident hearing loss and comorbidity: a longitudinal administrative claims study. *JAMA Otolaryngology–Head & Neck Surgery*, 145(1):36–43, 2019.
- [4] Michael E Braun, Stephen J Walsh, Jane L Horner, and R Chuter. Noise source characteristics in the iso 362 vehicle pass-by noise test: Literature review. *Applied Acoustics*, 74(11):1241–1265, 2013.
- [5] Hee-Min Noh. Noise-source identification of a high-speed train by noise source level analysis. *Proceedings of the Institution of Mechanical Engineers, Part F: Journal of Rail and Rapid Transit*, 231(6):717–728, 2017.
- [6] Hee-Min Noh. Wind tunnel test analysis to determine pantograph noise contribution on a high-speed train. *Advances in Mechanical Engineering*, 11(10):1687814019884778, 2019.
- [7] Hee-Min Noh, Sunghoon Choi, Sukyoon Hong, and Seog-Won Kim. Investigation of noise sources in high-speed trains. *Proceedings of the*

- *Institution of Mechanical Engineers, Part F: Journal of Rail and Rapid Transit,* 228(3):307–322, 2014.
- [8] ISO ISO. 3745, acoustics—determination of sound power levels of noise sources—precision methods for anechoic and semi-anechoic rooms. *International Organization for Standardization, Geneva, Switzerland*, 2003.
- [9] Leslie SG Kovasznay. Turbulence in supersonic flow. *Journal of the Aeronautical Sciences*, 20(10):657–674, 1953.
- [10] Christopher K W Tam and Jay C Webb. Dispersion-relation-preserving finite difference schemes for Computational acoustics. *Journal of Computational Physics*, pages 262–281, 1993.
- [11] Roland Ewert, Christina Appel, Jürgen Dierke, and Michaela Herr. Rans/caa based prediction of naca 0012 broadband trailing edge noise and experimental validation. In 15th AIAA/CEAS aeroacoustics conference (30th AIAA aeroacoustics conference), page 3269, 2009.
- [12] Michael James Lighthill. On sound generated aerodynamically ii. turbulence as a source of sound. *Proceedings of the Royal Society of London. Series A. Mathematical and Physical Sciences*, 222(1148):1–32, 1954.
- [13] J.E. Ffowcs Williams and D.L. Hawkings. Sound generation by turbulence and surfaces in arbitrary motion. *Philosophical Transactions of the Royal Society of London. Series A, Mathematical and Physical Sciences*, 264(1151):321–342, may 1969.
- [14] Jung H Seo and Young J Moon. Linearized perturbed compressible equations for low mach number aeroacoustics. *Journal of Computational Physics*, 218(2):702–719, 2006.
- [15] Roland Ewert and Wolfgang Schröder. Acoustic perturbation equations based on flow decomposition via source filtering. *Journal of Computational Physics*, 188(2):365–398, 2003.
- [16] Francesc Xavier Trias, Oriol Lehmkuhl, Assensi Oliva, Carles David Pérez-Segarra, and RWCP Verstappen. Symmetry-preserving discretization of navier–stokes equations on collocated unstructured grids. *Journal of Computational Physics*, 258:246–267, 2014.

[17] W Rozema, JC Kok, RWCP Verstappen, and AEP Veldman. A symmetry-preserving discretisation and regularisation model for compressible flow with application to turbulent channel flow. *Journal of Turbulence*, 15(6):386–410, 2014.

- [18] Sanjiva K. Lele. Compact finite difference schemes with spectral-like resolution. *Journal of Computational Physics*, 1992.
- [19] Christopher KW Tam. *Computational Aeroacoustics: a wave number approach*, volume 33. Cambridge University Press, 2012.
- [20] J Gordon Leishman. *Introduction to aerospace flight vehicles*. Embry-Riddle Aeronautical University, 2023.
- [21] Athony Leonard. Energy cascade in large-eddy simulations of turbulent fluid flows. In *Advances in geophysics*, volume 18, pages 237–248. Elsevier, 1975.
- [22] Franck Nicoud and Frédéric Ducros. Subgrid-scale stress modelling based on the square of the velocity gradient tensor. *Flow, turbulence and Combustion*, 62(3):183–200, 1999.
- [23] Franck Nicoud, Hubert Baya Toda, Olivier Cabrit, Sanjeeb Bose, and Jungil Lee. Using singular values to build a subgrid-scale model for large eddy simulations. *Physics of Fluids*, 23(8):085106, aug 2011.
- [24] Charles Mockett, Marian Fuchs, Andrey Garbaruk, Michael Shur, Philippe Spalart, Michael Strelets, Frank Thiele, and Andrey Travin. Two non-zonal approaches to accelerate RANS to LES transition of free shear layers in DES. In *Progress in Hybrid RANS-LES Modelling*, pages 187–201. Springer International Publishing, 2015.
- [25] Mikhail L. Shur, Philippe R. Spalart, Mikhail Kh. Strelets, and Andrey K. Travin. An enhanced version of DES with rapid transition from RANS to LES in separated flows. Flow, Turbulence and Combustion volume, 95(4):709–737, jun 2015.
- [26] F. X. Trias, A. Gorobets, M. H. Silvis, R. W. C. P. Verstappen, and A. Oliva. A new subgrid characteristic length for turbulence simulations on anisotropic grids. *Physics of Fluids*, 29(11):115109, nov 2017.

[27] Philippe R Spalart. Comments on the feasibility of les for wings and on the hybrid rans/les approach. In *Proceedings of the First AFOSR International Conference on DNS/LES*, 1997, pages 137–147, 1997.

[28] Philippe R Spalart, Shur Deck, Michael L Shur, Kyle D Squires, M Kh Strelets, and Andrei Travin. A new version of detached-eddy simulation, resistant to ambiguous grid densities. *Theoretical and computational fluid dynamics*, 20:181–195, 2006.

How to compute dispersion errors on Cartesian stretched meshes for both linear and non-linear operators

Main contents of this chapter has been published in:

J. Ruano, A. B. Vidal, J. Rigola and F. X. Trias. A new general method to compute dispersion errors on Cartesian stretched meshes for both linear and non-linear operators. *Computer Physics Communications*, 271, 108192, 2022.

Abstract. This chapter presents a new analysis for the dispersion error and the methodology to evaluate it numerically. Here we present the spectral properties of several convective schemes, including non-linear ones, on stretched grids for linear advection problems. Results obtained with this method when applied to uniform structured meshes converge to the results obtained with the classical method for all the studied schemes. Additionally, effects on the time step depending on which scheme is used are also analyzed using the proposed method. The extracted conclusions, taking into account both errors and

32 §2.1 Introduction

computational cost, allow for the proposal of an optimal scheme according to the selected meshing strategy.

2.1 Introduction

Discretization of the advective term in Computational Fluid Dynamics (CFD) and Computational AeroAcoustics (CAA) is still an open issue. Among others, it is well known that in order to preserve the skew-symmetry of the continuous operator, its discrete counterpart should be also skew-symmetric; this can only be achieved by means of the central convective schemes whether those proposed by Tam and Webb [1] or Bogey and Bailly [2], or the compact schemes of Lele [3], or the symmetry-preserving schemes studied by Trias et al. [4], Verstappen and Veldman [5], or Rozema et al. [6].

However, keeping the skew-symmetry of the discrete operator is not always the best option. Skew-symmetric operators do not introduce any diffusion, which means grid-to-grid numerical instabilities, which cannot be advected [1,2,7], can appear during the simulation. To avoid these artificial oscillations, numerical schemes that introduce diffusion are used. The most known approach is "up-winding" the numerical scheme, i.e. changing the stencil basis regarding the flux direction; this approach was first proposed by Courant et al. [8]. Nevertheless, upwind schemes are known to introduce excessive dissipation in the whole domain instead of just adding diffusion at points which start to diverge. Another option consists in using Total Variation Diminishing (TVD) schemes, to preserve the monocity of the solution and prevent the apparition of spurious modes [9]. However, is well known that linear TVD schemes are only first-order accurate as shown by Godunov [10]. In order to use high-order schemes without introducing spurious oscillations, non-linear techniques were developed. Flux or slope limiters [11] allow to use high-resolution schemes when the solution has no sharp gradients whereas low resolution and dissipative schemes are used when the solution has sharp oscillations. The change between these two schemes is done by means of a limiter, a function computed from the field which is being advected. Other approach that allows to keep a higher order of accuracy are the Essential Non-Oscillatory (ENO) schemes introduced by Harten et al. [12], or the Weighted Essential Non-Oscillatory (WENO) schemes of Liu et al. [13]. These schemes

use several stencils, the number and size of them depending on the order of accuracy, and the resulting scheme is constructed using the smoothest interpolating polynomial at each node. The main difference between both methods is the fact that the latter uses weights that depend on the local smoothness of the solution at the different stencils. In a similar way, Ren et al. [14,15] proposed their own dissipative numerical schemes with controllable dispersion but keeping dissipation at minimum.

When a numerical scheme is selected, is also important to know its associated error. As previously commented, upwind schemes are known to be dissipative, which means a diffusion error is introduced when are used. Regarding dissipation error, Schranner et al. [16] and Komen et al. [17] studied and quantified the effective dissipation rate in a general framework, extending their methods onto unstructured meshes. On the other hand, central schemes do not introduce any diffusion but another kind of error due to the approximation of the differential operator; this is the dispersion error. Dispersion error cannot be avoided when approximating a differential operator unless spectral methods are used. The spectral errors, i.e. the difference of the analytical wavenumber versus the numerical, have been widely studied in the bibliography. Tam and Webb [1] and Lele [3] both studied the errors of central difference schemes achieving similar conclusions. More recently, Pirozzoli [18], Fauconnier and Dick [19] and Zhao et al. [20] have extended the results of Tam and Lele onto non-linear schemes, such as ENO-WENO or schemes using flux limiters.

The classical methodology applies on the transport term of the system of Partial Differential Equations modelling wave propagation. However, it requires this term to be in advective form. For example, for the Euler Equations, one should use their characteristics form, i.e., the fluxes are calculated after applying the chain rule for the derivatives

$$\frac{\partial}{\partial t}q + \nabla \cdot f(q) = \frac{\partial}{\partial t}q + J(f, q) \cdot \nabla q = 0; \tag{2.1}$$

where $q \in \mathbb{R}^{D+2}$ are the fluid magnitudes, $f \in \mathbb{R}^{D+2}$ Eulerian fluxes, $J(f, q) \in \mathbb{R}^{(D+2)\times(D+2)}$ the Jacobian $J_{ij} = \partial f_i/\partial q_j$ and D the number of dimensions of the model. Then, the term in the center of Eq.(2.1) is projected on a unitary orthonormal basis of the Euclidean space where it is defined and one obtains the set of locally decoupled wave equations on each of the characteristic

34 §2.1 Introduction

variables

$$\frac{\partial}{\partial t}r_j + c_j \frac{\partial}{\partial s}r_j = 0, \qquad j = 1, \dots, D+2,$$
 (2.2)

where t is the time and s is a generic space coordinate. Then, the analysis studies the ratio between numerical approximations of $\partial r_j/\partial s$ and r_j in Eq.(2.2) when r_j are mono-modal sinusoids and the analytical values these ratios should take. These ratios are evaluated in the Fourier space by means of the Fourier Transform algorithm. The wave propagation speeds c_j in this procedure are assumed to be constant in space and time.

The classical analysis of Tam and Webb [1] and Lele [3] concluded that using high-order schemes is the best option to reduce dispersion error. In a similar way, Pirozzoli [18] also concluded that high-order schemes, including non-linear schemes, were the best option in order to reduce the committed dispersion error. Bogey [21] used their developed high-order schemes [2] to simulate high-Reynolds jets. Shur et al. [22,23] uses a fourth-order central -fifth-order upwind variant of the Roe scheme in the convective term when simulating jets. Fu [24] developed its very-high-order Targeted ENO (TENO) schemes to satisfy the approximated-dispersion relation when simulating, among others, very high-Mach astrophysical jets. Ewert and Schröder [25] and Seo and Moon [26] solved acoustic transport equations, instead of Navier-Stokes equations, also using high-order schemes to reduce dispersion errors. However, low-order schemes in the field of Computational AeroAcoustics are still used and achieving good results. Fuchs et al. [27,28] computed both acoustic and hydrodynamic fields of a subsonic single-stream round jet and the acoustics of a Rudimentary Landing Gear (RLG) by means of 2nd order schemes. Tyacke et al. [29] used the Kinetic Energy Preserving (KEP) discretization of Jameson [30] to compute the aeroacoustics of a jet in an industrial configuration. Both authors achieved promising results without relying on high-order discretizations of the convective term. And finally, dispersion error is not just a problem for CFD or CAA simulations, nor only tackled by engineering applications; it extends towards all physics involving wavelike phenomena. Among others, Maxwell equations have a big associated community interested on numerical dispersion. Zheng and Chen [31], or more recently Blinne et al. [32], have both studied numerical dispersion on electromagnetic equations.

The analysis employed by previous researchers does not allow to study

mesh non-uniformity. All the studies employed a Discrete Fourier Transform, which requires a uniform discretization. Nevertheless, most, if not all, of the used meshes in the CFD and CAA community are stretched or non-uniform; see, for instance, Bogey [21], Shur et al. [22, 23] or Bodony and Lele [33]. Moreover, stretching is a known mechanism that introduces numerical errors in the simulation, such as the diffusion introduced by Rai and Moin [34] to create a buffer zone to attenuate oscillations at the outflow, or the reflections studied by Vichnevetsky [35] due to an increase of the mesh size. Trefethen [36] and Vichnevetsky [35] studied how mesh anisotropy or non-uniformity introduce additional errors such as dispersive waves.

Additionally, when high-order schemes are recommended to be used, usually the temporal integration is not taken into account. However, the spatial integration is just a part of the whole integration procedure. In the methodology developed by Trias and Lehmkuhl [37] to determine the maximum time-step without having to rely on the CFL condition or the definition of a mesh size, Δx , it was concluded that the maximum eigenvalue of the discrete convective operator is the one that restricts the time-step. As can be seen in all the results of Tam and Webb [1], Lele [3] and Pirozzoli [18], the recovered wavenumbers are no other than the numerical eigenvalues of the discrete system. Analyzing their results, the maximum numerical eigenvalue rises as the order of the differential scheme does. Thus, if the maximum numerical eigenvalue rises, the maximum allowable time-step will reduce. Then, more iterations will be required if a high-order scheme is used instead of a low-order one. Consequently, it may be wrongly concluded that high-order schemes have a reduced total computational cost for a given resolution.

In conclusion, the reasons for using high-order methods on wave propagation problems in order to reduce dispersion are still open to debate. In this chapter, we develop a new methodology to overcome the limitations of the classical approach. Here, we will analyse numerically several of the most used numerical schemes on CAA, or wave-propagation simulations in general, taking into account additional parameters which usually are not considered, such as mesh stretching and the influence the scheme has in the determination of the time-step. This opens the door to dispersion error analysis on any mesh. The presented methodology is tested in a Finite Volume Method (FVM) framework, but the extracted conclusions are applicable to other discretization methodologies such as Finite Difference Method (FDM).

The rest of the chapter is organized as follows: in Section 2 the link between the classical approach used to study dispersion error and the present methodology is discussed as well as all the analytical derivation required. In Section 3 we detail how to apply this alternative methodology. In Section 4, a set of numerical tests are proposed and conducted. The results are later analysed and commented. In Section 5, a two-step study is presented: first, the effect that mesh stretching has onto the time step taking into account the order of the convective scheme is analysed. With these results, we study how the whole computational cost of the simulation is affected by using stretched meshes. Finally, in Section 6 the extracted conclusions of the whole chapter are discussed.

2.2 Theoretical background

In this section, we include the required theoretical background in functional analysis and linear algebra to fully understand the implementation of the methodology derived in section 3.

Let $f(x) : \mathbb{R} \to \mathbb{R}$ be a function that can be decomposed into a sum of sinusoids and

$$\widehat{f} = \int_{-\infty}^{\infty} f(x)e^{-2\pi ix\alpha} dx,$$
(2.3)

is its Fourier Transform. Then, the Fourier Transform of the spatial derivative

$$f' = \frac{d}{dx}f(x),\tag{2.4}$$

of f is:

$$\widehat{f}'(\alpha) = i\alpha \widehat{f}. \tag{2.5}$$

However, the previous expressions do not hold when the space is discretized. Namely, taking a discretization of the physical space defined by $\Omega = \{\omega_1(x), \omega_2(x), \omega_3(x), \dots, \omega_N(x)\}^T$, f is approximated with

$$f(x) \simeq \sum_{j=1}^{N} \omega_j(x) f_j = \Omega \cdot f,$$
 (2.6)

where the "N" scalars f_j are the components of the array $f = \{f_1, f_2, f_3, \dots, f_N\}^T \in \mathbb{R}^N$. If a Finite Difference discretization is selected, the different elements of Ω would be equal to:

$$\omega_i(x) = \begin{cases} 1 & \text{if} & x = x_i \\ 0 & \text{elsewhere} \end{cases}$$
 (2.7)

In case a Finite Volume approach is selected, with non-overlapping volumes, the elements of Ω would be:

$$\omega_i(x) = \begin{cases} 1 & \text{if} & x \in V_i \\ 0 & \text{elsewhere} \end{cases}$$
 (2.8)

Where V_i denotes the i^{th} control volume of the discretization. Assuming the discretization is uniform and the physical space is 1D, one can approximate the derivative f' with

$$f'(x) \simeq \sum_{i=1}^{N} \omega_j(x) \sum_{k=1}^{N} a_{j,k} f_k.$$
 (2.9)

The previous equation can be written in a matrix-vector form as:

$$f'(x) \simeq \Omega^T A f, \tag{2.10}$$

where the matrix *A* stands for the discrete differential operator.

Applying the shifting theorem and the derivative theorem (see Tam [1,38]), the Fourier Transforms of f and the discrete approximation to its derivative are related with

$$\widehat{f}'(\alpha) \approx \frac{1}{\Delta x} \left[\sum_{k} a_k e^{ik\alpha \Delta x} \right] \widehat{f}(\alpha).$$
 (2.11)

And the numerical wavenumber $\tilde{\alpha}$ according to the classical analysis follows straighforwardly:

$$i\widetilde{\alpha}\widehat{f} = \frac{1}{\Delta x} \left[\sum_{k} a_{k} e^{ik\alpha \Delta x} \right] \widehat{f} \Longrightarrow \widetilde{\alpha} = \frac{-i}{\Delta x} \left[\sum_{k} a_{k} e^{ik\alpha \Delta x} \right].$$
 (2.12)

But this definition assumes a uniform 1D mesh, as it uses a sole Δx . To broaden the concept of numerical wavenumber to non-uniform meshes where Eq.(2.11) does not apply, the eigenvalues of the derivative operator can be studied. More precisely, the differences between the analytical and numerical eigenvalues of the derivative operator. To extend the concept to non-uniform discretizations, we realize that the Fourier Transform projects functions into the space of eigenfunctions of the derivative operator of evenly distributed domains, i.e., Euclidean spaces or uniformly discretized domains. Thus, instead of projecting the function f in the space of sinusoids, we propose to project f onto the space of eigenfunctions of the derivative operator, which does not coincide with sinusoids in non-uniform discretizations. Then, Eq.(2.5) must be rewritten as:

$$f'^{\dagger}(\lambda) = \lambda f^{\dagger}(\lambda),$$
 (2.13)

where the projection, $()^{\dagger}$, is computed as:

$$f'^{\dagger}(\lambda) = \int_{-\infty}^{\infty} f'(x) \cdot \beta(\lambda, x) \, dx;$$

$$f^{\dagger}(\lambda) = \int_{-\infty}^{\infty} f(x) \cdot \beta(\lambda, x) \, dx,$$
(2.14)

and β and λ are the appropriate set of eigenfunctions and eigenvalues extracted from the first-order derivative operator. If we let

$$\langle \xi \mid \psi \rangle_{\Omega_{\mu}} = \int_{\Omega_{\mu}} \xi(\mu) \overline{\psi}(\mu) d\mu,$$
 (2.15)

be the inner product of $\{\xi, \psi\} \in \mathcal{L}^2(\Omega_\mu, \mu)$, where $\mathcal{L}^2(\Omega_\mu, \mu)$ is the space of square Lebesgue-integrable functions $\psi : \Omega_\mu \subset \mathbb{R} \mapsto \mathbb{C}$ and $\overline{\psi}$ the complex conjugate of ψ . We can rewrite the projections in a more compact form:

$$f'^{\dagger}(\lambda) = \langle f' | \beta \rangle_{\Omega_x}; f^{\dagger}(\lambda) = \langle f | \beta \rangle_{\Omega_x}.$$
 (2.16)

Once discretized, an implicit relation between the numerical eigenvalue

and the analytical one is found:

$$\widetilde{\lambda} = \frac{\widetilde{f'}^{\dagger}}{\widetilde{f}^{\dagger}} = \frac{\langle Af \mid \beta \rangle}{\langle f \mid \beta \rangle}, \tag{2.17}$$

where the discrete inner product is defined as:

$$\langle \boldsymbol{\phi} \mid \boldsymbol{\psi} \rangle = \sum_{j=1}^{N} \left(\phi_{j} \sum_{k=1}^{N} \left\langle \omega_{j} \mid \omega_{k} \right\rangle_{\Omega_{x}} \overline{\psi}_{k} \right). \tag{2.18}$$

We remark that ω_j and ω_k are the j and k terms of the discretization Ω defined at the beginning of this section.

Both methodologies, the classical and that defined in Eq.(2.17), assume that the derivative can be explicitly projected into a selected space of functions and depends linearly on the original f. For more complicated derivation processes, e.g. non-linear differential operators, these expressions are not valid. Consequently, another method is proposed.

Namely, let $\Phi = \{\phi_{-N}(x), \phi_{-N+1}(x), \dots \phi_{-1}(x), \phi_0(x), \phi_1(x), \phi_2(x), \dots \phi_N(x)\}$ be an orthonormal basis of functions of $\Omega_x \subset \mathbb{R}$, i.e,

$$\langle \phi_m \, | \, \phi_n \rangle_{\Omega_x} = \delta_{mn},$$
 (2.19)

where δ_{mn} is the Kronecker's delta.

One can thus define a mapping $T: \mathcal{L}^2(\Omega_x, x) \mapsto \mathbb{C}^{2N+1}$; $T: f(x) \mapsto (\alpha_m) \in \mathbb{C}^{2N+1}$, where

$$\alpha_m = \langle f \, | \, \phi_m \rangle_{\Omega_x} = \int_{\Omega_x} f(x) \overline{\phi_m}(x) \, dx, \tag{2.20}$$

is the projection of f(x) onto the m function Φ . Under the pertinent smoothness of f criterion,

$$f(x) \simeq S_N = \sum_{m=-N}^{N} \alpha_m \phi_m(x); \quad \lim_{N \to \infty} S_N = f(x). \tag{2.21}$$

This defines the inverse mapping $T^{-1}: \mathbb{C}^{2N+1} \mapsto \mathcal{L}^2(\Omega_x, x), T: (\alpha_m) \in \mathbb{C}^{2N+1} \mapsto f(x)$.

The derivative $f' = \frac{d}{dx}f(x)$ can also be expressed in terms of its projection on the set of functions of Φ :

$$f'(x) \simeq S'_N = \sum_{m=-N}^N \alpha_m \phi'_m(x) \simeq \sum_{m=-N}^N \left(\alpha_m \sum_{n=-N}^N \gamma_{mn} \, \phi_n(x) \right), \qquad (2.22)$$

where

$$\gamma_{mn} = \langle \phi'_m \, | \, \phi_n \rangle_{\Omega_m}. \tag{2.23}$$

This holds on the orthonormality of the functions of Φ :

$$\gamma_{mn} = \left\langle \phi'_{m} \mid \phi_{n} \right\rangle_{\Omega_{x}} = \left\langle \sum_{p=-N}^{N} \gamma_{mp} \phi_{p}(x) \mid \phi_{n} \right\rangle_{\Omega_{x}} \\
= \sum_{p=-N}^{N} \gamma_{mp} \left\langle \phi_{p} \mid \phi_{n} \right\rangle_{\Omega_{x}} = \sum_{p=-N}^{N} \gamma_{mp} \delta_{pn} = \gamma_{mn}. \tag{2.24}$$

We define the matrix Γ , where its elements $(\Gamma)_{mn} = \gamma_{mn}$ represent the projections of the derivatives of ϕ_m with respect to "x" on ϕ_n .

 Γ characteristics are determined by the selected basis of functions Φ and the properties of the derivative operator. Assuming null contributions from boundaries and integrating by parts, it is straightforward to show that the derivative operator is skew-Hermitian with respect to the inner product of Eq.(2.15), i.e.,

$$\left\langle \frac{d}{dx}\xi \mid \psi \right\rangle_{\Omega_x} = -\left\langle \xi \mid \frac{d}{dx}\psi \right\rangle_{\Omega_x}.$$
 (2.25)

Thus, Γ is skew-Hermitian too.

Using an approximate derivative operator $\frac{\widetilde{d}}{dx}(\cdot)$, one gets $\widetilde{\Gamma} \in \mathbb{C}^{2N+1 \times 2N+1}$ instead. Making a parallelism with Eq.(2.17), the errors associated with using approximate differential operators to approximate derivatives are the deviations of $\widetilde{\gamma}_{mn}$ from γ_{mn} . Finally, to ease the analysis, Φ can be chosen such that Γ is diagonal and known, i.e., ϕ_m is an eigenfunction of the derivative. Then, the possible errors in $\widetilde{\Gamma}$ are:

- $\widetilde{\gamma}_{mn} \neq 0$ if $m \neq n$,
- $Re(\widetilde{\gamma}_{mm}) \neq 0$, and

•
$$\frac{Im(\widetilde{\gamma}_{mm})}{\lambda_m} \neq 1$$
,

where $\lambda_m \in \mathbb{I}$ is the eigenvalue of the derivative on ϕ_m . A methodology to compute these errors is described in the next section.

2.3 Methodology

When functions are approximated with discretizations as in Eq.(2.6) to operate with arrays of scalars, the differential operators of the equations describing some physical phenomena should be approximated accordingly. For example, if f is the discrete representation of f(x) on $\Omega = \{\omega_1(x), \omega_2(x), \ldots, \omega_N(x)\}$ as defined in Eq.(2.6), the discrete representation of an approximation to its derivative f' is represented on $M = \{m_1(x), m_2(x), m_3(x), \ldots, m_M(x)\}$. The different discretizations methodologies of CFD contemplate $M \neq \Omega$. However, it is common to project the calculated derivatives onto the original Ω (see, e.g. [4]) in the following computation steps. Here, we focus on the compound process $A : \mathbb{R}^N \mapsto \mathbb{R}^N$, i.e. the approximation to the derivative $f \mapsto A(f)$ and its projection onto Ω . Since differential operators are linear, their discrete counterparts should be linear too. Therefore, A(f) = Af; $A \in \mathbb{R}^{N \times N}$. Splitting A into the Hermitian, D, and skew-Hermitian, C, parts [39],

$$C = \frac{1}{2} (A - A^*); (2.26)$$

$$D = \frac{1}{2} (A + A^*); (2.27)$$

$$A = C + D, \tag{2.28}$$

where $(\cdot)^*$ indicates the conjugate transpose. The previous matrices have interesting properties regarding the inner product:

$$\begin{aligned}
\langle C\psi \mid \psi \rangle &\in \mathbb{I} \\
\langle D\psi \mid \psi \rangle &\in \mathbb{R} \\
\langle C\psi \mid \eta \rangle &= -\langle \psi \mid C\eta \rangle \\
\langle D\psi \mid \eta \rangle &= \langle \psi \mid D\eta \rangle ,
\end{aligned} (2.29)$$

where $\{\boldsymbol{\psi}, \boldsymbol{\eta}\} \in \mathbb{C}^N$.

Both matrices C and D are related, respectively, to the real and the imaginary part of the γ scalars of Eq.(2.23). For a given discretization, these scalars can be numerically calculated:

$$\widetilde{\gamma}_{mn} = \langle A \boldsymbol{\phi}_{m} | \boldsymbol{\phi}_{n} \rangle
\widetilde{\gamma}_{mn}^{C} = Im(\widetilde{\gamma}_{mn}) = \langle C \boldsymbol{\phi}_{m} | \boldsymbol{\phi}_{n} \rangle
\widetilde{\gamma}_{mn}^{D} = Re(\widetilde{\gamma}_{mn}) = \langle D \boldsymbol{\phi}_{m} | \boldsymbol{\phi}_{n} \rangle .$$
(2.30)

This development holds because Φ is orthonormal and due to the nature of the skew and Hermitian operators. They can be calculated from A:

$$\widetilde{\gamma}_{mn}^{C} = \langle C\boldsymbol{\phi}_{m} \mid \boldsymbol{\phi}_{n} \rangle = \frac{\langle A\boldsymbol{\phi}_{m} \mid \boldsymbol{\phi}_{n} \rangle - \langle \boldsymbol{\phi}_{m} \mid A\boldsymbol{\phi}_{n} \rangle}{2}$$

$$\widetilde{\gamma}_{mn}^{D} = \langle D\boldsymbol{\phi}_{m} \mid \boldsymbol{\phi}_{n} \rangle = \frac{\langle A\boldsymbol{\phi}_{m} \mid \boldsymbol{\phi}_{n} \rangle + \langle \boldsymbol{\phi}_{m} \mid A\boldsymbol{\phi}_{n} \rangle}{2},$$
(2.31)

where the values of $\widetilde{\gamma_{mn}}$ are the different elements of the matrix $\widetilde{\Gamma}$. To simplify the analysis, we propose to compute the root mean square of the second index of the values of $\widetilde{\gamma}$,

$$\widetilde{\lambda}_{m}^{C} = \sqrt{\sum_{n} \left(\frac{\langle A \boldsymbol{\phi}_{m} \mid \boldsymbol{\phi}_{n} \rangle - \langle \boldsymbol{\phi}_{n} \mid A \boldsymbol{\phi}_{m} \rangle}{2} \right)^{2}}$$

$$\widetilde{\lambda}_{m}^{D} = \sqrt{\sum_{n} \left(\frac{\langle A \boldsymbol{\phi}_{m} \mid \boldsymbol{\phi}_{n} \rangle + \langle \boldsymbol{\phi}_{n} \mid A \boldsymbol{\phi}_{m} \rangle}{2} \right)^{2}}.$$
(2.32)

This procedure allows a faster comparison between the analytical value and the recovered numerical ones. Thus, if the recovered $\widetilde{\lambda}_m^D$ is not null, the differential operator will have diffusive behaviour. If the ratio between $|\widetilde{\gamma}_{mm}|$ and $\widetilde{\lambda}_m^C$ is smaller than the unity, then the off-diagonal values of $\widetilde{\Gamma}_{mn}$, which should be zero, will have a non-zero value. And finally, the ratio between $\widetilde{\lambda}_m$ and the reference parameter indicates the deviation of the numerical discretization from its expected value.

In summary, given a set of approximations of differentiating operators $\{A_1, A_2, \ldots, A_P\}$, their dispersion properties on a representative mesh can be compared after computing the quantities $\widetilde{\lambda}_m^{C_j}$ and $\widetilde{\lambda}_m^{D_j}$ for each element ϕ_m of an orthonormal basis and discrete operator A_j . The following subsections address the evaluation of A_j and the selection of an appropriate orthonormal basis Φ .

2.3.1 Evaluating the gradient

To evaluate the approximations of the derivative operators we propose to substitute Eq.(2.2) with

$$\frac{\partial r_j}{\partial t} + C(c_j, r_j) = 0, \qquad j \in [1, D+2]; \tag{2.33}$$

where $C(c_j, r_j)$ is the convection operator on r_j . After this, approximations of derivative operators can be easily obtained with $c_j = 1$. Notice that in the continuous space or with constant c_j Eqs. (2.2) and (2.33) are equivalent. In practical simulations, the discrete convective operator is an isomorphism, i.e. $C: \Omega \mapsto \Omega$. Hence, this resolves the eventual problem of the different basis pointed out in former paragraphs of this section. Furthermore, Eq.(2.33) is advantageous in discretizations where c_j is not constant. In fact, in the Euler Equations in the form of Eq.(2.33), $c_j: \mathbb{R}^{D+2} \mapsto \mathbb{R}$; $c_j(r)$ and their spatial variations can only be neglected for small perturbations (e.g. acoustics).

However, this assumption does not hold when simulating hydrodynamic regions. In these regions, the spatial variations of r are of the same order of magnitude and spatial variations of c_j cannot be neglected. Nonetheless, the literature shows how low-dispersion arguments based on the classical methodology have been employed to support using high-order numerical schemes in these regions. We expect that the dispersion analysis developed here with the derivatives computed via Eq.(2.33) will allow comparing schemes in hydrodynamic regions.

2.3.2 Selection of an orthonormal basis

The method described above has to be applied on an appropriate orthonormal basis of the discrete fields, Φ . The classical analysis [1,3,38] performs the dispersion error analysis on uniform structured meshes. On them, it is straightforward to use the projections of sinusoids on the canonical basis Ω^0 , i.e., define a change of basis of the type $B: \mathbb{R}^N \to \mathbb{R}^N$. For example, in Finite Differences or Finite Volumes formulations, one can use $b_{jk} = \langle \sin(jx) | \omega_k^0 \rangle_{\Omega_x}$. However, in non-uniform or unstructured meshes, this procedure does not generate an orthonormal basis.

For these cases, we propose to use the eigenvectors of the discrete Laplacian operator defined on such meshes. This basis is used in signal analysis and

related fields (see Shuman et al. [40]). Among others, the properties of the eigenvectors of the discrete Laplacian operator are:

- The eigenvectors are orthonormal.
- In evenly spaced domains, the eigenvectors are discretized sinusoids.
- In the continuous limit, its eigenvectors and eigenvalues collapse into the eigenfunctions of its continuous counterpart, i.e. sinusoids.
- They retain the concept of mesh connectivity.

Furthermore,

$$L = G^*G, (2.34)$$

where $L \in \mathbb{R}^{N \times N}$ is a discrete Laplacian, $G \in \mathbb{R}^{M \times N}$ a discrete gradient (see [41]) and G^* the conjugate-transpose of G. It is important to notice that G is not necessarily the differentiating operator on which the dispersion error analysis is to be conducted but a differencing operator that holds the equality. Actually, Φ should be independent of the scheme under study to allow comparisons if several of them will be tested.

The Singular Value Decomposition of G relates its right-eigenvectors $\{g_1, g_2, \ldots, g_N\}$ and singular values $\{g_1, g_2, \ldots, g_N\}$ with the eigenvectors $\{l_1, l_2, \ldots, l_N\}$ and eigenvalues of $\{l_1, l_2, \ldots, l_N\}$ of L. Specifically, $g_n = \sqrt{l_n}$ and $g_n = l_n$.

Thus, any scheme under analysis will be compared to a reference gradient. With this, we propose to calculate the quantities of Eq.(2.32) with $\Phi = \{l_1, l_2, \dots, l_N\}$ and $\lambda_j = \sqrt{l_j}$ for all $j \in [1, N]$.

The discrete eigenvectors of a 2nd order discrete symmetric Laplacian operator are shown in figure 2.1. The Laplacian matrix has been constructed such the identity vector lies in the kernel of the matrix. To achieve this, the off-diagonal elements are computed as:

$$l_{ij} = \frac{A_{ij}}{\overrightarrow{d_{ij}} \overrightarrow{n_{ij}} \frac{V_i + V_j}{2}},$$
(2.35)

whereas the diagonal terms are the negative sum of the off-diagonal terms:

$$l_{ii} = -\sum_{i \neq j} l_{ij}. \tag{2.36}$$

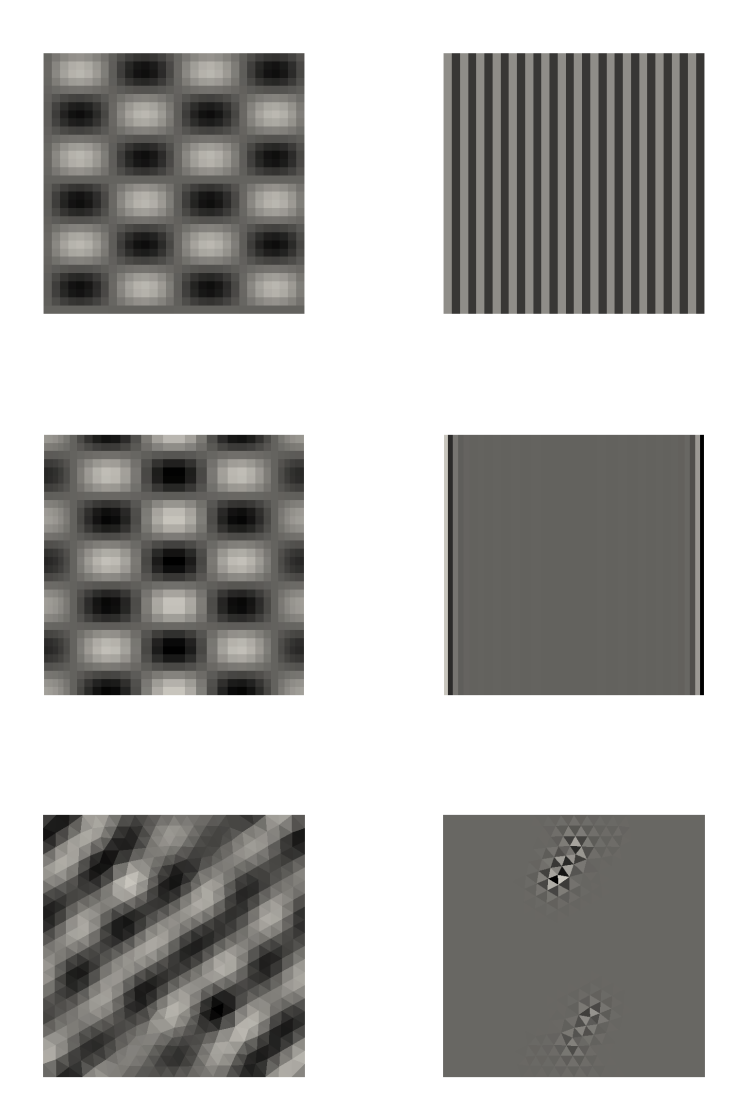


Figure 2.1: Examples of discrete eigenvectors in two-dimensional meshes. Left: low eigenvalue associated, right: high eigenvalue associated. Top: uniform mesh; Middle: stretched mesh; Bottom: unstructured mesh.

 A_{ij} is the intersection area between volumes i and j, $\overrightarrow{n_{ij}}$ its normal vector, $\overrightarrow{d_{ij}}$ the distance vector between centroids and V_i and V_j , the volumes i and j.

The results resemble, into some extent, a discrete sinusoid; this is more obvious when low modes are selected. When higher modes are selected, as on the figures on the right, this similarity can be lost if non-uniform, or non-structured meshes are used.

2.3.3 Effect of the phase

For non-linear differential schemes as well as when non-uniform meshes are used, independently if linear or non-linear discretization schemes are employed, the discrete function is distorted. This effect changes the function shape and aliases the derivative into several modes instead of a single one. Consequently, this difficults obtaining the numerical eigenvalue or wavenumber to compare with the analytical one. Fauconnier and Dick [19] solved this problem, in uniform meshes, when using non-linear schemes, by setting the phase of each frequency as a random parameter, obtaining a numerical wavenumber which depends on both analytical wavenumber and phase. Repeating this process 5000 times and then computing the average they obtained the averaged numerical wavenumber. Another point of view of this method can be that they chose an orthonormal basis of the mesh, i.e. discrete sinus and cosinus, which were not the eigenbasis of their discrete operator. Then, they rotated that basis 5000 times. On average, all the rotated basis will oscillate around the eigenbasis of his differential operator.

Algebraically, this implies performing a rotation with a random phase for each pair of eigenvectors, i.e. if the basis of eigenvectors consists in 2N+1 or 2N+2 vectors then N rotations will be performed each time. However, thanks to the specific form of these kinds of rotations , it is very easy to concatenate N rotations. In fact, we don't need to perform N matrix multiplications as N chained rotations but a single matrix due to the specific form of the rotation

we are using:

$$R = \begin{pmatrix} 1 & 0 & 0 & \cdots & 0 & 0 \\ 0 & \cos(\alpha_1) & \sin(\alpha_1) & \cdots & 0 & 0 \\ 0 & -\sin(\alpha_1) & \cos(\alpha_1) & \cdots & 0 & 0 \\ \vdots & \vdots & \vdots & \ddots & \vdots & \vdots \\ 0 & 0 & 0 & \cdots & \cos(\alpha_N) & \sin(\alpha_N) \\ 0 & 0 & 0 & \cdots & -\sin(\alpha_N) & \cos(\alpha_N) \end{pmatrix}$$
(2.37)

And the eigenvectors in the new rotated base:

$$E' = RE, (2.38)$$

where E' is the matrix containing the eigenvectors in the new base and E the eigenvectors in the original one.

It is important to notice that for uniform meshes, the Laplacian eigenvalues appear in pairs: each eigenvalue appears two times, except 0 and the maximum one if the discrete mesh has an even number of nodes. However, non-uniform meshes do not hold this property. Consequently, this methodology computes an effective eigenvalue, which is the average between the two consecutive eigenvalues associated to the rotated eigenvectors.

Therefore, the analysis of Fauconnier and Dick can be extended to nonuniform meshes by using the concept of rotation matrix instead of the random phase.

2.3.4 Studying sinusoids or other functions

It may be argued that the discrete eigenvalues of L are not directly related to waves in the physical, continuous, space. However, the closer the discrete L approximates the continuous ∇^2 , the closer are its eigenvalues and eigenvectors to resemble physical waves. Put short, using high order L reduces the errors , at least for long wavelengths with respect to the mesh characteristic spacing. But still, the user of the present methodology does not have strict control of the wavelengths that will be the eigenvalues of L on a mesh.

The following method allows to evaluate dispersion errors for any function f and, in particular, a sinusoid with wavenumber "k", e.g., $f(k, x) = \sin(kx)$. Expressing f on Ω , $f(k, x) \simeq \sum_m a(k)_m \phi_m(x)$, with $a(k)_m = \langle f | \phi_m \rangle_{\Omega_x}$, which

are the coordinates of the sinusoid function in the eigenvectors basis. The derivative is approximated by

$$f'(k, x) \simeq \frac{d}{dx} \sum_{m} a(k)_{m} \phi_{m}(x) = \sum_{m} a(k)_{m} \phi'_{m}(x)$$

$$= \sum_{m} a(k)_{m} \sum_{n} \gamma_{mn} \phi_{n}(x),$$
(2.39)

We can compute an approximation to the classical dispersion error:

$$S(k,l) = \left\langle \widetilde{f}'(k,x) \mid f(l,x) \right\rangle_{\Omega_x} \simeq \left\langle \widetilde{\Gamma} \boldsymbol{a}(k) \mid \boldsymbol{a}(l) \right\rangle. \tag{2.40}$$

where $\widetilde{\Gamma}$ is defined as in Eq.(2.31). As a particular case, when l is equal to k, the above definition becomes the usual expression of dispersion error on evenly distributed meshes, i.e. how the derivative of a mode projects in the same mode:

$$S(k,k) = \left\langle \widetilde{f}'(k,x) \mid f(k,x) \right\rangle_{\Omega_x} \simeq \left\langle \widetilde{\Gamma} a(k) \mid a(k) \right\rangle. \tag{2.41}$$

Thus, the presented methodology is able to numerically approximate the results in sinusoids basis on general meshes. On the other hand, the classical analysis cannot cope with non-uniform meshes due to the fact it requires performing a Discrete Fourier Transform.

2.4 Numerical tests

As application tests to study in this work, we have selected one-dimensional Cartesian structured meshes with different stretchings. The main reason for this selection is that structured meshes are one of the most used in the field of CFD and CAA. Due to the fact our developed methodology does not require uniform meshing, the results obtained in this work can shed some light on dispersion phenomena in this kind of meshes. The stretching procedure used in this thesis consists in applying a Poisson ratio between two consecutive control volumes, i.e. $\Delta x_{i+1} = r\Delta x_i$, with r = 1 + s, where s is the percentage of stretching. In Figure 2.2, we attach some images of the obtained meshes using this procedure that are used in this work. In this thesis we apply the aforementioned methodology to several of the most used convective schemes

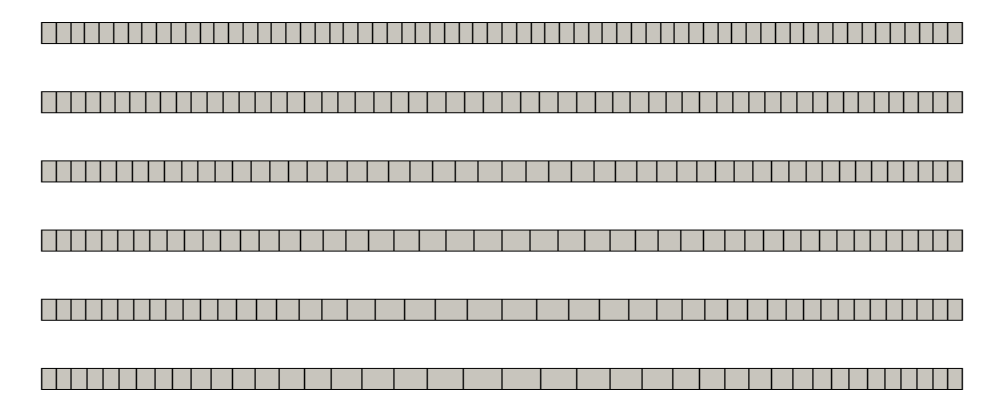


Figure 2.2: Used meshes with increasing stretching factor from top (0%) to bottom (5%) and equal minimum mesh size.

in CAA, or in wave-propagation like simulations in general. We have divided the tested convective schemes into two groups: linear, which compute the weights of each stencil just once at the beginning of the simulation, and nonlinear schemes, whose weights depend on the field being computed. Within the linear schemes, we have chosen a second-order symmetry preserving (SP2), sixth-order symmetry preserving (SP6), fourth and sixth-order dispersion relation preserving (DRP4,DRP6) [1] and sixth-order moving least-squares scheme (MLS3) [42,43]. The selection of the high-order schemes is not trivial: SP6, DRP6 and MLS3 have the same formal order of accuracy using different weights or formulation. On the other hand, SP6, DRP4 and MLS3 use the same stencils. The non-linear schemes are: first-order upwind (UPW), third, fifth and seventh order WENO schemes (WENO3, WENO5, WENO7) [44], and second-order total variation diminishing (TVD) schemes with Superbee, Minmod and Van Leer limiters (SB,MM,VL). These numerical tests will be done with several Cartesian structured meshes with different stretching ratios, as well as different minimum mesh sizes; the total size of the domain will be kept constant. In Figure 2.2, we show a set of meshes with the same minimum mesh size and different stretching ratios. The main reason why we do not include two or three-dimensional Cartesian structured meshes in our study is that the effective wavenumber in 2D and 3D domains is a linear combination of 1D wavenumbers. This was also analysed by Lele [3] or Nogueira [43],

by their polar plots of different wavenumbers taking into account directivity, i.e. different combinations of wavenumbers in the Cartesian directions which produce the same equivalent wavenumber. For example, it is well known that for first-order upwind schemes and second-order central schemes the recovered wavenumber is:

$$\widetilde{k_x} \Delta x = \sin(k_x \Delta x). \tag{2.42}$$

If two dimensions are considered and the same scheme is used at each direction, the relation (2.42) holds for each direction. This means that the effective wavenumber becomes:

$$\widetilde{k} = \sqrt{\widetilde{k_x}^2 + \widetilde{k_y}^2} = \sqrt{\left(\frac{\sin(k_x \Delta x)}{\Delta x}\right)^2 + \left(\frac{\sin(k_y \Delta y)}{\Delta y}\right)^2}.$$
 (2.43)

And transforming k_x and k_y to depend on the effective wavenumber, k:

$$k_x = k\cos(\theta) k_y = k\sin(\theta),$$
 (2.44)

where θ is the directivity angle. Replacing:

$$\widetilde{k} = \sqrt{\left(\frac{\sin(k\cos(\theta)\Delta x)}{\Delta x}\right)^2 + \left(\frac{\sin(k\sin(\theta)\Delta y)}{\Delta y}\right)^2}.$$
 (2.45)

The numerical wavenumber is made non-dimensional by dividing it between the analytical one. Thus, if dispersion relation holds, the expected shape of the plot is the unitary circle. However, dispersion error at each direction distorts the plot, as can be seen in Figure 2.3.

The test functions used to compute dispersion error are the discrete eigenvectors computed from the discrete Laplacian. The Laplacian is discretized as in Eqs.(2.35,2.36), following a second-order approximation of the differential operator, ensuring symmetry of the obtained matrix, and with periodic boundary conditions. Once constructed, the eigenvalues and eigenvectors of the discrete Laplacian matrix are calculated by means of QR reduction algorithm present in GNU scientific library package [45]. The obtained test functions are then convected by using each differential scheme previously presented.

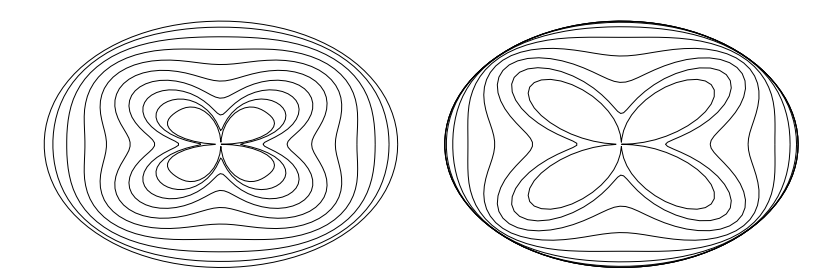


Figure 2.3: Normalized polar plot of wave number anisotropy for wavenumbers $\frac{k\Delta}{\pi} = \frac{1}{10}, \frac{2}{10}, ... \frac{9}{10}, \frac{10}{10}$. Left: second-order central difference scheme; Right: fourth-order DRP scheme.

The convective term is linearized, i.e. constant advection velocity, in order to compare the presented method with the classical approach due to the fact the latter implies a linear convective term. This means the studied convective term in one direction is:

$$C((1,0,0), \boldsymbol{\phi})_i = \frac{\delta}{\delta x} \boldsymbol{\phi}_i. \tag{2.46}$$

And its discrete counterpart in a Finite Volume framework:

$$\frac{d}{dx}\boldsymbol{\phi}_i \simeq \frac{1}{V_i} \sum_{f \in V_i} \phi_f A_f n_x, \tag{2.47}$$

where V_i is the volume of control volume i, ϕ_f the interpolated value of ϕ at face f, A_f the surface of face f and n_x the x component of the normal vector of face f.

For the sake of clarity, in Table 2.1 we have summarized the main characteristics of used meshes , i.e. minimum and maximum mesh sizes, Δx_{Min} and Δx_{Max} , and the number of control volumes, NCV, as well as the legend symbols of the results shown in this section. In the same table, we summarize the acronyms of the different convective schemes tested. However, we want to remark that the objective of some of the figures that we show in this study is not to analyse each case independently; we want to study common trends that allow to extract more general conclusions. Therefore, it is possible that the reader wouldn't be able to fully check each studied case in the next figures, but just the common trends that those cases have.

Table 2.1: List of the different used meshes and the symbol of the results obtained when using them and the acronyms of the convective schemes.

Stretching 0 %				Stretching 1 %			
Δx_{Min}	Δx_{Max}	NCV	Symbol	Δx_{Min}	Δx_{Max}	NCV	Symbol
0.03125	0.03125	32		0.03125	0.03628	30	+
0.01563	0.01563	64		0.015623	0.02065	56	\odot
0.00781	0.00781	128		0.00781	0.01285	100	▼
0.00391	0.00391	256		0.00391	0.00892	166	0
0.00195	0.00195	512		0.00195	0.00698	256	•
Stretching 2 %				Stretching 3 %			
Δx_{Min}	Δx_{Max}	NCV	Symbol	Δx_{Min}	Δx_{Max}	NCV	Symbol
0.03125	0.04206	30	X	0.03125	0.04727	28	*
0.01563	0.02563	50	•	0.01563	0.03084	46	Δ
0.00781	0.01795	84	\Diamond	0.00781	0.02332	74	♦
0.00391	0.01415	130	•	0.00391	0.01927	108	•
0.00195	0.01208	184	0	0.00195	0.01741	148	•
Stretching 4 %				Stretching 5 %			
Δx_{Min}	Δx_{Max}	NCV	Symbol	Δx_{Min}	Δx_{Max}	NCV	Symbol
0.03125	0.05203	26	$\overline{}$	0.03125	0.05893	26	
0.01563	0.03703	44	A	0.01563	0.04146	40	∇
0.00781	0.02850	66	\bigcirc	0.00781	0.03377	60	•
0.00391	0.02468	94	lacktriangle	0.00391	0.03032	84	\odot
0.00195	0.02222	124	•	0.00195	0.02722	108	•
UPW 1st-order upwind				SP2	2nd-order symmetric		
DRP4	4th-order DRP			DRP6	6th-order DRP		
SP6	J			MLS3	6th-order MLS		
WENO3				WENO5	5th-order WENO		
WENO7	7th-order WENO			MM	Minmod		
SB	Superbee			VL	Van Leer		

2.4.1 Dispersion error results: Eigenbase

In Figure 2.4 we have included the recovered eigenvalue, using the expression in Eq.(2.32) and the concept of basis rotation, for several discrete schemes. In order to avoid a huge amount of figures, we have only shown the results of a reduced number of schemes. We have selected the most representative ones, being a mixture of low and high-order schemes as well as linear and non-linear ones. The first thing that can be noticed when non-dimensionalizing via the maximum mesh size is the fact that there are two different trends: a graph corresponding to uniform meshes, in discontinuous line, and a plot that corresponds to stretched meshes, a dot-line containing the rest of the simulations. The latter is virtually independent of the minimum mesh size nor the stretching factor and just depends on the discretization scheme. This shows that the deviation of the numerical eigenvalue is only given by the maximum size of the mesh. Consequently, two slightly stretched meshes with different stretching factors and minimum mesh size but with the same maximum mesh size will perform in a very similar way.

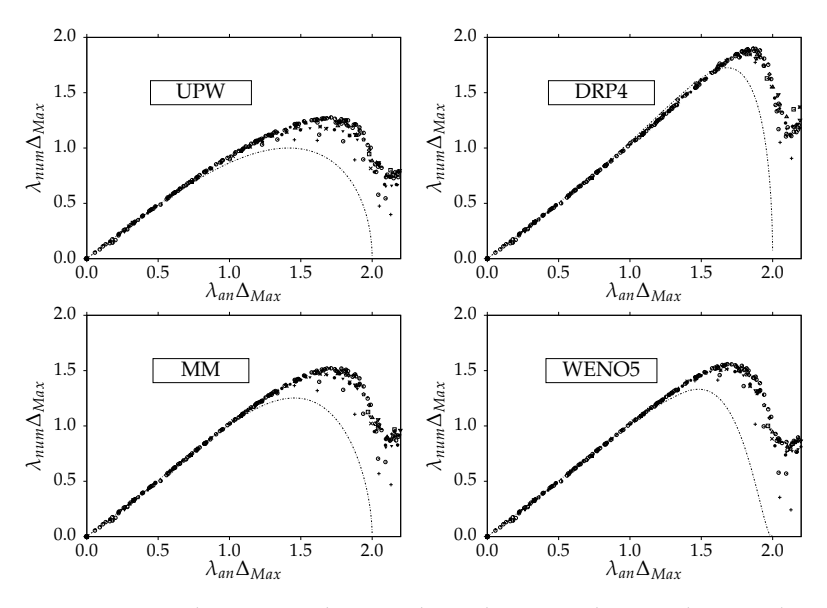


Figure 2.4: Recovered numerical vs analytical eigenvalue made non-dimensional using the maximum mesh size.

Thus, it is possible to have meshes with high mesh ratios, i.e. 5%, that have a good behaviour. However, even if this is possible, it does not mean that it is feasible: in Cartesian stretched meshes, the maximum mesh size is given by the combination of the minimum mesh size, the stretching ratio and the domain length. In a numerical simulation, usually, the domain length is given. Normally, minimum mesh size is given by the minimum hydrodynamic length scale that needs to be captured. If we want to achieve good resolution up to a specific eigenvalue, then the maximum mesh size is not really a free parameter. Consequently, only the minimum mesh size and the stretching factor are the parameters that can be modified. If a very high stretching factor is imposed, for a given length and a maximum size, this implies using an infimum minimal mesh size. On the other hand, imposing a minimum mesh size restricts the stretching to a very small value.

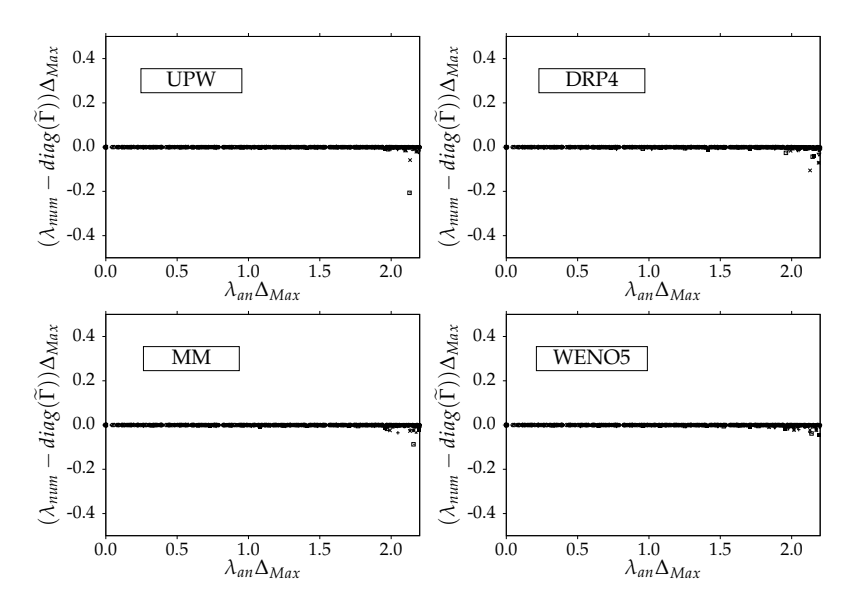


Figure 2.5: Difference between diagonal terms and the root mean square of the row of matrix Γ after 5000 rotations made non-dimensional using the maximum mesh size.

In order to show that the rotation procedure in section 2.3.3 removes aliasing effects, the difference between the diagonal term and the root mean square of the matrix row, $\widetilde{\lambda}_{m}^{C}$ in equation 2.32, is plotted on Figure 2.5.

As it can be seen, the difference between both terms is almost 0, which indicates the matrix $\widetilde{\Gamma}$ is diagonal dominant and, consequently, effectively removes aliasing effects.

As previously commented, the recovered eigenvalue depends also on the phase of the basis. In order to have more information about how modes are projected, the standard deviation of λ is shown in Figure 2.6. Now, differently than the average eigenvalue, the standard deviation seems to depend on both the stretching and minimum mesh size. In other words, the plots do not collapse for stretched meshes.

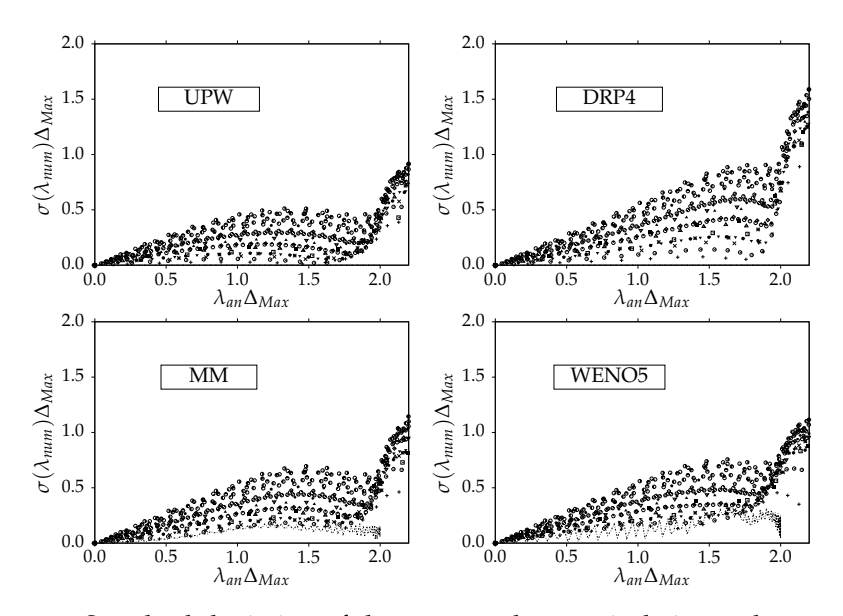


Figure 2.6: Standard deviation of the recovered numerical eigenvalue made non-dimensional using the maximum mesh size.

Distinguishing between linear and non-linear schemes, non-linear ones exhibit a non-null standard deviation for uniform meshes whereas linear schemes have a null standard deviation in the whole spectra in uniform meshes. This means that the distortion of the signal produced by non-linear schemes causes the projection of a single mode onto several ones. Analyzing the difference between high and low-order schemes, the former present higher standard deviation across the whole spectrum than the latter.

This implies that despite high-order schemes behave better than low-order schemes on average, for a given eigenmode and phase high-order schemes behave worse than low-order ones. Taking into account that the phase varies during a simulation, this means that on specific times with favourable phase low-order schemes are preferred over high-order ones. Finally, taking into account the effect of the minimum mesh size, which in reality is translated as a rise in the number of valid modes if the domain is kept constant, it is observed that meshes with small minimum mesh size exhibit a higher standard deviation than meshes with fewer points, i.e. higher minimum mesh size.

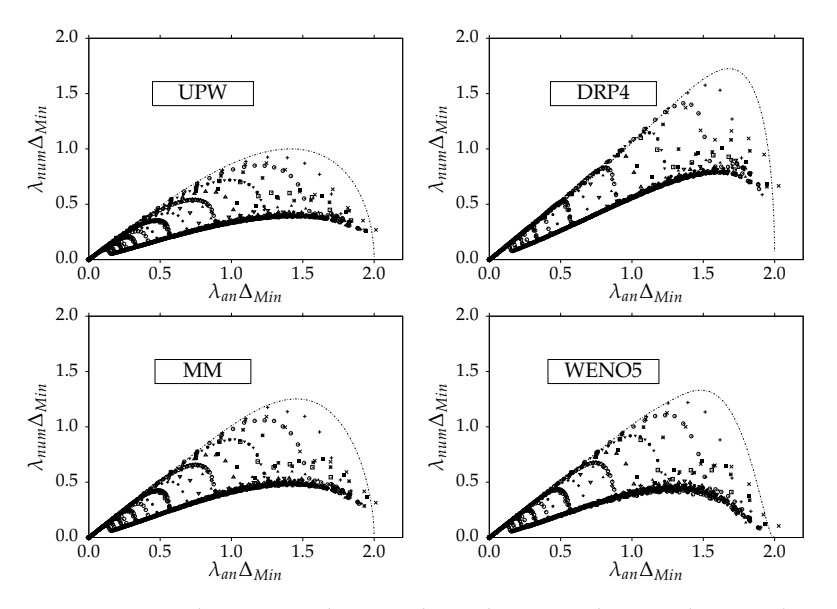


Figure 2.7: Recovered numerical vs analytical eigenvalue made non-dimensional using the minimum mesh size.

Finally, in Figure 2.7 we show the non-dimensionalization of the recovered eigenvalue using the minimum mesh size instead the maximum. This shows that meshes with a larger number of modes, and consequently a smaller minimum mesh size, have more noticeable differences between the maximum resolution of the mesh and its uniform counterpart.

Thus, as the ratio between the maximum and the minimum mesh sizes becomes higher, the differences between a uniform and a stretched meshes, keeping constant the minimum mesh size, becomes wider. Consequently, meshes with higher maximum-to-minimum ratios shown more differences than meshes that resemble more a uniform mesh.

2.4.2 Dispersion error results: Sinusoids

Similarly to the results obtained in the eigenbase, we can analyse them in the sinusoids base. The main reason for doing this is the common analysis works with this base and, if we want a common framework to compare the results, the most straightforward option is to express our results in the sinusoids base. In Figure 2.8 we include the recovered wavenumber versus the analytical one; the non-dimensionalization is performed via the maximum mesh size. This figure is obtained by performing a change of basis of Eq.(2.41) each time the basis of eigenvectors is rotated.

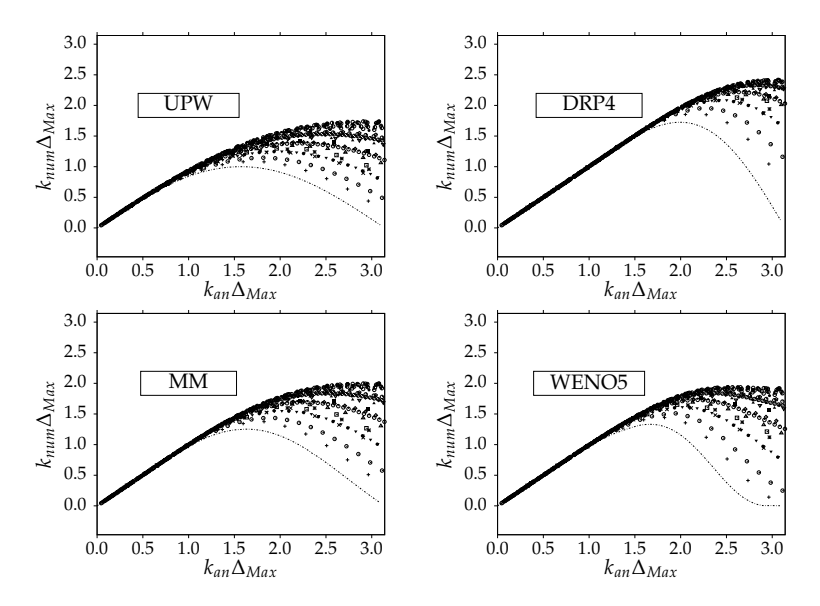


Figure 2.8: Recovered numerical vs analytical wavenumber made non-dimensional using maximum mesh size.

Again in this case, but not as clear as when eigenvectors are used, the stretched meshes tend to the same graph whereas uniform meshes have their own. This reinforce the idea that modes with a higher wavenumber than the corresponding to the maximum mesh size should not be taken into account. In the special case of uniform meshes, the obtained results match with Tam and Webb [1] and Lele [3] in the case of linear discrete operators and with the ADR of Pirozzoli [18] in the case of non-linear schemes. The reason why Figures 2.8 and 2.4 are quite similar is because the eigenvector basis and the sinusoid basis are almost the same up to the eigenvalue equal to $\frac{2}{\Delta x}$, or equivalently up to the wavenumber $\frac{\pi}{\Delta x}$. In other words, the numerical functions that are derived are almost the same. However, for modes with higher associated eigenvalue, this equivalence does not hold.

In Figure 2.9, we include the non-dimensional recovered wavenumber but using the minimum mesh size instead of the maximum one. As can be seen, now the figure does not resemble Figure 2.7 at all. This is because now the used basis in each methodology up to the maximum mode are totally different.

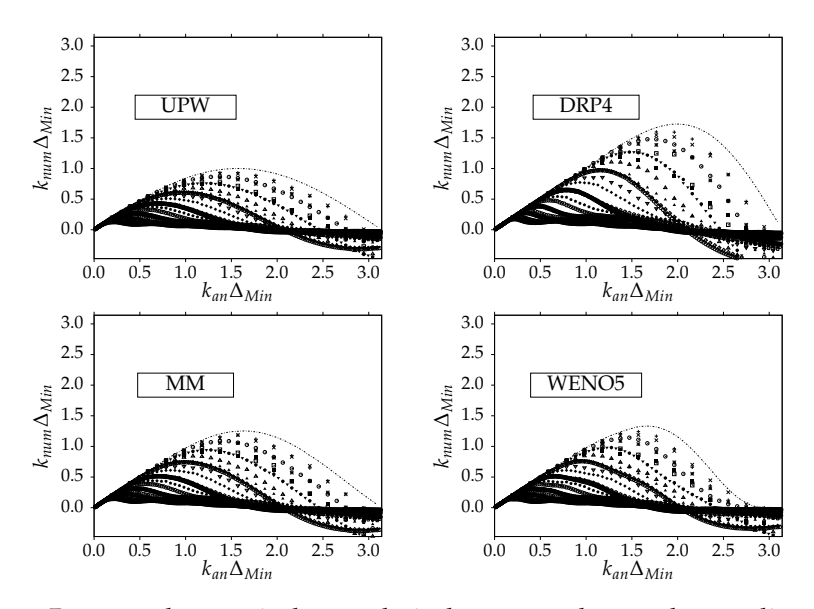


Figure 2.9: Recovered numerical vs analytical wavenumber made non-dimensional using minimum mesh size.

A conclusion extracted from this figure is that in stretched meshes, several frequencies are propagated backwards; in other words, they are reflected. This feature is easily observed when an abrupt change in the mesh size is imposed.

In Figure 2.10 we show the standard deviation of each mode made nondimensional in the same way as has been done with eigenvectors. In this case, however, a clear discontinuity around a specific mode or frequency is not present. This reinforces the idea that the discontinuity can only be observed when studying the orthogonal basis associated to the mesh. When transforming the eigenvector base to the sinus base, low frequencies are composed also of high eigenvectors which appear after the cut-off mode. Therefore, expressing the results in sinusoids space makes them noisier and with a higher standard deviation than when expressing them in the eigenvectors space.

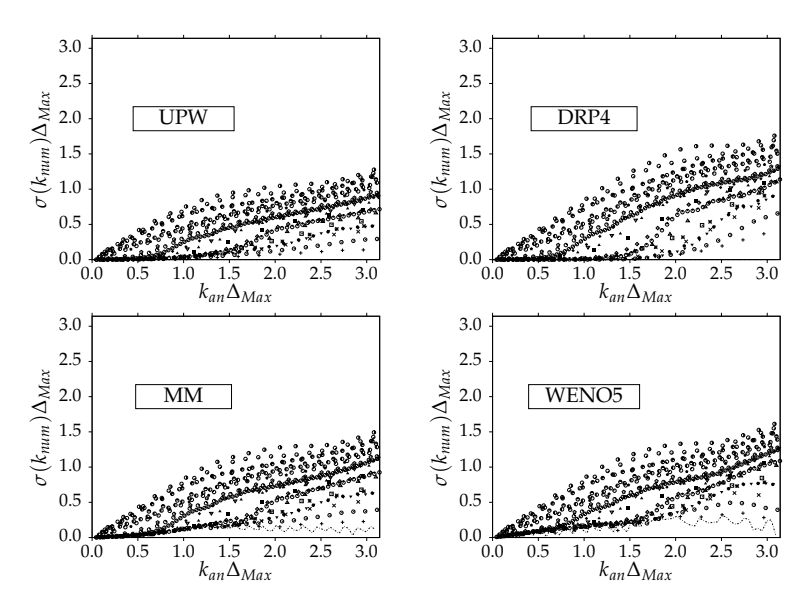


Figure 2.10: Standard deviation of recovered numerical wavenumber vs analytical wavenumber made non-dimensional using maximum mesh size.

So, even though sinusoids basis is the common base to express the results in dispersion phenomena, when stretched meshes are used it seems it is not the most appropriate base to use. Instead, results using eigenvectors seem to be less dependant on the mesh used and even the stretching.

2.5 Effect on the time step

Discretizing in space is just half of the whole procedure when Navier-Stokes equations are solved. The discretization of the transient term requires defining a time-step, the equivalent of mesh size but in the time domain.

The resolution in the temporal scale must be fine enough to capture all the transient features of the simulation. Thus, one can set a very small time-step during the setup process that ensures the simulation will remain stable and will produce reliable results.

Another option will be to compute the required time-step at each iteration. This optimizes the integration process because the used time-step is "optimal"; it could happen that using a constant time-step the temporal resolution is excessive, leading only to an increase of the computational time without affecting the quality of the results. The most common option to compute the time-step is the CFL condition [46]. However, such definition requires the concept of mesh size Δx . In cases where the mesh is uniform and 1D this is not a problem: there is only a Δx in the whole domain. However, if the mesh is no longer uniform but still structured, this is not still a problem. The time-step is then computed as the most restrictive time-step in the whole domain, involving the ratio between the mesh size and the advective speed and choosing the lesser of the whole domain.

Nevertheless, when 2 or 3D domains are considered, the computation of the time-step could become a problem. In cases with grid book, ribbon or pencil types [47] computed time-step usually does not take appropriatelly into account the physics due to the fact CFL condition is just too simple. And finally, when unstructured meshes are used the concept of mesh size is still a bit shady. To solve this, Trias and Lehmkuhl [37] developed a methodology which does not require the concept of mesh size to compute the time-step. Instead, the time-step is constructed using the maximum eigenvalue of the discrete operator.

Tam and Webb [1] or Lele [3] defined the wavenumber, α , of the finite difference as:

$$\alpha = \frac{2}{\Delta x} \sum_{k} a_k \sin(bk), \qquad (2.48)$$

where
$$\frac{a_k}{\Delta x} = c_{n-k}$$
 and $b = \frac{2\pi j}{n}$.

To prove that the wavenumber used by them are the eigenvalues of their differential operator, lets begin with a circular matrix, *A*, which represents a linear discrete operator:

$$A = \begin{pmatrix} c_0 & c_{n-1} & c_{n-2} & \cdots & c_2 & c_1 \\ c_1 & c_0 & c_{n-1} & \cdots & c_3 & c_2 \\ \vdots & c_1 & c_0 & c_{n-1} & \ddots & \vdots \\ c_{n-2} & \ddots & \ddots & c_0 & c_{n-1} \\ c_{n-1} & c_{n-2} & \cdots & c_1 & c_0 \end{pmatrix}.$$
 (2.49)

The eigenvalues of the circulant matrix *A* will be computed as:

$$\lambda_j = c_0 + c_{n-1}\omega_j + c_{n-2}\omega_j^2 + \dots + c_2\omega_j^{n-2} + c_1\omega_j^{n-1}, \tag{2.50}$$

where ω_j is $e^{i\frac{2\pi i}{n}}$. However, as Tam and Lele imposed central stencils, the coefficients of the matrix A are skew-symmetric in order to have non-diffusive schemes. This means $c_j = -c_{n-j}$ and the diagonal term, c_0 , must be null. Replacing:

$$\lambda_{j} = c_{n-1}(\omega_{j} - \omega_{j}^{n-1}) + c_{n-2}(\omega_{j}^{2} - c_{2}\omega_{j}^{n-2}) + \dots = \sum_{k} c_{n-k}(\omega_{j}^{k} - \omega_{j}^{n-k}).$$
(2.51)

This can be further reduced as:

$$\lambda_j = \sum_k c_{n-k} (\omega_j^k - \omega_j^n \omega_j^{-k}) = \sum_k c_{n-k} (\omega_j^k - \omega_j^{-k}), \tag{2.52}$$

which due to the symmetries of the exponential functions reduces to

$$\lambda_j = 2i\sum_k c_{n-k} \sin\left(\frac{2\pi jk}{n}\right). \tag{2.53}$$

Taking into account just the modulus, this expression is equivalent to the one found using the classical approach.

Consequently, the plots that show the relation between the numerical and analytical wavenumber are, indeed, the plots of the numerical eigenvalues of the differential operator. Using this approach, and considering the plots of Tam and Webb [1] and Lele [3], is easy to see that higher-order schemes lead

to a maximum recovered eigenvalue higher than lower-order schemes. If the analysis of Trias and Lehmkuhl [37] is employed here, this implies that high-order schemes require a smaller time-step compared with low-order schemes. Thus, when computing the computational cost, a factor which considers the maximum eigenvalue should be employed. We include in Table 2.2 the ratio of the maximum eigenvalue of several linear discretization schemes normalized with the second-order symmetry preserving scheme and in Table 2.3 the ratio of the maximum eigenvalue of several non-linear schemes normalized with the first-order upwind scheme. On both tables we have included an average value, AVG, of the ratios in stretching meshes; the maximum difference between this average and the eigenvalue using specific stretching is lesser than 2%.

Table 2.2: Non-dimensional maximum eigenvalue normalised respect maximum eigenvalue for second-order symmetry preserving in uniform meshes, linear schemes.

Stretching [%]	SP2	DRP4	DRP6	SP6	MLS3
0	1	1.7254	1.8368	1.586	1.5615
1	1.203	1.8884	1.9638	1.7688	1.7466
2	1.2396	1.8792	1.9466	1.7704	1.7488
3	1.2501	1.856	1.9239	1.7564	1.7369
4	1.2512	1.8364	1.9018	1.7412	1.7205
5	1.2432	1.8223	1.8748	1.7268	1.708
AVG	1.2374	1.8565	1.9222	1.7527	1.7322

As can be seen, the normalized eigenvalues at fixed stretching are always higher in high-order schemes than in low order schemes. This means that, at meshes with the same maximum mesh size, this leads to higher time-steps when using low order schemes due to the fact the values at tables 2.2 and 2.3 are inversely proportional to the time-step.

Table 2.3: Non-dimensional maximum eigenvalue normalised respect maximum eigenvalue for first-order upwind in uniform meshes, non-linear schemes.

Stretching [%]	WENO3	WENO5	WENO7	MM	SB	\overline{VL}
0	1.1667	1.3317	1.4529	1.2526	1.4053	1.3237
1	1.3747	1.52	1.6315	1.4713	1.6272	1.543
2	1.4036	1.5402	1.6432	1.4946	1.6444	1.566
3	1.4072	1.5362	1.6377	1.4966	1.637	1.5611
4	1.4047	1.5296	1.6249	1.4973	1.6344	1.5573
5	1.3889	1.5183	1.6132	1.4736	1.6205	1.5374
AVG	1.3958	1.5289	1.6301	1.4867	1.6327	1.553

2.5.1 Corrected performance

In order to compare the error vs performance of the different numerical schemes used in this thesis, a similar approach to the used by Pirozzoli [18] is employed. In his article, the error was computed as:

$$e_0(\hat{k}_{Max}) = \frac{1}{\hat{k}_{Max}} \max_{0 \le k \le k_{Max}} \left| \hat{k}_{num}(\hat{k}_{an}) - \hat{k}_{an} \right|, \tag{2.54}$$

whereas the computational cost of each scheme was computed as:

$$C \sim \frac{\nu}{\overline{\sigma} \hat{k}_{Max}^{n_D+1}},\tag{2.55}$$

where ν was a measure of the required machine time per node and time-step, $\overline{\sigma}$ a measure of the Courant number and \hat{k} are non-dimensional wavenumbers, being: \hat{k}_{Max} the maximum studied wavenumber, \hat{k}_{an} the analytical one and \hat{k}_{num} the numerical one. In our case, we will modify the definition of some of these parameters slightly. We keep the measure of the maximum relative error as the maximum L2 norm of the difference between the numerical result and the analytic one, but the rest of parameters will be modified. First, our ν will not be the required machine time per node and time-step. We will use the required number of bytes of each scheme, i.e. the number of bytes required to compute the value at the face.

Table 2.4: Arithmetic Intensity for each differential scheme.

SP2	DRP4	DRP6	SP6	MLS3
0.0938	0.1719	0.1875	0.1719	0.1719

UPW	WENO3	WENO5	WENO7	MM	SB	VL
0.0938	0.1667	0.267	0.3816	0.125	0.1148	0.1429

The main reason to not use machine time underlies on the Roofline model [48]. Depending on the arithmetic intensity, the ratio between the number of floating-point operations and required bytes, the processor works under different performance regimes. In table 2.4 we include the different arithmetic intensity values for our implementation of each scheme. This implies that some schemes will access to higher performances than others and, consequently, do a higher number of floating-point operations per second. In consequence, it is possible to have a different number of required number of floating operations but the same clock time. However, actual processor architectures do not reach peak performance on the range of the arithmetic intensities obtained; thus, the simulations are memory-bound [49]. In consequence, the factor that rules the computational cost in this situation is not the time required per simulation but the required number of bytes to compute the value at the face, which is totally independent of the processor. In table 2.5 we include the different number of bytes in double-precision, B, of each scheme.

Table 2.5: Number of bytes (B) for each differential scheme.

SP2	DRP4	DRP6	SP6	MLS3
32	64	80	64	64

UPW	WENO3	WENO5	WENO7	MM	SB	VL
32	168	296	456	112	112	112

The terms $\overline{\sigma}$ and \hat{k}_{Max} we will consider them as a whole. Due to the fact $\overline{\sigma}$ involves a division by Δx and \hat{k}_{Max} involves multiplication by Δx , is easy to see that the product will not depend explicitly on the mesh size but implicitly; the time step is a function of the mesh. We will use the analysis of Trias and Lehmkuhl [37] to deduce the maximum allowable time step.

Using the formulation on their paper, and for pure advection matrices, the maximum allowable time step is proportional to:

$$\Delta t \propto \frac{1}{a||\lambda_{Max}||}. (2.56)$$

Note that we have included the linear advection speed, *a*, as Trias and Lehmkuhl deduction involves using the eigenvalues of the convective speed, which includes implicitly the velocity. In our case, and because we have considered linear wave propagation, the relation between the eigenvalues of the convective operator and the derivative operator is just the product. As has been commented in this work, the maximum eigenvalue when studying linear advection problems on stretched meshes is only a function of the convective scheme and the maximum mesh size. Consequently, the previous equation can be rewritten as:

$$\Delta t = \frac{1}{a||\lambda_{Max}||} \frac{\Delta x_{Max}}{\Delta x_{Max}} \approx \frac{\Delta x_{Max}}{aE},$$
(2.57)

where E is the tabulated coefficient on tables 2.2 and 2.3. In conclusion, the effective computational cost in our work will be computed as:

$$C \sim \frac{B}{a^{\frac{\Delta x_{Max}}{aE}} k_{Max}} = \frac{B \cdot E}{\Delta x_{Max} k_{Max}}.$$
 (2.58)

In figures 2.11 and 2.12 we have included the computational cost vs the relative error of the studied convective schemes for different stretching factors. The upper limit of the wavenumber range belongs to the maximum wavenumber at the coarse mesh. As can be seen, the relative error achieves a minimum at uniform meshes for both linear and non-linear schemes at the cost of an increased computational effort.

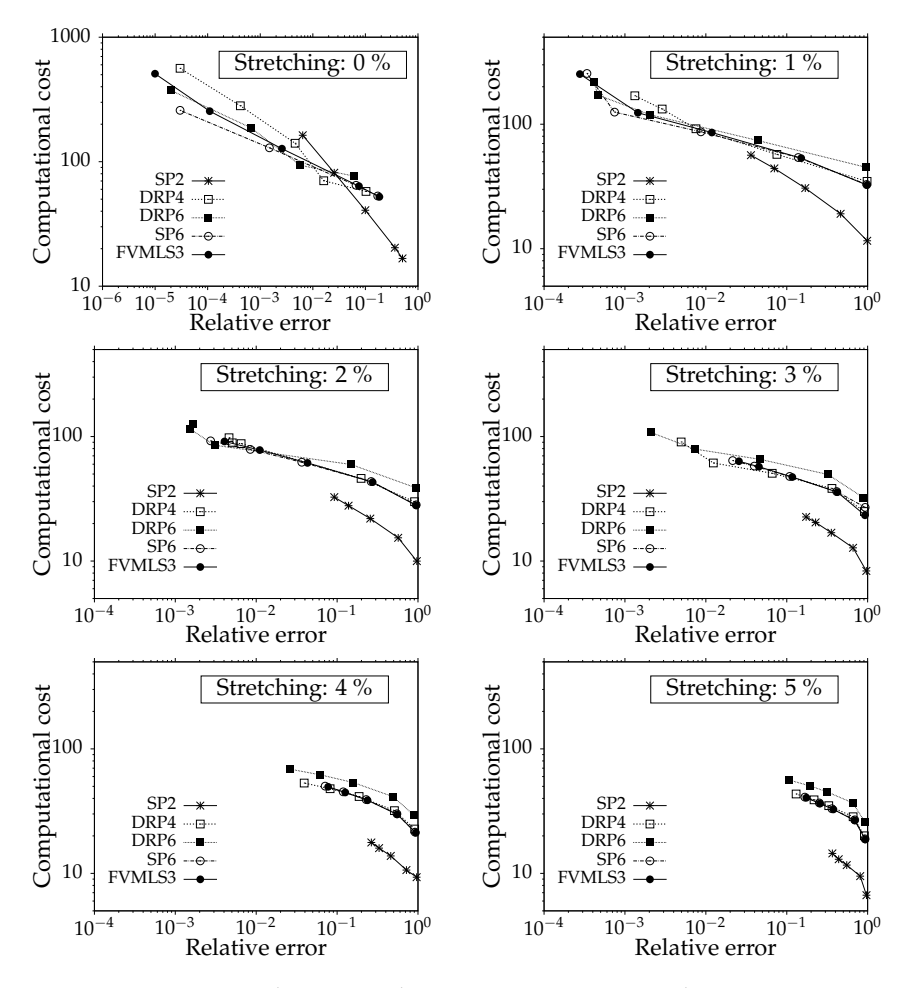


Figure 2.11: Computational cost vs relative error at wavenumber range 0 to 32π for different stretchings and linear convective schemes.

Some non-linear schemes exhibit a break-up in the tendencies; this happens because the error changes its sign, i.e. the numerical wavenumber is higher or lesser than the analytical one depending on the mesh resolution. By just changing from uniform mesh to a mesh stretched 1%, the minimum relative error increases an order of magnitude, from 10^{-5} to higher than 10^{-4} .

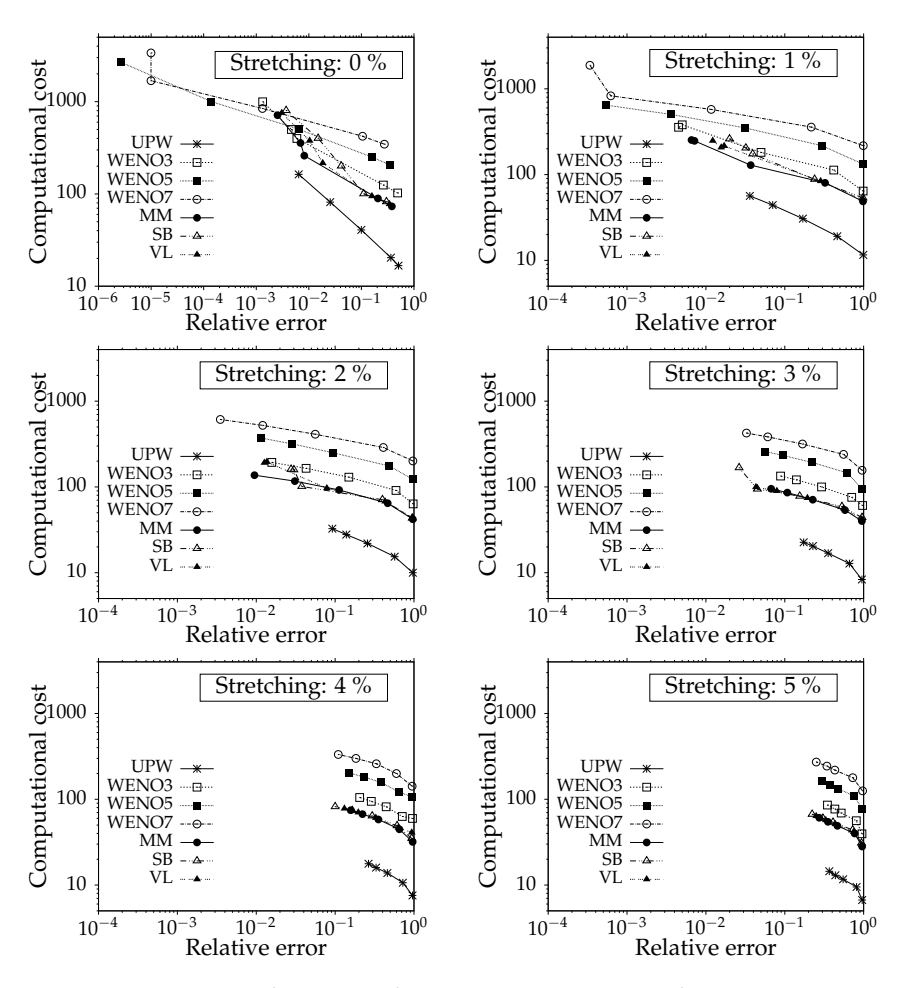


Figure 2.12: Computational cost vs relative error at wavenumber range 0 to 32π for different stretchings and non-linear convective schemes.

Tam [38] studied the deviation point of linear convective schemes and stated that errors higher than 2% were not allowed on long-range propagation. Analysing our results for the studied wavenumber range and used meshes, for stretchings higher than 2% just linear high-order schemes seem to obtain results with an error lesser than the 2% threshold. Regarding specific schemes, both upwind and second-order symmetry preserving schemes have the lowest

computational cost of the whole schemes due to they require few bytes in comparison with the rest. What is interesting is that these schemes can achieve similar values of error than high-order counterparts, using each one different meshes of course, but with approximately a fourth of the required computational effort. A feature which can be analysed from previous figures is the fact that low-order schemes seem to keep their order of convergence, i.e. the slope at each plot is almost the same: doubling the computational effort, reduces the error to a fourth. However, high order schemes become less cost-effective as stretching becomes more important. For example, SP6, MLS3 and DRP6 in less-stretched meshes, each time computational cost is doubled the error is reduced approximately 50 times, in uniform meshes the reduction is equal to 2^6 , where 6 is the formal order of accuracy of the scheme. However, in highly stretched meshes, each time the cost is doubled, the error is reduced less: about 25 times. Consequently, the formal order of accuracy is reduced. Nevertheless, they are still more cost-effective than low-order schemes, but less than if uniform meshes are used.

On the family of non-linear schemes, WENO schemes have the highest computational cost due to they are the ones with the highest number of bytes, as shown in Table 2.5. As noted by Pirozzoli [18], when strict tolerances are imposed, WENO schemes become the only possible option as they achieve very low relative errors due to a lesser slope in comparison with classical TVD schemes. However, when stretched meshes are used, starting at 2%, WENO schemes do not reduce the relative error more than TVD schemes; both have similar error values but a difference of an order of magnitude in their computational cost. And additionally, when stretched meshes are used, both TVD and WENO schemes, independently of the employed order, seem to have almost identical convergence order: when the computational effort is doubled, the error is reduced a little bit more than one order of magnitude.

Looking Figures 2.11 and 2.12, and with some extrapolation onto finer meshes, i.e. lesser errors higher computational costs, it seems that low-order schemes have always lesser computational costs for a fixed error. However, this is a very tricky statement. First, the obtained error range for stretched meshes is quite small. Even high-order schemes are not able to reach an error lesser than 10^{-4} on slightly stretched meshes; this is more noticeable on highly stretched ones, where the error is in the range of 1-10%. Consequently, extrapolating could be misleading.

And second, the procedure used in this work does not take into account the simulation as a whole but just one term of the full equation. Pre-processing times, the size of the mesh that needs to be stored when multiple dimensions are simulated instead of a single one, the effect that other terms of the full equation... are factors that should be taken into account if such statement were claimed. Nevertheless, this is out of the reach of this study.

2.6 Conclusions

In this chapter, an alternative methodology to compute dispersion errors which is neither restricted to uniform meshes nor linear schemes has been developed. This methodology arises from questioning how dispersion should be computed in non-uniform domains to avoid using Fourier Transform. We thought it would be useful to answer that question as the majority of used meshes in CFD or CAA are not uniform. The key that opened the door to use non-uniform meshes was to change the kernel of the method, as it lies on analysing the spectrum of discrete operators and, consequently, does not require Fourier Transform. Nevertheless, there is a strong link between the usual approach to analyse dispersion and the herepresented method: both use the eigenvectors of the discrete Laplacian. The Discrete Fourier Transform used in the classical method can be seen as the projection of discrete functions on uniform meshes onto the eigenvectors of discrete Laplacian. Consequently, when uniform meshes are used, both methodologies converge onto the same results.

Regarding the experiments selected, we have chosen configurations able to produce results which can be compared with previous studies. This means that, even the method is not restricted to one-dimensional Cartesian structured meshes, just this kind have been used, even though fully unstructured three-dimensional meshes could have been used. The first reason to use one-dimensional meshes is that if unstructured meshes were employed, meaning at least two-dimensional meshes, the results will not be understandable. For each eigenvalue, two different values will be recovered, three in three-dimensional meshes. However, and as pointed by Lele [3] or Nogueira [43], the polar representation of the recovered wavenumber shows that for a given wavenumber, depending on its components, it has different dispersion errors.

70 §2.6 Conclusions

If eigenvalues are used, the components are not a free parameter, and thus the result will only show several components but not the total number of combinations. Additionally, using an unstructured mesh will not provide any insight in understanding numerical dispersion in a general way as the results will solely represent the used mesh. Finally, the usage of periodic boundary conditions is not mandatory in the presented method. However, they have been used in order to compare with results employing Fourier Transform, which requires periodic domains.

During the development of the procedure, we have also taken into account the analysis of Fauconnier and Dick [19]. As both non-linear schemes and non-uniform meshes distort the signal when approximating the derivative, the numerical wavenumber depends on both the analytical one and the phase of the input signal. Thus, the phase should be considered as a study parameter to compute dispersion characteristics. However, in non-uniform meshes the phase lacks of sense: the spectral resolution is not the same in the whole domain. The extrapolation to their analysis to non-uniform meshes uses rotation matrices. More precisely, instead of changing the phase of a couple of discrete sinusoids, two consecutive orthogonal eigenvectors are selected and rotated a random angle; in uniform meshes this is exactly Fauconnier and Dick method.

Another feature of conflict which wanted to be studied was the computation of time-step, which affect the whole computational cost of the simulation. As was studied by Trias and Lehmkhul [37], the maximum allowed time step is linked with the maximum eigenvalue of the discrete operator. The dispersion plots of Tam and Webb [1] and Lele [3] are the eigenvalues of their discrete convective operator. In their plots, it is easy to see that high-order schemes have a higher maximum than low-order ones; consequently, they require a lesser time-step. This effect is also included in the herepresented results regarding the computational cost of discrete schemes.

Regarding the results, and as previously commented, when uniform meshes are used the results match the ones obtained by authors using the classical approach. Results of linear convective operators match the obtained by both Tam and Webb [1] and Lele [3], whereas the ADR of Pirozzoli [18] matches the results obtained in this thesis when studying non-linear schemes. On the other hand, when using Cartesian stretched meshes a new plot has been observed.

More precisely, making the numerical eigenvalue non-dimensional via the maximum mesh size, the recovered plot does not depend on the stretching factor nor the number of mesh nodes but just on the discrete scheme. There is, of course, a transition between the uniform plot towards the stretched plot, but even slightly stretched meshes, in the range of 1% of stretch, collapse onto the same plot. What should be noticed is the fact that low-order schemes seem to transition slower than high-order schemes. Nevertheless, this is also expected as in high-order stencils a higher number of nodes is required, implying a higher ratio between the maximum and minimum size of the stencil. Studying dispersion in the eigenvector space allows to explicitly see a cut-off mode for stretched meshes which solely depends on the maximum mesh size. After this mode, each frequency is aliased by a larger number of modes. This translates into a noticeable increase of variance of each row eigenmode. However, when plotting the same results but using sinusoid basis instead of eigenvectors, the results previously commented were not observed: the plots do not collapse onto a single one for stretched meshes and the cut-off frequency is not observed.

The results analysing the computational cost show that low-order schemes, UPW and SP2, seem to keep their formal order of convergence. However, high-order schemes, independently if they are linear or not, become less cost-effective in stretched meshes than in structured ones as their formal order of accuracy is reduced. An interesting conclusion for non-linear schemes is that WENO schemes, independently of the order, are not a good option for stretched meshes with stretchings higher than 2%. The numerical error for both WENO and TVD schemes is appropriately the same, whereas the computational cost is always higher for WENO schemes. It has also observed that for stretchings higher than 3% the numerical wavenumbers have associated errors higher than 1% in the studied range, which is the approximate relative error at which Tam [38] considers there is the deviation point.

Regarding the method's applicability, the herepresented procedure could help to develop or select the more appropriate differential schemes when several meshes geometries are taken into account. We hope that this methodology could be applied to the design of meshing techniques leading to reduction of dispersion errors as it could quantify the associated dispersion error to the mesh used.

References

[1] Christopher K W Tam and Jay C Webb. Dispersion-relation-preserving finite difference schemes for Computational acoustics. *Journal of Computational Physics*, pages 262–281, 1993.

- [2] Christophe Bogey and Christophe Bailly. A family of low dispersive and low dissipative explicit schemes for flow and noise computations. *Journal of Computational Physics*, 194(1):194–214, 2004.
- [3] Sanjiva K. Lele. Compact finite difference schemes with spectral-like resolution. *Journal of Computational Physics*, 1992.
- [4] F Xavier Trias, Oriol Lehmkuhl, Assensi Oliva, Carlos David Pérez-Segarra, and RWCP Verstappen. Symmetry-preserving discretization of navier–stokes equations on collocated unstructured grids. *Journal of Computational Physics*, 258:246–267, 2014.
- [5] RWCP Verstappen and AEP Veldman. Symmetry-preserving discretization of turbulent flow. *Journal of Computational Physics*, 187(1):343–368, 2003.
- [6] W Rozema, JC Kok, RWCP Verstappen, and AEP Veldman. A symmetry-preserving discretisation and regularisation model for compressible flow with application to turbulent channel flow. *Journal of Turbulence*, 15(6):386–410, 2014.
- [7] R Charles Swanson and Eli Turkel. On central-difference and upwind schemes. *Journal of Computational Physics*, 101(2):292–306, 1992.
- [8] Richard Courant, Eugene Isaacson, and Mina Rees. On the solution of nonlinear hyperbolic differential equations by finite differences. *Communications on Pure and Applied Mathematics*, 5(3):243–255, 1952.
- [9] Ami Harten. High resolution schemes for hyperbolic conservation laws. *Journal of Computational Physics*, 49(3):357–393, 1983.
- [10] Sergei Konstantinovich Godunov. A difference method for numerical calculation of discontinuous solutions of the equations of hydrodynamics. *Matematicheskii Sbornik*, 89(3):271–306, 1959.

[11] Bram Van Leer. Towards the ultimate conservative difference scheme. ii. monotonicity and conservation combined in a second-order scheme. *Journal of Computational Physics*, 14(4):361–370, 1974.

- [12] Ami Harten, Bjorn Engquist, Stanley Osher, and Sukumar R Chakravarthy. Uniformly high order accurate essentially non-oscillatory schemes, III. In M Yousuff Hussaini, Bram van Leer, and John Van Rosendale, editors, *Upwind and high-resolution schemes*, pages 218–290. Springer, 1987.
- [13] Xu-Dong Liu, Stanley Osher, and Tony Chan. Weighted essentially non-oscillatory schemes. *Journal of Computational Physics*, 115(1):200–212, 1994.
- [14] Zhen-Sheng Sun, Yu-Xin Ren, Cedric Larricq, Shi-Ying Zhang, and Yue-Cheng Yang. A class of finite difference schemes with low dispersion and controllable dissipation for dns of compressible turbulence. *Journal of Computational Physics*, 230(12):4616–4635, 2011.
- [15] Qiu-Ju Wang, Yu-Xin Ren, Zhen-Sheng Sun, and Yu-Tao Sun. Low dispersion finite volume scheme based on reconstruction with minimized dispersion and controllable dissipation. *Science China Physics, Mechanics and Astronomy*, 56(2):423–431, 2013.
- [16] Felix S Schranner, J Andrzej Domaradzki, Stefan Hickel, and Nikolaus A Adams. Assessing the numerical dissipation rate and viscosity in numerical simulations of fluid flows. *Computers & Fluids*, 114:84–97, 2015.
- [17] EMJ Komen, EMA Frederix, THJ Coppen, V D'alessandro, and JGM Kuerten. Analysis of the numerical dissipation rate of different runge–kutta and velocity interpolation methods in an unstructured collocated finite volume method in openfoam®. *Computer Physics Communications*, page 107145, 2020.
- [18] Sergio Pirozzoli. On the spectral properties of shock-capturing schemes. *Journal of Computational Physics*, 219(2):489–497, 2006.
- [19] Dieter Fauconnier and Erik Dick. On the spectral and conservation properties of nonlinear discretization operators. *Journal of Computational Physics*, 230(12):4488–4518, 2011.

[20] Guoyan Zhao, Mingbo Sun, Antonio Memmolo, and Sergio Pirozzoli. A general framework for the evaluation of shock-capturing schemes. *Journal of Computational Physics*, 376:924–936, 2019.

- [21] Christophe Bogey. Grid sensitivity of flow field and noise of high-reynolds-number jets computed by large-eddy simulation. *International Journal of Aeroacoustics*, 17(4-5):399–424, may 2018.
- [22] Michael L. Shur, Philippe R. Spalart, and Michael Kh. Strelets. Noise prediction for increasingly complex jets. part i: Methods and tests. *International Journal of Aeroacoustics*, 4(3):213–245, jul 2005.
- [23] Michael L Shur, Philippe R Spalart, and Michael K Strelets. Jet noise computation based on enhanced DES formulations accelerating the RANS-to-LES transition in free shear layers. *International Journal of Aeroacoustics*, 15(6-7):595–613, jul 2016.
- [24] Lin Fu. A very-high-order teno scheme for all-speed gas dynamics and turbulence. *Computer Physics Communications*, 244:117–131, 2019.
- [25] Roland Ewert and Wolfgang Schröder. Acoustic perturbation equations based on flow decomposition via source filtering. *Journal of Computational Physics*, 188(2):365–398, 2003.
- [26] Jung H Seo and Young J Moon. Linearized perturbed compressible equations for low mach number aeroacoustics. *Journal of Computational Physics*, 218(2):702–719, 2006.
- [27] M. Fuchs, C. Mockett, M. Shur, M. Strelets, and J. C. Kok. Single-stream round jet at m = 0.9. In *Notes on Numerical Fluid Mechanics and Multidisciplinary Design*, pages 125–137. Springer International Publishing, jul 2017.
- [28] M Fuchs, C Mockett, M Shur, M Strelets, and JC Kok. Single-stream round jet at m= 0.9. In *Go4Hybrid: Grey Area Mitigation for Hybrid RANS-LES Methods*, pages 125–137. Springer, 2018.
- [29] James Tyacke, Iftekhar Naqavi, Zhong-Nan Wang, Paul Tucker, and Peer Boehning. Predictive large eddy simulation for jet aeroacoustics–current

- approach and industrial application. *Journal of Turbomachinery*, 139(8), mar 2017.
- [30] Antony Jameson. Formulation of kinetic energy preserving conservative schemes for gas dynamics and direct numerical simulation of one-dimensional viscous compressible flow in a shock tube using entropy and kinetic energy preserving schemes. *Journal of Scientific Computing*, 34(2):188–208, 2008.
- [31] Fenghua Zheng and Zhizhang Chen. Numerical dispersion analysis of the unconditionally stable 3-d adi-fdtd method. *IEEE Transactions on Microwave Theory and Techniques*, 49(5):1006–1009, 2001.
- [32] Alexander Blinne, David Schinkel, Stephan Kuschel, Nina Elkina, Sergey G Rykovanov, and Matt Zepf. A systematic approach to numerical dispersion in maxwell solvers. *Computer Physics Communications*, 224:273–281, 2018.
- [33] Daniel J Bodony and Sanjiva K Lele. Current status of jet noise predictions using large-eddy simulation. *AIAA Journal*, 46(2):364–380, 2008.
- [34] Man Mohan Rai and Parviz Moin. Direct numerical simulation of transition and turbulence in a spatially evolving boundary layer. *Journal of Computational Physics*, 109(2):169–192, 1993.
- [35] R Vichnevetsky. Propagation through numerical mesh refinement for hyperbolic equations. *Mathematics and Computers in Simulation*, 23(4):344–353, 1981.
- [36] Lloyd N Trefethen. Group velocity in finite difference schemes. *SIAM review*, 24(2):113–136, 1982.
- [37] FX Trias and O Lehmkuhl. A self-adaptive strategy for the time integration of navier-stokes equations. *Numerical Heat Transfer, Part B: Fundamentals*, 60(2):116–134, 2011.
- [38] Christopher KW Tam. *Computational Aeroacoustics: a wave number approach*, volume 33. Cambridge University Press, 2012.

[39] Larisa Beilina, Evgenii Karchevskii, and Mikhail Karchevskii. *Numerical Linear Algebra: Theory and Applications*. Springer, 2017.

- [40] D. I. Shuman, S. K. Narang, P. Frossard, A. Ortega, and P. Vandergheynst. The emerging field of signal processing on graphs: Extending high-dimensional data analysis to networks and other irregular domains. *IEEE Signal Processing Magazine*, 30(3):83–98, May 2013.
- [41] Pavel B Bochev and James M Hyman. *Principles of mimetic discretizations of differential operators*. Springer, 2006.
- [42] Sofiane Khelladi, Xesús Nogueira, Farid Bakir, and Ignasi Colominas. Toward a higher order unsteady finite volume solver based on reproducing kernel methods. *Computer Methods in Applied Mechanics and Engineering*, 200(29-32):2348–2362, 2011.
- [43] X Nogueira. *Moving least squares and high-order finite volume methods for the numerical simulation of compressible flows*. PhD thesis, Universidade da Coruna, 2009.
- [44] Chi-Wang Shu. Essentially non-oscillatory and weighted essentially non-oscillatory schemes for hyperbolic conservation laws. In *Advanced numerical approximation of nonlinear hyperbolic equations*, pages 325–432. Springer, 1998.
- [45] Mark Galassi, Jim Davies, James Theiler, Brian Gough, Gerard Jungman, Patrick Alken, Michael Booth, and Fabrice Rossi. Gnu scientific library. *Reference Manual edition*, 1, 2007.
- [46] Richard Courant, Kurt Friedrichs, and Hans Lewy. Über die partiellen differenzengleichungen der mathematischen physik. *Mathematische annalen*, 100(1):32–74, 1928.
- [47] Mikhail L. Shur, Philippe R. Spalart, Mikhail Kh. Strelets, and Andrey K. Travin. An enhanced version of DES with rapid transition from RANS to LES in separated flows. *Flow, Turbulence and Combustion volume*, 95(4):709–737, jun 2015.

[48] Samuel Williams, Andrew Waterman, and David Patterson. Roofline: an insightful visual performance model for multicore architectures. *Communications of the ACM*, 52(4):65–76, 2009.

[49] Jack Dongarra, Michael A Heroux, and Piotr Luszczek. High-performance conjugate-gradient benchmark: A new metric for ranking high-performance computing systems. *The International Journal of High Performance Computing Applications*, 30(1):3–10, 2016.

The effect of numerical scheme and turbulence model on subsonic round jet spectra

Main contents of this chapter has been published in:

A. P. Duben, J. Ruano, A. V. Gorobets, J. Rigola and F.X Trias. Evaluation of enhanced gray area mitigation approaches based on jet aeroacoustics. *AIAA journal*, 61(2), 612-625, 2023.

Abstract. This chapter presents the investigation of the requirements for accurate scale-resolving simulation of aerodynamics and aeroacoustics of the subsonic turbulent round jet. To avoid the non-physical delay in the transition from Reynolds-averaged Navier–Stokes (RANS) to Large Eddy Simulation (LES) in a Detached-Eddy Simulation (DES), recently developed dynamic adapting subgrid length scales ($\tilde{\Delta}_{\omega}$, Δ_{SLA} and Δ_{lsq}) and subgrid LES models (σ and S3QR) are used as a Gray Area Mitigation (GAM) technique. The case selected is the aforementioned subsonic turbulent round jet, using a set of three refining unstructured meshes to analyze the problem's convergence. Two different scale-resolving numerical algorithms were used to analyse the effect of the numerical scheme's order of accuracy: OpenFOAM and NOISEtte.

OpenFOAM is a low-order accuracy open-source numerical code, whereas NOISEtte is an in-house code offering high-order accuracy schemes. The obtained results show how the selection of both the numerical scheme and the combination of subgrid length scale and LES model affect the quality of both jet aerodynamics and acoustics.

3.1 Introduction

Computational AeroAcoustics (CAA) requires a very accurate numerical solution in the near-field flow region to simulate the aerodynamic noise generation mechanisms adequately. If turbulence is not well-resolved, acoustics will not be either. In this context, it is important to know how the numerical discretization of differential operators and partial turbulence modeling in a scale-resolving numerical algorithm affect the quality of the results. As acoustics is very sensitive to the accuracy of simulation of the flow fields that reproduce noise sources, high-accuracy numerical schemes are in great demand. This is especially important for simulating turbulent jet noise. Bogey [1] and Shur et al. [2,3] used high-order schemes on structured meshes, which can be difficult to deal with in the case of complex geometries in industrial problems. On the other hand, high-order schemes on unstructured meshes are computationally much more expensive. To reduce resource intensity, secondorder low-dissipation schemes can be used in combination with meshes that satisfy extra quality requirements, such as structured-like hexahedral zones in the jet plume region, flow-aligned mesh lines, and smooth changes in mesh resolution. Tyacke et al. [4] and Fuchs et al. [5] used second-order schemes when simulating a jet. Of course, second-order finite-volume methods can be used with fully unstructured meshes, but with much higher resolution, as in [6], hoping that this will still be less computationally expensive than high-order methods. The use of higher-accuracy second-order schemes with extended numerical stencils can improve the fidelity of results without significantly increasing computational costs. By higher accuracy, we mean lower values of the error (relative to the exact solution in model problems [7]) compared to "standard" second-order schemes (see [8,9]). Bres et al. [10,11] and Duben and Kozubskaya [9] use algorithms based on such schemes to capture both jet plume aerodynamics and far-field noise.

Another feature that affects the quality of the results, especially the acoustics, is how turbulence is modeled. Hybrid RANS-LES methods (HRLM) aim to achieve an optimal balance between accuracy and computational cost. They allow simulating flows at high Reynolds numbers without requiring excessively fine meshes, especially in the near-wall region. Among such methods, the detached eddy simulation (DES) family is one of the most widely used and extensively validated non-zonal approaches that are actively developing nowadays. Recent investigations are focused on solving the so-called gray-area problem in shear-layer flows, which is the delay of RANS-to-LES transition from steady RANS to the mesh-resolved turbulence operating in the LES regime. The usual methodology for the gray-area mitigation (GAM) follows from the definition of the subgrid eddy viscosity:

$$\nu_t = \left(C_{\text{LES}}\Delta_{\text{SGS}}\right)^2 \cdot \mathcal{D}_{\text{LES}}.\tag{3.1}$$

Here Δ_{SGS} is the subgrid length scale (SGS), \mathcal{D}_{LES} is the LES model differential operator (that is typically derived from the resolved velocity gradient tensor, $G = \partial u_i / \partial x_i$), C_{LES} is the LES constant, which is usually calibrated on the decay of homogeneous isotropic turbulence. Thus, the RANS-to-LES transition can be triggered by decreasing ν_t , which, in turn, is achieved by reducing Δ_{SGS} or \mathcal{D}_{LES} . For this, special dynamic subgrid length scales, which are sensitive to the local flow characteristics, were developed, such as Δ_{ω} [12,13], $\tilde{\Delta}_{\omega}$ [14], $\Delta_{\rm SLA}$ [15] and Δ_{lsq} [16]. All of them, to some extent, contribute to the GAM. However, they differ in their behavior in the region of developed turbulent flow. LES models sensitive to two-dimensional flow patterns, such as σ , WALE [17], or S3PQR [18], can replace the Smagorinsky model used in the original DES formulation [19] and its modifications DDES [20] and IDDES [21]. The abovementioned SGS and LES models can be applied together [14]. In doing so, the following are essential questions requiring well-justified answers. While GAM strategies improve the performance of a scale-resolving algorithm in the initial part of the shear layers by inducing a rapid transition to resolved turbulence, do they perform well in the perturbed flow region? And if not, to what extent? How do GAM strategies affect acoustics? How do they behave in terms of mesh convergence?

The present study addresses these questions, which are especially relevant for aeroacoustics problems. Far-field noise is very sensitive to dissipation coming from the numerical method and turbulence model, and a lack of 82 §3.1 Introduction

viscosity can lead to the generation of spurious noise caused by instabilities in the solution. Various GAM approaches are being investigated and evaluated in terms of accuracy for both aerodynamics and aeroacoustics. The present work continues the study [22], where the evaluation was mostly focused on the aerodynamics of incompressible (or low-Mach) shear-layer flows. Here we present the results of simulating an immersed subsonic turbulent air jet at a Mach number M=0.9. In this case, compressibility plays an essential role, of course. The simulations are performed on a set of refining meshes to evaluate mesh convergence.

The accuracy of predicting the turbulent jet far-field noise is largely determined by the accuracy of simulating the shear layer evolution. Most of the computations carried out by many researchers assume a quasi-stationary simulation of the flow upstream of the nozzle exit (see, for instance, [2,4,9,11]). This simplification is used because the accurate reproduction of the thin turbulent boundary layer inside the nozzle is very computationally demanding. Resolving near-wall turbulence inside the nozzle, even in simplified configurations (e.g., reduced Reynolds number), requires very fine computational meshes consisting of hundreds of millions of nodes [1,6,23]. Thus, when there is no resolved turbulence inside the nozzle, rapid transition in the initial part of the shear layer is crucial. It can be accelerated to some extent by providing fine enough mesh near the nozzle edge, as, in [11,24], which again leads to much higher computational costs. But if we want to preserve low resource intensity, the scale-resolving approach and its GAM properties play a determining role. For example, as demonstrated in Figure 3.3, where the solutions on the same mesh, with and without delayed shear layer RANS-to-LES transition, are shown. Thus, the ability of particular scale-resolving approaches with the GAM properties to adequately predict jet noise in the far-field requires careful research, which is the focus of the present study. Additionally, we consider the influence of the accuracy provided by the numerical scheme on the results obtained. It is done by using the two 2nd order finite-volume numerical algorithms: the higher-accuracy one realized in the code NOISEtte and the lower-accuracy one from the OpenFOAM code.

The chapter is organized as follows. The case formulation and computational setup are presented in section 3.2. The numerical algorithms in use are described in section 3.3. Then, the results of all the computations with their evaluation are demonstrated in section 3.4.

3.2 Case Formulation and Computational Meshes

An immersed jet exiting from a conical nozzle at $M_{\rm jet}=0.9$ and ${\rm Re}_D=1.1\cdot 10^6$ based on the jet diameter D and the jet exit velocity $U_{\rm jet}$ is considered. The present jet case is based on the experiments conducted by Viswanathan [25], aimed at investigating its aeroacoustic. The reference far-field data, OASPL and $1/3^{\rm rd}$ spectra, are taken from there. The jet plume aerodynamics and turbulence characteristics are evaluated using the experimental data of similar jets [26–30]. The computational domain, mesh, and boundary conditions are obtained from the study carried out by Shur et al. [31]. This case was already used in several works: Shur et al. [3], Duben&Kozubskaya [9], and in Pont-Vílchez et al. [22].

The most common and widely used approach to jet simulation is when the internal part of the nozzle is present in the computational domain with the total pressure, temperature, and velocity direction specified at the inlet. This approach, with the nozzle considered, has been used either with or without resolved turbulence upstream of the nozzle exit [4,6,11,32].

In the absence of resolved turbulence inside the nozzle, some incorrectness in simulating the initial region of the shear layer is introduced due to the lack of turbulent content. In this situation, even local mesh refinement near the nozzle edge does not help [11]. But the proper resolution of turbulence inside the nozzle in many cases requires too much computational effort for practical use.

For this reason, turbulence modeling approaches that can provide reasonably accurate solution while avoiding scale-resolved simulation of the turbulent boundary layer inside the nozzle are of high value. In such approaches, the GAM property plays a crucial role, since it is responsible for the numerical RANS to LES transition. Therefore, in the present work, we study GAM in such conditions, when no resolved turbulence is present at the nozzle exit.

In order to further reduce computational cost, we use the two-stage approach, as in many other jet simulations using various numerical algorithms [3,5,9,14,22]. At the first stage, the entire configuration with both the nozzle and the jet plume is simulated using RANS. This first-stage steady-state solution for the present simulations was provided by M. Shur and M. Strelets from the Peter the Great St. Petersburg Polytechnic University.

At the second stage, the jet-plume region is simulated separately using a scaleresolving method with the obtained stationary RANS solution imposed on the boundary surface at the nozzle exit. This allows us to save the computational cost of maintaining a predominantly stationary zone inside the computational domain during the scale-resolving simulation. If the GAM works fine in this simplified configuration, we can expect that it will also work in the entire setup with the nozzle (the opposite is not so obvious).

A set of hexahedral refining meshes, labeled *Grid 1*, *Grid 2*, and *Grid 3*, is used for the simulations. These three meshes are directly inherited from Shur et al. [31]. Table 3.1 summarises the main parameters of these meshes: the total number of nodes, N_n ; the number of nodes in the azimuthal direction, N_{φ} ; the mesh step sizes Δ_x , Δ_r , Δ_{φ} relative to the nozzle diameter, D, in the streamwise, radial and azimuthal directions, respectively.

Table 3.1: Meshes parameters

Parameter	Grid 1	Grid 2	Grid 3
N_n	1.52M	4.13M	8.87M
N_{arphi}	64	80	160
Δ_x/D at the nozzle exit	0.011	0.008	0.008
$\min (\Delta_r/D)$ in the shear layer	0.003	0.0025	0.0025
$r\Delta_{\varphi}/D$ in the shear layer	0.05	0.04	0.02

Additionally, the distributions of the minimum (Δ_{min}) and maximum (Δ_{max}) values of the subgrid length scales along the jet lip line (the streamwise line downstream of the nozzle edge) are presented in Figure 3.1. The nodal values of the Δ_{min} and Δ_{max} are derived from the corresponding heights of the incident elements.

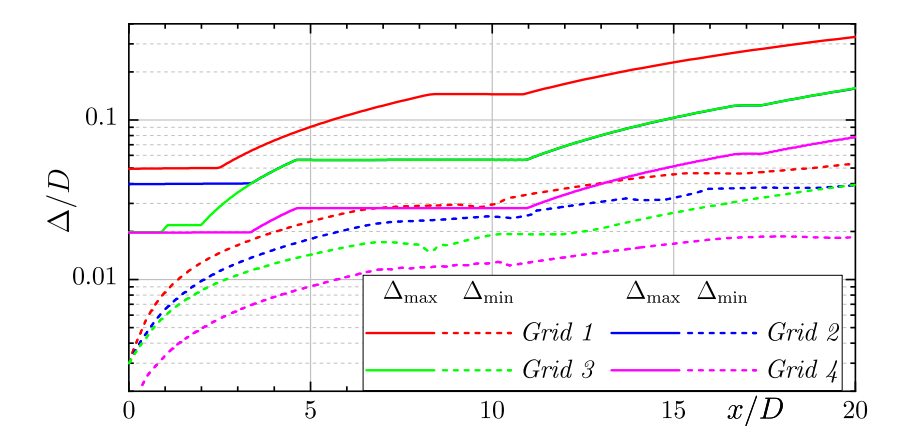


Figure 3.1: Distributions of maximum (Δ_{max}/D , solid lines) and minimum (Δ_{min}/D , dashed lines) mesh sizes along the lip line for the meshes considered

3.3 Mathematical Models and Numerical Methods

All the simulations are carried out using the DDES [20] approach. Note that due to the absence of co-flow, the method operates mostly in the LES regime, so the influence of the external nozzle walls is negligible. The incorporation of alternative LES models is done according to the technique suggested by Mockett et al. [5,14].

In order to evaluate the sensitivity of the eddy viscosity models on the jet simulation results, two scale-resolving algorithms are considered. The use of two codes with significantly different numerical schemes in terms of approximation accuracy allows us to more comprehensively investigate the performance of considered eddy-viscosity models.

One of the codes, the OpenFOAM open-source simulation software, relies on a basic second-order finite-volume method for unstructured meshes. The convective part is discretized using the hybrid scheme of Travin et al. [33], which provides a blend of the second-order central differences and upwind schemes. The sonicFoam flow solver has been used for the simulations in the present work. sonicFoam has been set up to have two PISO loops, i.e. nCorrectors = 2, and two additional outer loops, i.e. nOuterCorrectors = 2.

These setup values had been found previously as otherwise, there was a substantial mismatch between numerical and experimental hydrodynamic results.

The second algorithm is represented in the NOISEtte code [34, 35]. It is based on a higher-accuracy scheme with an extended numerical stencil, namely, the EBR (Edge-Based Reconstruction) scheme [8] with an edge-based quasi-1D reconstruction of variables. The hybrid scheme for convective terms uses the adapting blend of the central-difference and upwind schemes [9] based on an extended numerical stencil containing four points with the special hybridizing function [36]. The values of the sensor function ([33] in Open-FOAM and [36] in NOISEtte), which controls the amount of diffusion ($\sigma_{\rm upw}$) in the hybrid schemes, are limited both from below and from above, similarly to [9].

In both codes, implicit second-order schemes are used for temporal integration. The maximum Courant–Friedrichs–Lewy (CFL) was set to 5 in all the simulations. Since the size of the time step directly affects the computational cost, but can also affect the accuracy of the results, several preliminary simulations were performed for CFL values in the range from 0.9 to 10 to ensure that the time step is small enough not to affect simulation results.

To predict far-field acoustics, the Lighthill acoustic analogy in the form of a modified version of the integral Ffowcs Williams and Hawkings (FWH) method [37] is used. The NOISEtte's acoustic postprocessor is based on the formulation 1A proposed by Farassat [38] in terms of retarded times. Acoustic post-processing of the OpenFOAM results is done via an in-house FWH solver based on Fourier Analysis, obtaining the equivalent FWH equation but in Fourier space. This methodology effectively removes the requirement of retarded time computations, which is substituted by its equivalent in Fourier space: a phase shift between observer and source. According to Shur et al. [2, 39], the data for acoustic post-processing is accumulated on nested closed permeable control surfaces, excluding the "quadrupole" volume terms. The density-by-pressure substitution assuming the isentropic relations [39] and average over both the outflow-discs [2] and conical "sleeve" surfaces [40] is applied in order to reduce spurious non-physical noise (see the parts of the permeable surfaces marked by solid yellow lines in Figure 3.2). All the far-field noise characteristics are obtained at a distance of 98D from the jet nozzle center.

To improve the convergence of the results, they are calculated at 32 azimuthally equidistant points (for each observer's angle), followed by averaging.

The time of accumulation for the unsteady simulation data for further post-processing (both near-field aerodynamics and far-field acoustics) is at least $250D/U_{\rm jet}$. The transient period (from the uniform fields) takes about $250D/U_{\rm jet}$, but it is significantly reduced by either using the developed flow computed using a different approach or by interpolating from a coarser (or a finer) mesh.

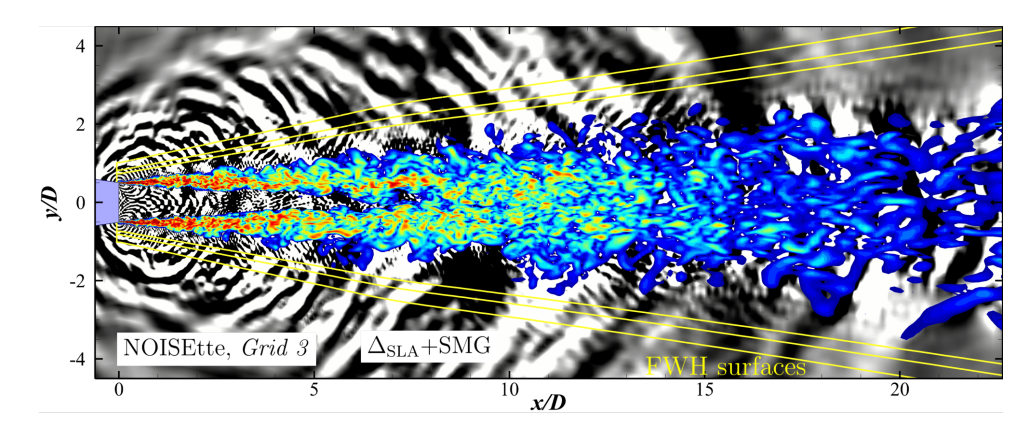


Figure 3.2: The instantaneous flow field in the jet plume region (the NOISEtte simulation on the *Grid 3* mesh using the Δ_{SLA} +SMG approach). The yellow lines mark the location of the FWH control surfaces

NOISEtte simulations are carried out on hybrid GPU-based clusters using the heterogeneous version [35]. It uses portable multilevel MPI + OpenMP + OpenCL parallelization for computing on manycore CPUs and GPUs. Information about the computational cost of simulation of 100 dimensionless time units $(100D/U_{\rm jet})$ is presented in Table 3.2. The number of time steps performed is about 20 thousand. On CPUs, the performance of the Open-FOAM and NOISEtte codes is comparable, the latter is even faster, despite the higher-accuracy scheme used. In must be noted that the overall performance depend on the specific solver set-ups, such as the time integration methods. On GPUs, NOISEtte demonstrates significant acceleration, getting the equivalent of about 150 CPU cores from a single device.

Code	Hardware configuration	Time, h
OpenFOAM	2 × 24-core Intel Xeon Platinum 8160	23
NOISEtte	2×24 -core Intel Xeon Platinum 8160	12
NOISEtte	2 × 24-core Intel Xeon Gold 6142	1.8
	and $2 \times GPU$ NVIDIA V100	

Table 3.2: Computational cost of $100D/U_{jet}$ time units on *Grid 3*

3.4 Results and Discussion

3.4.1 Influence of GAM Approaches on Jet Plume Aerodynamics

We evaluate the impact of using all the considered dynamic adapting subgrid length scales, including their combinations with alternative LES models, on the jet plume aerodynamics. Simulations on *Grid* 2 use the DDES method with the following configurations: $\Delta_{\rm vol}$, Δ_{ω} , $\tilde{\Delta}_{\omega}$, $\Delta_{\rm SLA}$ and $\Delta_{\rm lsq}$ with Smagorinsky (SMG) model; $\tilde{\Delta}_{\omega}+\sigma$; $\Delta_{\rm lsq}+{\rm S3QR}$. Note that some of them are already investigated in the paper [22].

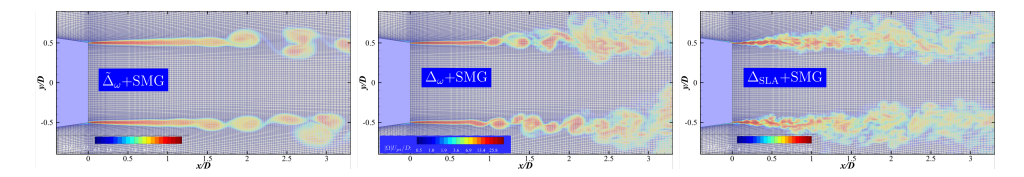


Figure 3.3: Instantaneous flow fields (vorticity magnitude, $|\Omega|$) on the *Grid* 2 mesh in the mid-span section: strongly delayed RANS-to-LES transition in the shear layer using the SGS $\tilde{\Delta}_{\omega}$ (left), delayed transition using Δ_{ω} (center) and rapid transition using Δ_{SLA} .

Grid 2, like the other meshes considered, is typical for the jet case simulation (see the mesh patterns colored by instantaneous fields from the solutions with a varying delay of the transition in Figure 3.3). The mesh has the finest resolution (in the radial direction) near the nozzle to resolve the boundary layer and the shear layer with coarsening downstream (usually smoother in

the streamwise and faster in the radial directions), while the number of mesh nodes in the azimuthal direction remains the same. The mesh resolution and both turbulent and numerical dissipation coming from the scale-resolving algorithm define the possibility of provoking the transition. This "numerical" transition resembles the Kelvin-Helmholz instability, accompanied by generation of quasi-2D, correlated over the azimuthal direction, structures with evolution to 3D turbulence downstream (see Figured 3.3 left and center). The appearance of these quasi-2D structures manifests in the form of an overestimation of the turbulence characteristics in the initial part of the shear layer (see the "humps" in the graphs of rms(u') in Figures 3.5 and 3.9).

When the flow becomes plausibly 3D right near the nozzle edge (like in Figure 3.3 right), it usually does not noticeably influence the prediction of the far-field noise. Conversely, the delay in the RANS-to-LES transition (like in Figure 3.3 left and center) leads to a drastic overestimation of jet acoustics [2,3,31]. This is caused by the intensification and enlargement of non-physical quasi-2D structures that inevitably accompany such a transition. Due to their azimuthal correlation and their large size, which increases while mesh coarsening downstream the nozzle edge, they generate spurious noise contaminating the jet acoustics characteristics. As for the flow after transition, a nonappropriate (usually lower than "enough") amount of subgrid turbulent viscosity can result in the generation of spurious noise. It affects predominantly at the higher Strouhal numbers, too.

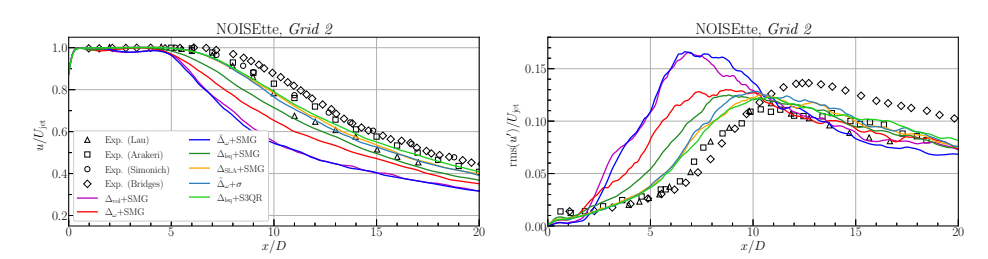


Figure 3.4: Centerline distributions of streamwise velocity (left) and its rms (right) obtained using all the considered combinations.

The centerline and lipline distributions of streamwise velocity and its rms values are presented in Figures 3.4 and 3.5. The graphs demonstrate

the following properties of the considered approaches. The usage of $\tilde{\Delta}_{\omega}$, $\Delta_{\rm vol}$, Δ_{ω} and $\Delta_{\rm lsq}$ with SMG clearly leads to the delay of the RANS-to-LES transition. This effect is more pronounced for $\tilde{\Delta}_{\omega}$ and Δ_{vol} than for Δ_{ω} and Δ_{lsq} . The absence of quick transition in the early shear layer region generally yields drastic underprediction of the jet flow. More precisely, the result of the delay is manifested in the following. First, underprediction of the jet core region is observed (see Figure 3.4 left): the location of dumping the jet centerline velocity is shifted upstream. Second, there is strong overprediction of streamwise velocity rms values at $2 \lesssim x/D \lesssim 11$ downstream the nozzle along both the jet center and the lip line. Moreover, the underprediction of rms(u') starting from x/D = 10 in the shear layer is also characteristic. The attenuation of the delay with consequent better prediction of jet plume aerodynamics is strongly correlated with the behavior of distributions of turbulent viscosity levels presented in Figure 3.6. It is seen that the decreasing of v_t/v leads to the suppression of the GAM problem and, in turn, towards better jet plume aerodynamics prediction.

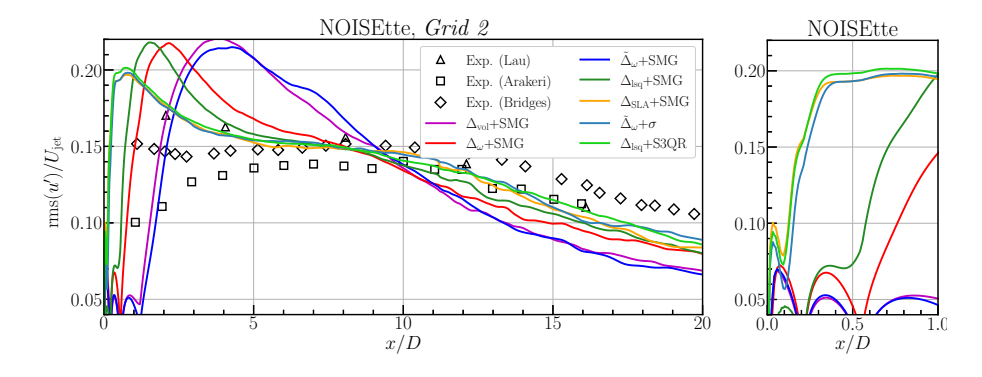


Figure 3.5: Lipline distributions of the rms of streamwise velocity obtained using all the considered combinations.

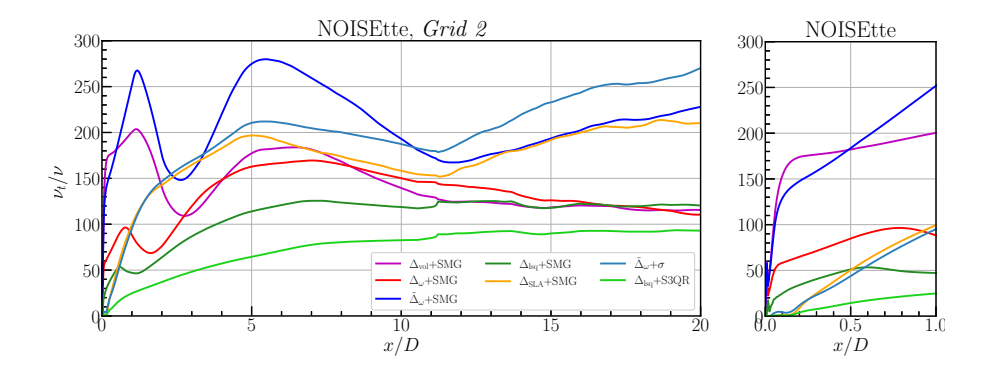


Figure 3.6: Lipline distributions v_t/v obtained using all the considered combinations.

The simulations carried out using Δ_{SLA} +SMG, Δ_{lsq} +S3QR and Δ_{ω} + σ demonstrate a fast RANS-to-LES transition in the shear layers and a quite accurate prediction of the jet near field characteristics, as evidenced by their comparisons with the experimental data in Figures 3.4 and 3.5. When using these combinations, the values of u and rms(u') do not differ much from each other both along the center line and along the lip line of the jet, while the v_t/v levels along the lip line differ noticeably (see Figure 3.6). Similar results for these models were obtained in the paper [22]. Thus, it is of interest how the use of different approaches (that allow simulating the jet plume correctly) affects the prediction of noise in the far-field. The next part of the chapter is dedicated to investigating the performance of the selected enhanced DDES modifications $(\Delta_{SLA}+SMG, \tilde{\Delta}_{\omega}+\sigma \text{ and } \Delta_{lsq}+S3QR)$ on jet acoustics. Other configurations that allow such unacceptable delay in the transition in the shear layer are not considered for further study because they result in strong misprediction of the far-field noise. The same effect was demonstrated by Shur et al. [3] where the $\tilde{\Delta}_{\omega}$ +SMG was considered too.

3.4.2 Influence of the Selected GAM Approaches on Jet Aerodynamics for a Set of Refining Meshes

The comparison of both the center and lipline distributions of streamwise velocity and rms of its pulsations using both NOISEtte and OpenFOAM codes on a set of refining meshes is presented in figures 3.7-3.9. A noticeable trend,

typical for all the considered approaches and numerical algorithms, is that the mesh refining leads to better agreement of the results with the experimental data. It can be stated that convergence is achieved on the *Grid 3* mesh. As for the comparison of the results obtained using different numerical algorithms with each other, it is seen from Figures 3.7-3.9 that the NOISEtte ones are closer to the reference on the same mesh, thanks to the usage of higher accuracy numerical scheme.

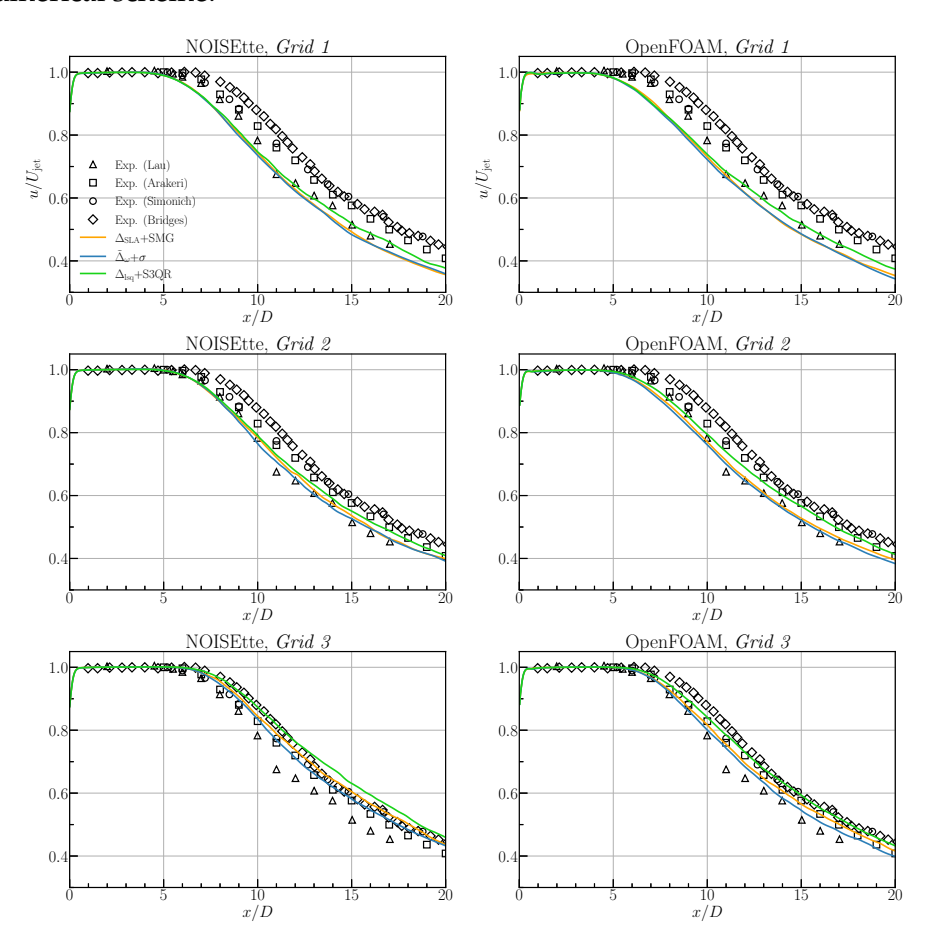


Figure 3.7: Centerline distributions of the streamwise velocity obtained using NOISEtte (left) and OpenFOAM (right) on a set of refining meshes (top to bottom).

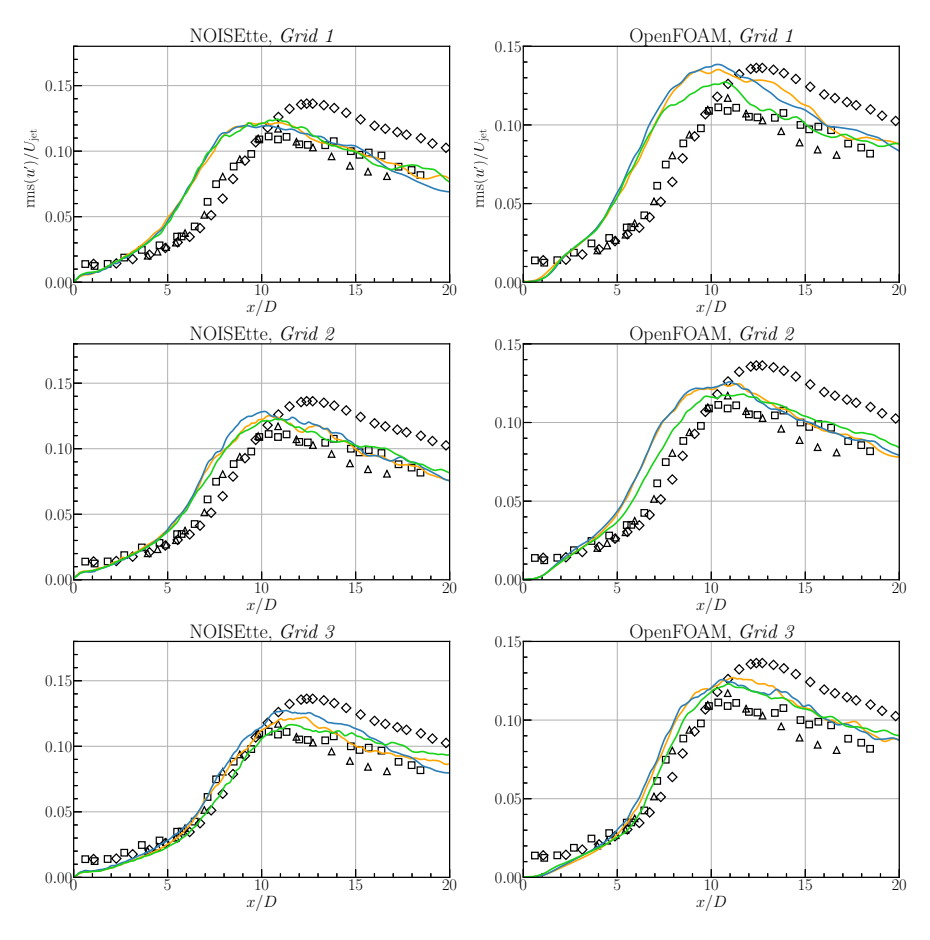


Figure 3.8: Centerline distributions the streamwise velocity pulsations rms obtained using NOISEtte (left) and OpenFOAM (right) on a set of refining meshes (top to bottom).

The behavior of the Reynolds stresses in the initial part of the shear layer, presented by the rms(u') in Figure 3.9, requires special attention. A wide peak characterises all the results at $0.2 \lesssim x/D < \lesssim 2$ that is present in all the computations and, depending on mesh and numerical algorithm, one or more narrow peaks earlier. All of them are the consequence of not physical but "numerical" solution transition in the early shear layer region, from steady RANS to resolved LES. The width and power of the peaks depend on the

properties of the computational algorithm, models, and mesh resolution. The result of mitigation of this problem, either by the usage of the GAM approach or by mesh refining, is manifested by a narrowing of the peaks and a reduction of the corresponding maximum values. This can be traced, for example, by the results using $\tilde{\Delta}_{\omega}$ + σ (see graphs of Figure 3.9, from top to bottom).

In general, analyzing the graphs in Figures 3.7-3.9, we can say that for all the approaches, there is mesh convergence in the jet plume aerodynamics.

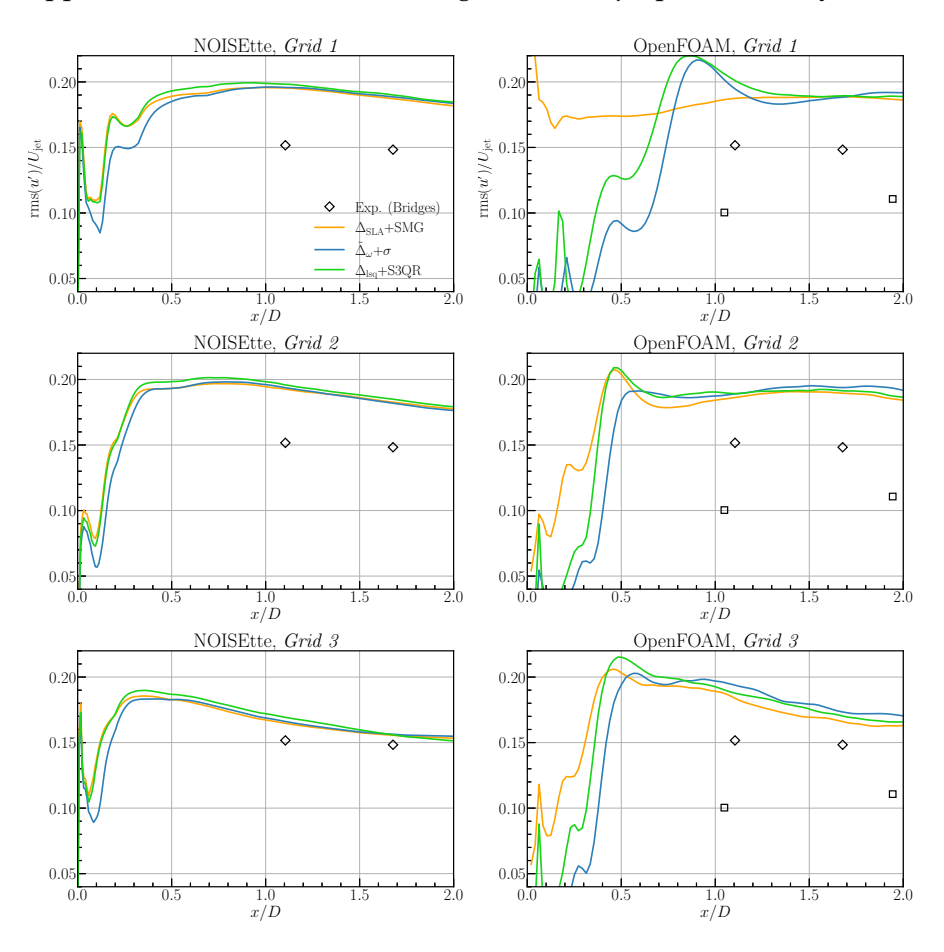


Figure 3.9: Lipline distributions of the streamwise velocity pulsations rms obtained using NOISEtte (left) and OpenFOAM (right) on a set of refining meshes (top to bottom).

3.4.3 Influence of the Selected GAM Approaches on Jet Aeroacoustics for a Set of Refining Meshes

In contrast to the near-field aerodynamics results, the correct prediction of noise in the jet far-field is a more challenging task. As was mentioned above, both simulation of physical noise sources and the possible appearance of "spurious" sources are very sensitive to the scale-resolving approach used. NOISEtte and OpenFOAM results are presented in Figures 3.10-3.12. The overall sound pressure levels' (OASPL) distributions (noise directivity) are shown in Figure 3.10. Figures 3.11 and 3.12 plot $1/3^{\rm rd}$ octave integrated spectrums at the observer angles $\theta = 60^{\circ}$ and $\theta = 150^{\circ}$, respectively ($\theta = 180^{\circ}$ corresponds to the jet downstream direction). These angles (marked by vertical dashed lines in Figure 3.10) are chosen as representative ones to emphasize and analyze the discrepancy between the different approaches considered and the experimental data.

Considering all the results in general, the following observations and conclusions could be revealed. First of all, it is common for all the considered approaches that mesh refinement leads to better correspondence with the reference data and less difference from each other. In contrast to the corresponding NOISEtte results, OpenFOAM results obtained using different approaches on the same meshes are more correlated with each other and appear more stable (independent of either approach or mesh). This is explained by the use of a higher-accuracy numerical scheme in NOISEtte in contrast to OpenFOAM, where numerical dissipation and related errors dominate. So the peculiarities of the different LES models and SGS emerge more vividly.

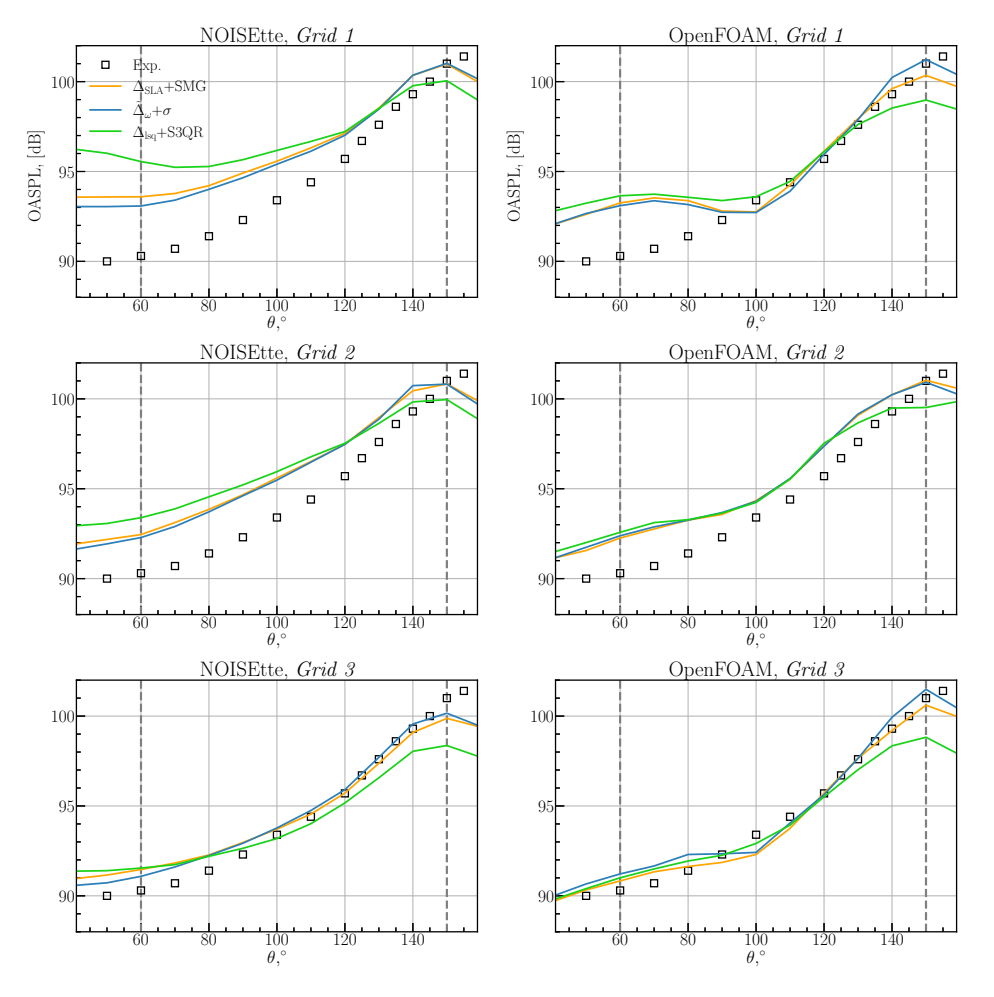


Figure 3.10: Noise directivity obtained using NOISEtte (left) and OpenFOAM (right) on a set of refining meshes (top to bottom).

When evaluating the OASPL distributions obtained using the NOISEtte code (Figure 3.10 left), the following common trend of discrepancy with experimental data is seen: overestimation of the noise levels at the lower observer angles and underestimation at the higher ones, at the same time. It is more pronounced when $\Delta_{\rm lsq}$ in combination with the S3QR model is used. This effect is amplified while mesh coarsening.

The overestimation of the noise levels for $\theta \lesssim 100^\circ$ is related to the spurious noise generation in the early shear layer region due to the nonphysical RANS-to-LES transition accompanied by instabilities provided by the low-dissipative numerical scheme. It manifests on the part of the spectrum at the higher Strouhal numbers, $St \geq 1$ (see Figure 3.11, for instance), especially on the most coarse mesh $Grid\ 1$ (the left graphs).

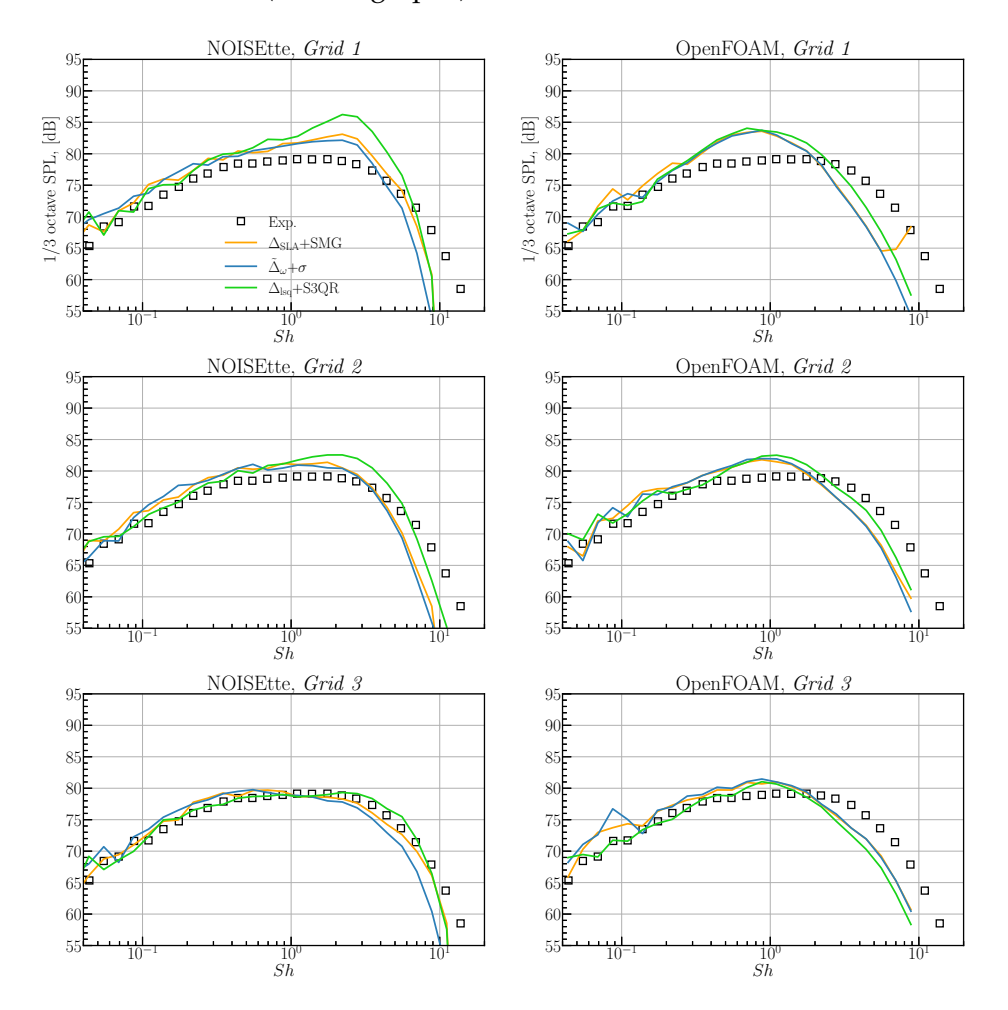


Figure 3.11: 1/3rd-octave integrated spectrums at the observer angle $\theta = 60^{\circ}$ using NOISEtte (left) and OpenFOAM (right) on a set of refining meshes (top to bottom)..

The significant underestimation of noise levels at $\theta > 130^\circ$ comes from "noise deficit", mostly at lower Strouhal numbers in the vicinity of noise peak (in the range 0.2 < Sh < 0.9, approximately) that is seen in Figure 3.12. Noise in this range of Strouhal numbers is associated with the dynamics of large vortices with a size of the order of the nozzle diameter. This effect is similar to the results obtained using the Implicit LES approach in [31] on the same meshes *Grid 1*, *Grid 2* and *Grid 3*. Nevertheless, on *Grid 3*, all the considered approaches allow predicting the OASPL in the range $50^\circ < \theta < 140^\circ$ with an error below 1.4 dB compared to the experiment (it is more clearly seen in Figure 3.13 top). The revealed differences from the experiment for the considered models are analyzed in detail in the next subsection using the results obtained on *Grid 3*.

Distinguished trends characterize the OASPL distributions obtained using OpenFOAM compared with the NOISEtte ones. As can be seen in Figure 3.10 bottom, the predicted noise levels better agree with the experiment in the range $90^{\circ} < \theta < 130^{\circ}$ on *Grid 1* and *Grid 2*, the deviation is within 2 dB. At the same time, the OpenFOAM results at $\theta < 90^{\circ}$ demonstrate comparable overestimation of OASPL as the NOISEtte ones. As was mentioned above, in contrast to the NOISEtte, all the considered approaches provide very similar far-field results when OpenFOAM algorithm is used. This is true for both overall values and spectral distributions.

The $1/3^{\rm rd}$ octave spectrums at $\theta=60^\circ$ and $\theta=150^\circ$ (Figures 3.11 and 3.12, respectively) obtained using the NOISEtte reveal the following properties of the GAM strategies considered. First, the usage of the $\tilde{\Delta}_\omega+\sigma$ combination leads to earlier decay of the spectrum compared to the remaining approaches. At the same time, it provides the lowest overestimation of the SPL at $\theta=60^\circ$ and the lowest underestimation at $\theta=150^\circ$. The usage of the $\Delta_{\rm SLA}$ results in similar behavior of the solution.

As for the OpenFOAM results presented (Figures 3.11-3.12 bottom), due to higher numerical dissipation provided by the spatial discretization scheme, the noise levels are not overestimated in the region 1 < Sh < 4 for $\theta < 60^{\circ}$, but the graphs start to drop earlier together with a shift in the "overestimation peak" towards lower Strouhal numbers (0.3 < Sh < 2). So, actual resolution capability of the OpenFOAM algorithm ends up at $Sh = 1 \div 2$. The plots in Figure 3.12 bottom demonstrate noticeable underestimation of the noise levels for the Strouhal numbers after the peak of the spectrum (at $Sh \gtrsim 0.4$).

Such behavior, again, is explained by the fact that the accuracy provided by the scheme used in the OpenFOAM is not enough to resolve small vortexes contributing to noise propagating far downstream of the nozzle exit.

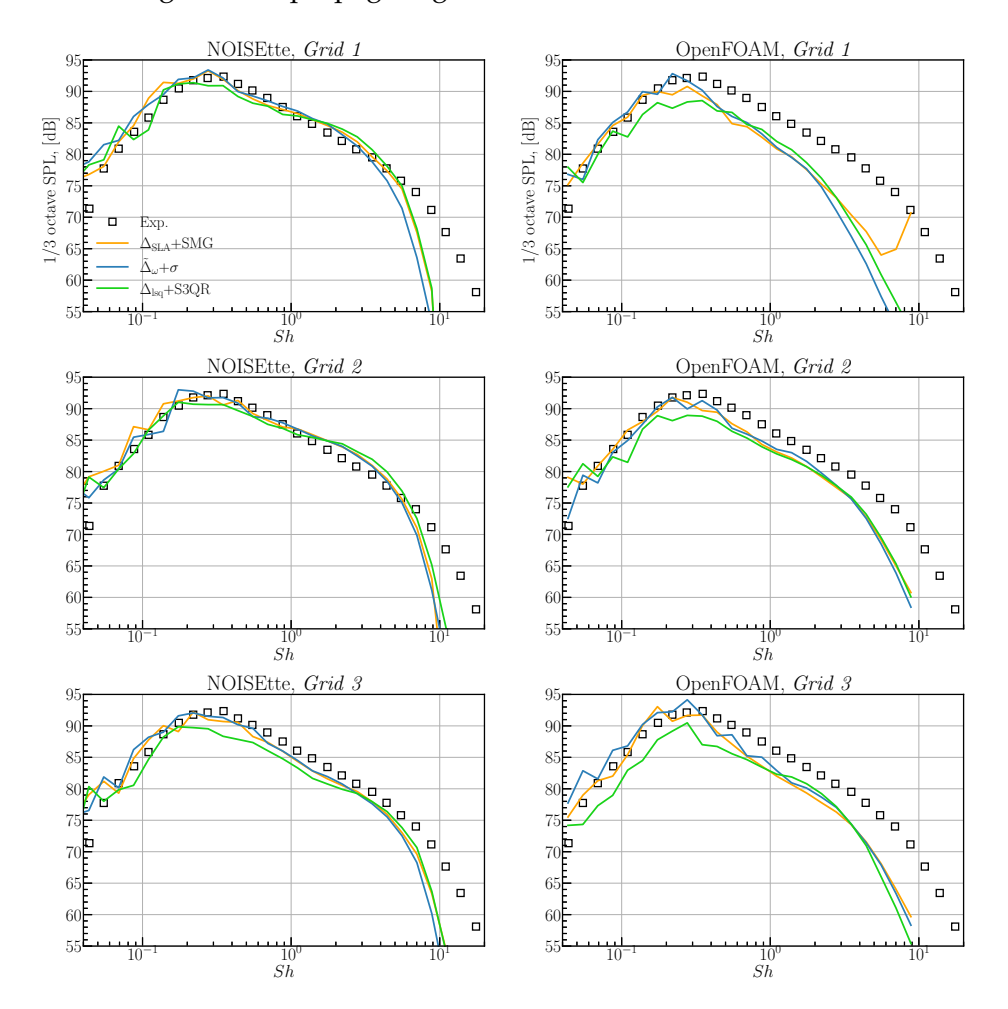


Figure 3.12: 1/3rd-octave integrated spectrums at the observer angle $\theta = 150^{\circ}$ using NOISEtte (left) and OpenFOAM (right) on a set of refining meshes (top to bottom).

3.4.4 Evaluation of Far-Field Results on *Grid 3*

We have demonstrated mesh convergence for the near-field flow dynamics and far-field noise results for the three considered combinations with GAM properties: $\Delta_{\rm SLA}+{\rm SMG},\,\Delta_{\rm lsq}+{\rm S3QR}$ and $\tilde{\Delta}_\omega+\sigma.$ As was already mentioned, the deviations from the experimental values are characterized by overestimation at lower observer angles and underestimation at higher ones. However, it remains unclear why these combinations differ to some extent in the magnitude of these deviations. To shed more light on this issue, let us consider other combinations that provide fast RANS-to-LES transition (which is critical) in the early shear layer region: $\Delta_{\rm vol}+\sigma,\,\Delta_{\rm lsq}+{\rm SMG}$ and $\Delta_{\rm min}+{\rm SMG}$. This will allow us to study in more detail the dependence of the far-field noise deviations from the experiment on the level of turbulent viscosity of the LES approach inside the shear layer.

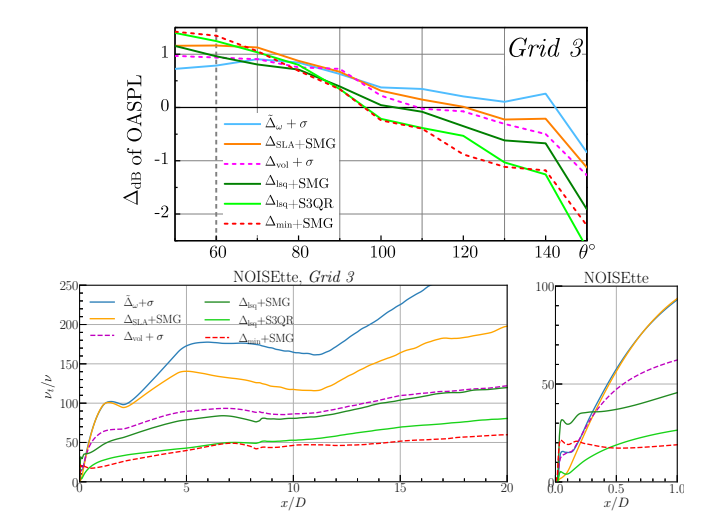


Figure 3.13: Deviation of OASPL from the experimental data in dB $\Delta_{\rm dB} = {\rm OASPL_{comp}} - {\rm OASPL_{exp}}$ (top) and lipline distributions of ν_t/ν (bottom) obtained on *Grid 3*.

The deviation of OASPL from the experimental data (in dB) is shown together with the ratio of turbulent to molecular viscosity in Figure 3.13. It is

seen that the overestimation of the noise levels at the lower observer angles and underestimation at the higher ones correlates with the distributions of v_t/v . Therefore, Figure 3.13 demonstrates that approaches with higher turbulent viscosity throughout the entire shear layer region (except the initial part, which is crucial to provoke the RANS-to-LES transition), $\tilde{\Delta}_{\omega}+\sigma$ and $\Delta_{\rm SLA}+{\rm SMG}$, (slightly) better agree with the experiment. At low turbulent viscosity, the deviation is bigger, regardless of whether such low v_t is caused by the SGS alone, as for $\Delta_{\rm min}+{\rm SMG}$, or also by the LES model, as in the case of $\Delta_{\rm lsq}+{\rm S3QR}$. The rest the combinations considered, $\Delta_{\rm vol}+\sigma$ and $\Delta_{\rm lsq}+{\rm SMG}$, lie between the the above-mentioned groups in terms of the discrepancy with the experiment. The mesh convergence results in the previous subsection demonstrate that approaches with higher values of v_t (like $\tilde{\Delta}_{\omega}+\sigma$) show better convergence of the far-field noise characteristics than approaches providing lower subgrid viscosity (such as $\Delta_{\rm lsq}+{\rm S3QR}$). This phenomenon is also present when using OpenFOAM (see the results of $\Delta_{\rm lsq}+{\rm S3QR}$ in Figures 3.11-3.12 bottom).

3.5 Conclusions

New enhanced eddy-viscosity models within the hybrid RANS-LES DDES method have been investigated. The enhancement considers using GAM approaches by implying either flow-dependent dynamic subgrid scales, alternative LES models sensitive to 2D flows, or both. The object of investigation is the immersed unheated subsonic turbulent jet. The effect of using different GAM techniques on near-field aerodynamics and far-field aeroacoustics is evaluated based on the comparison with experimental reference data. The simulations are carried out using two different control volume numerical algorithms realized in the codes NOISEtte and OpenFOAM, respectively, on a set of refining meshes. The crucial difference between them is that the first one uses a higher-accuracy scheme to approximate the convective fluxes, while the second uses a regular second-order scheme.

The testing of various combinations of SGS and alternative LES models as applied to the scale-resolving simulation of the jet on the *Grid* 2 mesh is characterized by the following results. Using $\tilde{\Delta}_{\omega}$, $\Delta_{\rm vol}$, Δ_{ω} and $\Delta_{\rm lsq}$ coupled with the SMG model leads to a delay in the transition from RANS to LES, followed by a strong mismatch between the computational results and the

102 §3.5 Conclusions

reference data in the jet plume. Unlike them, the GAM-enhanced combinations $\Delta_{SLA}+SMG$, $\tilde{\Delta}_{\omega}+\sigma$, and $\Delta_{lsq}+S3QR$ allow mitigating the gray area problem with significant and very similar influence on the jet near field aerodynamics. This conclusion is equally valid for the both numerical algorithms considered.

So the study of their capability to predict far-field noise on a set of refining meshes is conducted. The investigation clearly demonstrated the crucial role of the numerical scheme for convective fluxes used. Thus, using a higher accuracy numerical scheme allows the evaluation of the performance and sensitivity of different GAM approaches. Basic $2^{\rm nd}$ -order schemes, as in Open-FOAM, do not permit (at least for practical mesh resolution) to reveal the subtle effect of the subgrid-scale model on the solution in the GAM-enhanced combinations. The lack of scheme accuracy leads to a noticeable underestimation of far-field noise at higher Strouhal numbers (for Sh > 2 at $\theta = 60^{\circ}$ and for Sh > 0.4 at $\theta = 150^{\circ}$).

This investigation revealed that the usage of advanced GAM techniques is required to obtain plausible results on practical meshes. It implies a combination of a SGS model that switches off for 2D flows (F_{KH} function plays this role for Δ_{SLA} +SMG combination) and a Δ_{SGS} that is close to or lesser than Δ_{min} in the initial part of the shear layer.

Using only enhanced dynamic length scales does not guarantee adequate results, because it does not ensure proper diminishing of turbulent viscosity in the initial part of the shear layer. The considered Δ_{SGS} , except for Δ_{SLA} due to the F_{KH} function, provide the values in the range between Δ_{min} and Δ_{max} , with Δ_{lsq} having the smallest values close to Δ_{min} , $\tilde{\Delta}_{\omega}$ the largest. As for their behavior in the 3D flow regions, after transition, it appears to be consistent with either Δ_{vol} (Δ_{ω} and Δ_{lsq}) or Δ_{max} ($\tilde{\Delta}_{\omega}$ and Δ_{SLA}).

The study has shown that using an alternative LES model (like σ or S3QR) is crucial in the initial part of the shear layer, while its impact is weak in the remaining areas (downstream of the nozzle exit). It has revealed that using either any of the considered alternative LES models or the F_{KH} function (as a part of Δ_{SLA}) may significantly reduce the subgrid turbulent viscosity in the initial part of the shear layer, provoking the RANS-to-LES transition. So they are sufficiently reliable candidates for the gray area mitigation. At the same time, the use of alternative LES operators, rather than the F_{KH} function, is preferable due to their less empirical nature and the fact that the function can unexpectedly operate in areas with resolved turbulence.

All the considered advanced combinations of Δ_{SGS} and \mathcal{D}_{LES} allow obtaining consistent with the experiment mesh-converged solution in the jet near field. As for the far field, despite the different behavior of the solution in the convergence on a set of refining meshes, on the finest one, all the considered advanced GAM approaches predict the noise adequately. Note that the *Grid 3* mesh which provides adequate results is still relatively coarse: the number of cells is about an order of magnitude smaller than in the meshes used nowadays [1,6,11] in simulations of turbulent jets.

In summary, all of the GAM-enhanced combinations considered, Δ_{SLA} +SMG, $\tilde{\Delta}_{\omega}$ + σ , and Δ_{lsq} +S3QR, demonstrate reasonably accurate results, which are close to each other. However, if we look in more detail, the results show that the magnitude of deviations from the reference data (overestimation of the noise levels at the lower observer angles and underestimation at the higher ones) correlates with the subgrid eddy viscosity distributions, so that diminishing of ν_t leads to an increase in discrepancy with the experiment. At the same time, approaches based on the use of subgrid scales close to Δ_{max} in the region of resolved turbulence allow to obtain more accurate results that converge faster to the experiment in terms of mesh convergence. Thus, the $\tilde{\Delta}_{\omega}$ + σ combination is the most prominent example of this. Conversely, the use of close-to- Δ_{vol} subgrid scales is more likely to lead to less accurate results in far-field aeroacoustics. Thus, among these three combinations, the Δ_{lsq} with the S3QR model demonstrates slightly worse noise prediction.

References

- [1] Christophe Bogey. Grid sensitivity of flow field and noise of highreynolds-number jets computed by large-eddy simulation. *International Journal of Aeroacoustics*, 17(4-5):399–424, may 2018.
- [2] Michael L. Shur, Philippe R. Spalart, and Michael Kh. Strelets. Noise prediction for increasingly complex jets. part i: Methods and tests. *International Journal of Aeroacoustics*, 4(3):213–245, jul 2005.
- [3] Michael L Shur, Philippe R Spalart, and Michael K Strelets. Jet noise computation based on enhanced DES formulations accelerating the RANS-to-

- LES transition in free shear layers. *International Journal of Aeroacoustics*, 15(6-7):595–613, jul 2016.
- [4] James Tyacke, Iftekhar Naqavi, Zhong-Nan Wang, Paul Tucker, and Peer Boehning. Predictive large eddy simulation for jet aeroacoustics—current approach and industrial application. *Journal of Turbomachinery*, 139(8), mar 2017.
- [5] M. Fuchs, C. Mockett, M. Shur, M. Strelets, and J. C. Kok. Single-stream round jet at m = 0.9. In *Notes on Numerical Fluid Mechanics and Multidisciplinary Design*, pages 125–137. Springer International Publishing, jul 2017.
- [6] F. Gand and M. Huet. On the generation of turbulent inflow for hybrid RANS/LES jet flow simulations. *Computers & Fluids*, 216:104816, feb 2021.
- [7] Jesus Ruano, Aleix Baez Vidal, Joaquim Rigola, and Francesc Xavier Trias. A new general method to compute dispersion errors on cartesian stretched meshes for both linear and non-linear operators. *Computer Physics Communications*, 271:108192, feb 2022.
- [8] Ilya Abalakin, Pavel Bakhvalov, and Tatiana Kozubskaya. Edge-based reconstruction schemes for unstructured tetrahedral meshes. *International Journal for Numerical Methods in Fluids*, 81(6):331–356, dec 2015.
- [9] Alexey P. Duben and Tatiana K. Kozubskaya. Evaluation of quasi-one-dimensional unstructured method for jet noise prediction. *AIAA Journal*, 57(12):5142–5155, dec 2019.
- [10] Guillaume A. Brès, Frank E. Ham, Joseph W. Nichols, and Sanjiva K. Lele. Unstructured large-eddy simulations of supersonic jets. *AIAA Journal*, 55(4):1164–1184, apr 2017.
- [11] Guillaume A. Brès, Peter Jordan, Vincent Jaunet, Maxime Le Rallic, André V. G. Cavalieri, Aaron Towne, Sanjiva K. Lele, Tim Colonius, and Oliver T. Schmidt. Importance of the nozzle-exit boundary-layer state in subsonic turbulent jets. *Journal of Fluid Mechanics*, 851:83–124, jul 2018.

[12] Nicolas Chauvet, Sebastien Deck, and Laurent Jacquin. Zonal detached eddy simulation of a controlled propulsive jet. *AIAA Journal*, 45(10):2458–2473, oct 2007.

- [13] Sébastien Deck. Recent improvements in the zonal detached eddy simulation (ZDES) formulation. *Theoretical and Computational Fluid Dynamics*, 26(6):523–550, oct 2011.
- [14] Charles Mockett, Marian Fuchs, Andrey Garbaruk, Michael Shur, Philippe Spalart, Michael Strelets, Frank Thiele, and Andrey Travin. Two non-zonal approaches to accelerate RANS to LES transition of free shear layers in DES. In *Progress in Hybrid RANS-LES Modelling*, pages 187–201. Springer International Publishing, 2015.
- [15] Mikhail L. Shur, Philippe R. Spalart, Mikhail Kh. Strelets, and Andrey K. Travin. An enhanced version of DES with rapid transition from RANS to LES in separated flows. Flow, Turbulence and Combustion volume, 95(4):709–737, jun 2015.
- [16] F. X. Trias, A. Gorobets, M. H. Silvis, R. W. C. P. Verstappen, and A. Oliva. A new subgrid characteristic length for turbulence simulations on anisotropic grids. *Physics of Fluids*, 29(11):115109, nov 2017.
- [17] Franck Nicoud, Hubert Baya Toda, Olivier Cabrit, Sanjeeb Bose, and Jungil Lee. Using singular values to build a subgrid-scale model for large eddy simulations. *Physics of Fluids*, 23(8):085106, aug 2011.
- [18] F. X. Trias, D. Folch, A. Gorobets, and A. Oliva. Building proper invariants for eddy-viscosity subgrid-scale models. *Physics of Fluids*, 27(6):065103, jun 2015.
- [19] P. R. Spalart, W.-H. Jou, M. Strelets, S. R. Allmaras, C. Liu, Z. Liu, and L. Sakell. Comments on the feasibility of les for wings, and on a hybrid rans/les approach, international conference; 1st, advances in dns/les: Direct numerical simulation and large eddy simulation. In *Advances in DNS/LES: Direct numerical simulation and large eddy simulation, International conference; 1st, Advances in DNS/LES: Direct numerical simulation and large eddy simulation,* pages 137–148. Greyden Press;, 1997.

[20] P. R. Spalart, S. Deck, M. L. Shur, K. D. Squires, M. Kh. Strelets, and A. Travin. A new version of detached-eddy simulation, resistant to ambiguous grid densities. *Theoretical and Computational Fluid Dynamics*, 20(3):181–195, may 2006.

- [21] Mikhail L. Shur, Philippe R. Spalart, Mikhail Kh. Strelets, and Andrey K. Travin. A hybrid RANS-LES approach with delayed-DES and wall-modelled LES capabilities. *International Journal of Heat and Fluid Flow*, 29(6):1638–1649, dec 2008.
- [22] Arnau Pont-Vílchez, Alexey Duben, Andrey Gorobets, Alistair Revell, Assensi Oliva, and F. Xavier Trias. New strategies for mitigating the gray area in delayed-detached eddy simulation models. *AIAA Journal*, 59(9):3331–3345, sep 2021.
- [23] Ali Uzun and M. Youssuff Hussaini. Some issues in large-eddy simulations for chevron nozzle jet flows. *Journal of Propulsion and Power*, 28(2):246–258, mar 2012.
- [24] Anton P. Markesteijn, Vasily Gryazev, Sergey A. Karabasov, Ruslan Sh. Ayupov, Leonid A. Benderskiy, and Dmitriy A. Lyubimov. Flow and noise predictions of coaxial jets. *AIAA Journal*, 58(12):5280–5293, dec 2020.
- [25] K. VISWANATHAN. Aeroacoustics of hot jets. *Journal of Fluid Mechanics*, 516:39–82, oct 2004.
- [26] Jark C. Lau, Philip J. Morris, and Michael J. Fisher. Measurements in subsonic and supersonic free jets using a laser velocimeter. *Journal of Fluid Mechanics*, 93(1):1–27, jul 1979.
- [27] J. C. Lau. Effects of exit mach number and temperature on mean-flow and turbulence characteristics in round jets. *Journal of Fluid Mechanics*, 105(-1):193, apr 1981.
- [28] J. Simonich, S. Narayanan, T. Barber, and M. Nishimura. High subsonic jet experiments. i - aeroacoustic characterization, noise reduction and dimensional scaling effects. In 6th Aeroacoustics Conference and Exhibit. American Institute of Aeronautics and Astronautics, jun 2000.

[29] V. H. ARAKERI, A. KROTHAPALLI, V. SIDDAVARAM, M. B. ALKISLAR, and L. M. LOURENCO. On the use of microjets to suppress turbulence in a mach 0.9 axisymmetric jet. *Journal of Fluid Mechanics*, 490:75–98, sep 2003.

- [30] James Bridges and Mark Wernet. Establishing consensus turbulence statistics for hot subsonic jets. In *16th AIAA/CEAS Aeroacoustics Conference*. American Institute of Aeronautics and Astronautics, jun 2010.
- [31] M.L. Shur, P.R. Spalart, and M.Kh. Strelets. LES-based evaluation of a microjet noise reduction concept in static and flight conditions. *Procedia Engineering*, 6:44–53, 2010.
- [32] Anton P. Markesteijn and Sergey A. Karabasov. CABARET solutions on graphics processing units for NASA jets: Grid sensitivity and unsteady inflow condition effect. *Comptes Rendus Mécanique*, 346(10):948–963, oct 2018.
- [33] A. Travin, M. Shur, M. Strelets, and P. R. Spalart. Physical and numerical upgrades in the detached-eddy simulation of complex turbulent flows. In *Fluid Mechanics and Its Applications*, pages 239–254. Springer Netherlands, 2002.
- [34] A. Gorobets. Parallel algorithm of the NOISEtte code for CFD and CAA simulations. *Lobachevskii Journal of Mathematics*, 39(4):524–532, may 2018.
- [35] Andrey Gorobets and Pavel Bakhvalov. Heterogeneous CPU+GPU parallelization for high-accuracy scale-resolving simulations of compressible turbulent flows on hybrid supercomputers. *Computer Physics Communications*, 271:108231, feb 2022.
- [36] E K Guseva, A V Garbaruk, and M Kh Strelets. An automatic hybrid numerical scheme for global RANS-LES approaches. *Journal of Physics: Conference Series*, 929:012099, nov 2017.
- [37] J.E. Ffowcs Williams and D.L. Hawkings. Sound generation by turbulence and surfaces in arbitrary motion. *Philosophical Transactions of the Royal Society of London. Series A, Mathematical and Physical Sciences*, 264(1151):321–342, may 1969.

[38] F. Farassat. Linear acoustic formulas for calculation of rotating blade noise. *AIAA Journal*, 19(9):1122–1130, sep 1981.

- [39] Philippe R. Spalart and Michael L. Shur. Variants of the ffowcs williams hawkings equation and their coupling with simulations of hot jets. *International Journal of Aeroacoustics*, 8(5):477–491, jul 2009.
- [40] Yaser Khalighi, Frank Ham, Joseph Nichols, Sanjiva Lele, and Parviz Moin. Unstructured large eddy simulation for prediction of noise issued from turbulent jets in various configurations. In 17th AIAA/CEAS Aeroacoustics Conference (32nd AIAA Aeroacoustics Conference). American Institute of Aeronautics and Astronautics, jun 2011.

Conclusions and further work

4.1 Concluding remarks

As this thesis is clearly divided into two big blocks, we have decided to summarise the conclusion of each part separately.

4.1.1 Concluding remarks on the development of a new dispersion error methodology

How would dispersion error be computed on non-uniform Cartesian grids? How could we give a measure of this type of error without having to rely on using a method involving the Fourier Transform? These questions were the seed to develop an alternative methodology able to give a dispersion error measure that was not restricted either to uniform cartesian grids or linear discretization schemes, as the majority of meshes used within the CAA community are stretched and blendings between diffusive and non-diffusive schemes are usually selected to ensure stability without compromising the validity of the results.

The developed method has shown a perfect match when applied to structured, evenly spaced grids, recovering the classical results from Tam [1] or Lele [2]. Nonetheless, what is more interesting is that when the method is applied to uniform or non-uniform grids, and both the analytical and the

recovered eigenvalue are multiplied by the maximum grid size, two different plots are obtained. For the selected stretching factor, i.e., 1 to 5 %, the recovered numerical eigenvalue for all the studied grids overlaps in a single plot.

Thanks to the prior point, we have computed a "maximum" eigenvalue associated with each numerical scheme. Results show that high-order schemes have, as a rule of thumb, a maximum eigenvalue 50 % higher than a low-order scheme. Taking into account Trias and Lehmkuhl [3] considerations for computing the time step, this implies that high-order schemes should have, for the same mesh, a time step reduced by 2/3 in comparison to a low-order scheme, requiring more time steps to achieve the same simulation time.

Finally, the comparison between the effective cost, considering both the maximum time step as well as the arithmetic intensity and the number of access bytes each differential scheme requires, has shown interesting results. First, high-order schemes exhibit a rapid degradation, i.e., loss of the order of accuracy, compared to low-order schemes, which keep it. In the bibliography, it is often stated that high-order schemes lose one order of accuracy when applied to non-uniform meshes; the herepresent work has quantified this effect. Second, even for very tiny stretching factors, i.e., 2%, the numerical errors are becoming larger and coming closer to the maximum allowed error of about 1% suggested by Tam.

The extracted conclusions in this part of the work open the door to studying noise propagation phenomena in a generic computational aeroacoustics problem. The differences between low and high-order schemes when applied to the typical meshes used within the field, i.e., stretched grids, and using the kind of schemes canonical in CAA, i.e., non-linear upwinded schemes to ensure the stability of the simulation, do not show clear winner amongst the selected options.

4.1.2 Concluding remarks on jet aerodynamics and aeroacoustics

The second part of this thesis explores an application case, the simulation of a subsonic round jet, with the primary objective of quantifying the effect of the selection of the numerical scheme and the turbulence modeling applied have on both aerodynamics and aeroacoustics. This increases the initial scope of Pont-Vilchez [4] by not only comparing jet aerodynamics but also taking into account the effects into the acoustic spectra.

Regarding the effect that the order of accuracy of the numerical scheme has on jet aerodynamics, centerline velocities, and their fluctuations show a slightly better correspondence if high-order methods, i.e., NOISEtte, are used. In the range x/D < 10, OpenFOAM shows slightly higher oscillations than NOISEtte at the centerline, with smoothing as the mesh is refined. The same trend is observed at the lip line, with a faster convergence obtained by NOISEtte in comparison with OpenFOAM, which approximates the experimental results more slowly.

On the other hand, the scheme selection has a more pronounced effect on the far-field aeroacoustics. Both codes exhibit noisier results than the experimental ones at the coarsest mesh, reducing this mismatch when the mesh is consecutively refined. Nonetheless, NOISEtte 1/3rd integrated octave spectra show a better agreement between numerical and empirical results at higher Strouhal numbers, whereas OpenFOAM is not able to achieve the reference noise levels.

Regarding the effect that the selection of the turbulence model has on jet aerodynamics, the usage of the Smagorinsky turbulence model leads to a considerable mismatch between numerical and experimental results; only when using Δ_{SLA} results become accurate. Nonetheless, this is not surprising, as Δ_{SLA} is specifically tuned to work together with the Smagorinsky turbulence model, as this Δ_{SGS} takes the full role as a GAM, without being it leveraged between the turbulence model and the subgrid-scale. If other options are considered, such as $\sigma + \Delta_{\omega}$ or $S3QR + \Delta_{lsq}$, the GAM works as intended, obtaining very similar and accurate numerical results for these combinations.

Finally, acoustic spectra on the far field have shown excellent results for the selected GAM approaches: the differences between numerical and reference data for the finest grid do not exceed 3 dB, with the maximum difference located at a very high observer angle (150°). Among all the selected combinations, $S3QR + \Delta_{lsq}$ is the one exhibiting more differences between numerical and experimental results at high angles, whereas all the selected combinations show almost identical behavior for observer angles lesser than 120°.

4.2 Further work

As stated in the introduction, direct methods applied to CAA will be an unrealistic approach until DNS has become feasible on a weekly or, ideally, daily basis; therefore, hybrid approaches such as the ones used in the present thesis will be the used option until the computational power allows the first. Consequently, the current lines within hybrid approaches should be the ones to focus on: the generation of noise sources and noise propagation.

Regarding the computation of noise sources, the herepresent work has restricted its application to a decoupled acoustic wave problem. Decoupled in the sense that hydrodynamics generates the acoustics, but the acoustics do not interact with hydrodynamics; this basically means the CFD solver is acting as the noise generator feeding the acoustics solver. Nonetheless, when supersonic flows are considered, this assumption should be revisited. Screech tones generated due to the feedback loop between instability waves in the jet shear layer interacting with shock waves is an example of a non-decoupled system that appears within an aeroacoustics problem. Therefore, even though the method used in this work has been shown to be robust and able to produce reliable results, its validity should also be tested in more challenging cases with increased Mach numbers. This will allow us to determine the validity range of the present methodology.

The application case in this work benefits from the absence of walls generating noise, as the only walls are located upstream of the main noise-generating regions. However, in other cases, like the driven cavity problem or an aero-dynamic profile, where the walls play an important role in noise generation, the interaction between the RANS and LES models in DDES is of paramount importance. For example, the turbulent wake behind a car is known to be one of the main noise contributors at high-speed regimes. In the recent years, it has been shown that correct shielding behavior within DDES is mandatory, as otherwise, the LES mode could generate unphysical oscillations, leading to purely numerical noise. Improved DDES has been successfully used within the DES family in the context of wall-modelled Large-Eddy Simulations. Consequently, it should be interesting to analyze if this success can also be extrapolated to CAA simulations, as acoustics are extremely sensitive to the solution provided by the hydrodynamic simulation.

Regarding noise propagation methods, the present thesis only presents results using analytical transport methods, more precisely using the FWH equation. Nonetheless, the FWH equation can only deal with free propagation phenomena, which is not the usual situation. This could be solved by using a more general formulation of the Green function which considers the presence of additional boundary conditions, i.e., solid obstacles. However, from a mathematical point of view, this is extremely complex; this can be extrapolated to the vast majority of analytical transport methods, as the free-space Green function is used. Consequently, if analytical transport methods cannot deal with more complex situations involving noise reflections, numerical transport methods should be considered. At the beginning of this thesis, some preliminary work was done in incompressible-based, LPCE by Seo and Moon [5] and compressible-based transport methods, APE systems by Ewert and Scröder [6]. Including these methods within a CAA solver would allow studying flows where the acoustic-near field does not follow a free-space-like propagation.

Linked with the first item in this section, i.e., supersonic phenomena, but regarding noise propagation, non-linear wave propagation is another aspect that should be revisited. FWH equation, and basically all the equations derived from Lighthill's equation, is an inhomogeneous wave equation based on the d'Alembert operator: $\Box \phi$. Nonetheless, when the amplitudes of the acoustic waves become so large that they distort when traveling, other modelizations, like Westervelt or KZK, which introduce the concept of noise diffusivity, should be considered.

References

- [1] Christopher K W Tam and Jay C Webb. Dispersion-relation-preserving finite difference schemes for Computational acoustics. *Journal of Computational Physics*, pages 262–281, 1993.
- [2] Sanjiva K. Lele. Compact finite difference schemes with spectral-like resolution. *Journal of Computational Physics*, 1992.
- [3] FX Trias and O Lehmkuhl. A self-adaptive strategy for the time integration of navier-stokes equations. *Numerical Heat Transfer, Part B: Fundamentals*, 60(2):116–134, 2011.

[4] Arnau Pont-Vílchez, Alexey Duben, Andrey Gorobets, Alistair Revell, Assensi Oliva, and F. Xavier Trias. New strategies for mitigating the gray area in delayed-detached eddy simulation models. *AIAA Journal*, 59(9):3331–3345, sep 2021.

- [5] Jung H Seo and Young J Moon. Linearized perturbed compressible equations for low mach number aeroacoustics. *Journal of Computational Physics*, 218(2):702–719, 2006.
- [6] Roland Ewert and Wolfgang Schröder. Acoustic perturbation equations based on flow decomposition via source filtering. *Journal of Computational Physics*, 188(2):365–398, 2003.